AD-784 834

NASC-117 SATELLITE EXPERIMENT: MEASURE-MENT OF THE NONLINEAR IMPEDANCE AND NONLINEAR PLASMA EFFECTS IN THE NEAR FIELD OF AN ELECTRIC-DIPOLE ANTENNA

Harry C. Koons, et al

Aerospace Corporation

Prepared for:

Space and Missile Systems Organization

31 July 1974

AD784834

Final Report for the NASC-117 Satellite Experiment
Measurement of the Nonlinear Impedance and Nonlinear Plasma Effects in the Near Field of an Electric-Dipole Antenna

H. C. KOONS and F. A. MORSE
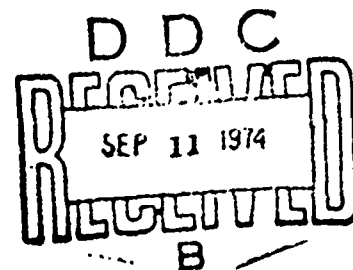Space Physics Laboratory
Laboratory Operations

and

D. A. McPHERSON
Development and Survivability Directorate
Technology Division, Development Operations
The Aerospace Corporation
El Segundo, Calif. 90245

31 July 1974

Final Report

Prepared for

SPACE AND MISSILE SYSTEMS ORGANIZATION
AIR FORCE SYSTEMS COMMAND
Los Angeles Air Force Station
Los Angeles, Calif. 90045

Approved

G. A. Paulikas, Director
Space Physics Laboratory
Laboratory Operations

Elliott Katz, Group Director
Development and Survivability
Directorate
Technology Division
Development Operations

Publication of this report does not constitute Air Force approval of the report's findings or conclusions. It is published only for the exchange and stimulation of ideas.

Jean Bogert, 2dLt, USAF
Technology Development
   Division
Project Officer

REPORT DOCUMENTATION PAGE		READ INSTRUCTIONS BEFORE COMPLETING FORM
1. REPORT NUMBER SAMSO-TR-74-162	2. GOVT ACCESSION NO.	3. RECIPIENT'S CATALOG NUMBER
4. TITLE (and Subtitle) FINAL REPORT FOR THE NASC-117 SATELLITE EXPERIMENT Measurement of the Nonlinear Plasma Effects in the Near Field of an Electric-Dipole Antenna		5. TYPE OF REPORT & PERIOD COVERED Final
		6. PERFORMING ORG. REPORT NUMBER TR-0075(9260-09)-1
7. AUTHOR(s) Harry C. Koons, Frederick A. Morse, and Donald A. McPherson		8. CONTRACT OR GRANT NUMBER(s) F04701-74-C-0075
9. PERFORMING ORGANIZATION NAME AND ADDRESS The Aerospace Corporation El Segundo, Calif. 90245		10. PROGRAM ELEMENT, PROJECT, TASK AREA & WORK UNIT NUMBERS
11. CONTROLLING OFFICE NAME AND ADDRESS Space and Missile Systems Organization Air Force Systems Command Los Angeles, Calif. 90045		12. REPORT DATE 31 July 1974
		13. NUMBER OF PAGES 116
14. MONITORING AGENCY NAME & ADDRESS(if different from Controlling Office)		15. SECURITY CLASS. (of this report) Unclassified
		15a. DECLASSIFICATION/DOWNGRADING SCHEDULE

16. DISTRIBUTION STATEMENT (of this Report)

Approved for release; distribution unlimited

17. DISTRIBUTION STATEMENT (of the abstract entered in Block 20, if different from Report)

18. SUPPLEMENTARY NOTES

19. KEY WORDS (Continue on reverse side if necessary and identify by block number)

Magnetospheric Plasma
Nonlinear Antenna Impedance
Electric Dipole Antenna
Very-Low-Frequency Waves

20. ABSTRACT (Continue on reverse side if necessary and identify by block number)

The nonlinear impedance of a satellite-borne, electric-dipole antenna was measured at ELF/VLF at drive voltages between 10 r V and 100 V peak-to-peak. The magnitude of the impedance is in general agreement with the predictions of theoretical models of plasma-clad antennas. At the higher drive voltages the magnitude of the impedance is a weak function of electron density. The magnitude decreases as electron density increases. At low voltages the phase angle of the impedance is in agreement with linear sheath models. As the voltage increases the phase angle rotates through 0 deg in the

20. ABSTRACT (Continued)

inductive sense. Above 10 V p-p the phase angle often exceeds +90 deg. The electric and magnetic field intensities measured in the near field of the primary dipole ⁓ ᴤ presented as a function of frequency, drive voltage, and electron density.

PREFACE

It is a pleasure to thank Dr. I. P. Shkarofsky for theoretical computations of the dipole impedance, and Mr. L. S. Bearce and Dr. .). J. Baker for discussions on the design of this experiment and the interpretation of the data.

CONTENTS

Preceding page blank

TABLES

FIGURES

FIGURES (Continued)

FIGURES (Continued)

FIGURES (Continued)

FIGURES (Continued)

FIGURES (Continued)

I. INTRODUCTION

A. SUMMARY

This report is a comprehensive report covering the period 27 June 1971 to 29 June 1973. It is the final report on work consisting of prelaunch and orbital support, and data reduction and analysis for the NASC-117 experiment, sponsored by the Naval Air Systems Command as part of the Navy Sub-LF Satellite Communications Technology Development Program. This experiment was carried by the satellite OV1-21S orbited by the U.S. Air Force, Space Experiments Support Program (SESP) Flight 70-2 on 7 August 1971. Technical guidance and experiment review was provided for the Navy by Mr. Loren S. Bearce of The Naval Research Laboratory, Washington, D. C.

The primary objective of the measurements was to determine the linear and nonlinear components of the amplitude and phase of the impedance of an electric-dipole antenna at voltages much higher than plasma potential and at seven frequencies in the ELF/VLF range from 40 Hz to 14.5 kHz.

The instrument operated successfully for the duration of the satellite lifetime of 27 days. A total of 41 hours of data was obtained.

The instrument is described in detail in Section II. In Sections III, IV, and V, prelaunch support, calibrations and orbital support are reported. The data reduction is discussed in Section VI, and the data analysis is described in Section VII. Finally, the significant results are compiled in Section VIII.

B. BACKGROUND

Measurements of the linear component of the antenna impedance of electric-dipole antennas at ELF/VLF have been performed on the Aerobee 4.58 and 4.59, the Black Brant 4.09, and the Javelin 8.45 rocket flights, and on the ISIS I, ISIS II, Injun 5, OV3-3, and LOFTI-IIA satellites (Refs. 1 through 9). These measurements have produced the following results: (1) The impedance of the sheath surrounding an electric-dipole antenna dominates the impedance at the terminals of the antenna; (2) no effect in the VLF range has been seen at the characteristic frequencies in the plasma dielectric constant, such as the

ion-cyclotron frequencies and the lower-hybrid-resonance frequency; and (3) at moderate drive voltage (~10 V p-p), harmonics of the excitation frequency are observed in the signal from an electric-field antenna perpendicular to the driven antenna (Ref. 9). The measurement results demonstrate that such an antenna system is nonlinear; however, it is not possible to determine where or how the nonlinearity occurs.

The fundamental differences between the data obtained with these flights and the measurements required to determine the nonlinear effects of the plasma on the antenna system are as follows:

1. The excited-antenna current and voltage waveforms are not telemetered. In order to determine the nonlinear portion of the impedance, both the antenna current and voltage waveforms must be telemetered with as large a bandwidth as possible. The signal induced on a receiving antenna, such as the ones used on ISIS I, ISIS II, and the Black Brant 4.09, is partially isolated from the excited antenna by the intervening plasma and sheath and may not have the same waveform as the excited antenna current. These previous experiments have returned only the rms voltage and current from the driven antenna and this determines only the linear component of the antenna impedance.

2. With the exception of possibly the Black Brant 4.09, the driving voltages are not high enough to exceed the induced $\vec{v} \times \vec{B}$ voltage. For ISIS II, the maximum driving voltage (0.5 V p-p) does not exceed the sheath potential. To assure that all nonlinear effects are exhibited, driving voltages much greater than $\vec{v} \times \vec{B}$ must be used.

3. The receiving antennas used for the Black Brant 4.09, ISIS I, and ISIS II are not fully isolated from the excited antenna, but share a common sheath at the base of the antennas. Since most of the antenna admittance is at the antenna base, it is possible that the voltage induced on the receiving antenna is in part caused by the modulation of the sheath potential rather than by a penetration of the electric field into the plasma. This is essentially the mechanism by which the interference signals from the solar cell array were induced on the electric-field antenna on OV3-3 (Ref. 6).

4. Simultaneous magnetic measurements were not performed on the Black Brant and ISIS experiments. It is highly desirable to measure both the electric and magnetic intensities of the fields which penetrate the plasma. If the excited antenna is generating ion waves in the plasma, these can be identified by the completely electrostatic character of the fields.

-2-

An efficient radiating system cannot be designed without a detailed knowledge of the antenna impedance characteristics (Refs. 16, 17).

The measurements discussed above have determined only the linear component of the impedance. Complex nonlinear characteristics of the impedance at voltages above the plasma potential are predicted by nonlinear Langmuir probe treatments (Refs. 10, 14, 17, 18). A measurement of the nonlinear component of the impedance is required to determine the applicability of the concept of impedance matching to the proposed communication system and to verify these theoretical analyses.

It is also necessary to determine the extent to which characteristic frequencies in the plasma dielectric constant, such as the ion cyclotron frequencies and the lower-hybrid-resonant frequency, affect the nonlinear component of the impedance. To date, no effect has been seen at these frequencies in the linear component. The evidence that such an antenna system is nonlinear has been demonstrated at ELF/VLF by recent rocket measurements, and at higher frequencies by the Alouette sounder measurements.

The Javelin 8.45 linear impedance measurements show an unexplained phase shift of approximately 45° when the antenna axis is aligned with the geomagnetic field (Ref. 4). A measurement of changes in the near-field of the antenna as well as of the nonlinear impedance may clarify this phenomenon.

Besides power losses within the sheath, it is necessary to determine under what conditions and to what extent power is lost to electrostatic plasma turbulence.

Calculations presented by Scarf (Ref. 11) predict the runaway electric field to be orders of magnitude smaller than the electric fields expected in the vicinity of the antenna. A measurement of the electric fields in the vicinity of the antenna for all plasma conditions of interest to the proposed system is required to determine the extent of transmission losses associated with electrostatic plasma turbulence.

The effective current source for the radiation field consists of the current flowing in the sheath and plasma as well as that on the antenna. A measurement of the ac magnetic field at the ferrite-core-coil magnetic antenna during excitation of the primary dipole may be used to determine the extent to which the sheath and plasma currents cancel the antenna current.

The results obtained from this experiment are required for the design of a practical ELF/VLF satellite transmitter.

C. SCHEDULE

The proposed project schedule together with the actual performance are shown in Fig. 1. Most tasks were completed on or ahead of the scheduled completion date. Items dependent on computer data reduction, such as digitization of baseband data, ephemeris calculations, PCM-ephemeris merge, and aspect program modification were initially delayed by a computer hardware change from the CDC 6600 to the CDC 7600 at The Aerospace Corporation. The increased speed and capacity of the CDC 7600 allowed these items to be completed by July 1972.
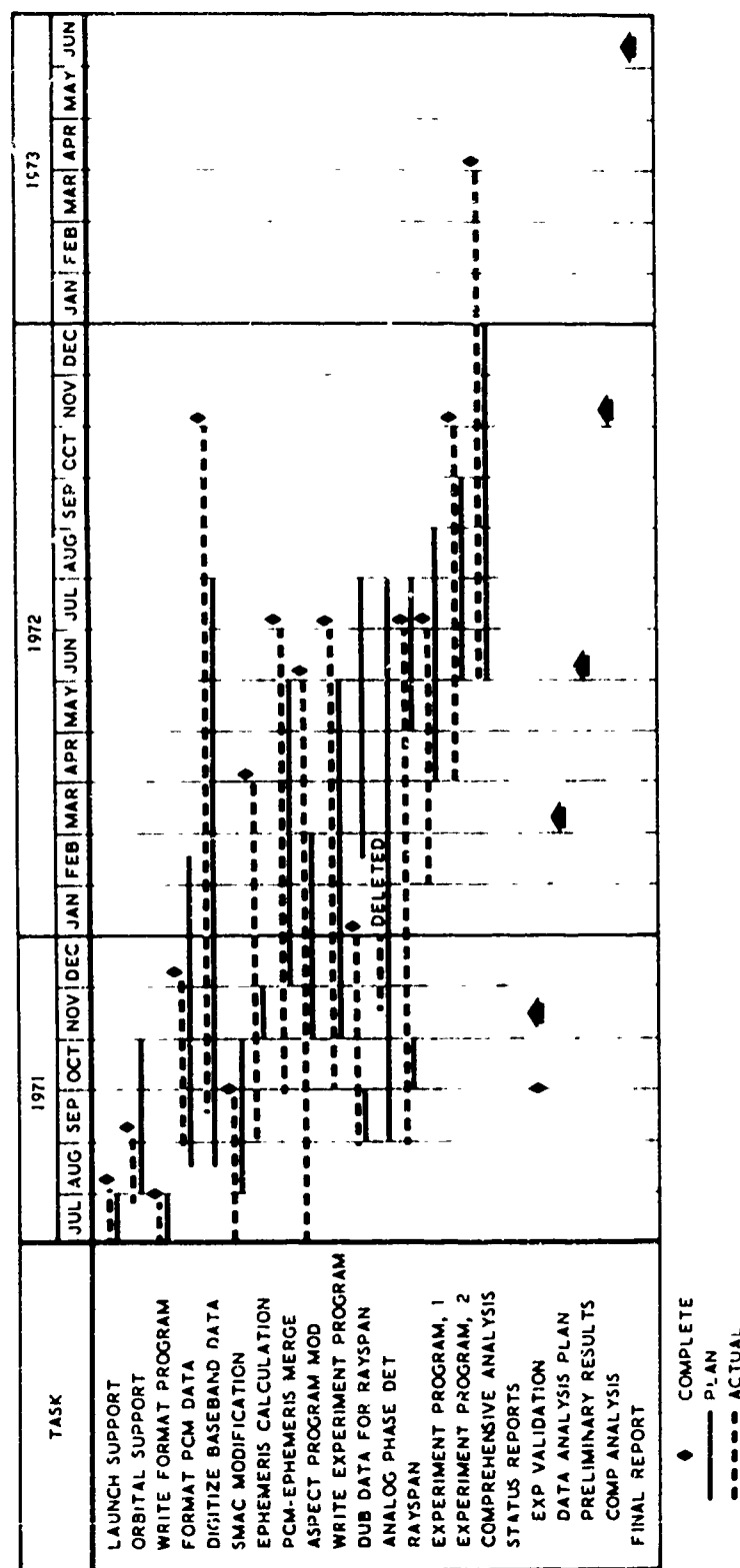
Fig. 1. NASC-117 experiment schedule. (The solid lines show the planned schedule. The dashed lines show the actual performance. The diamonds indicate the actual completion data for each item.)

II. DESCRIPTION OF EXPERIMENT

The OV1-21S (1971-67A) spacecraft was launched from the Western Test Range on 7 August 1971, into a polar orbit with a 102-min period, an 87.6° inclination, a 921-km apogee, and a 800-km perigee. The spacecraft was spin-stablized with a spin rate of 1.5 rpm after the antenna assemblies were deployed.

Figure 2 is a diagram of the spacecraft configuration. The electric-dipole antenna consisted of two STEM elements, each 16-m long and 1.27-cm in diameter, deployed perpendicular to the spin axis. The magnetic-field and electric-field intensities were measured by a ferrite-core-coil magnetic probe and two dual-sphere electric probes, respectively. These probes were deployed on a 2-m long boom approximately 2 m behind the electric-dipole antenna.

In addition to the VLF instrumentation, the satellite contained a boom-mounted spherical ion retarding potential analyzer and a body-mounted planar ion retarding potential analyzer (Fig. 2).

The electric-dipole antenna was sinusoidally excited at seven voltage levels between 10 mV and 100 V peak-to-peak at 400 and 730 Hz and 1.3, 2.3, 3.9, 7.35, and 14.5 kHz following the sequence shown in Fig. 3. Each voltage was applied for two seconds. Following the 100-V step at each fre-quency the experiment was quiescent for two seconds to enable the receivers to monitor ambient VLF signals. An 18-sec quiescent period followed the 100-V excitation at 730 Hz.

Six broadband channels on two S-band transmitters were used to transmit the impedance and ELF/VLF receiver data to the U.S. Air Force, Satellite Control Facility, Range Tracking Stations using the channel format shown in Fig. 4. The voltage waveform exciting the primary dipole antenna directly modulated one of the transmitters with a bandwidth of 30 kHz. The resulting current waveform at the feed points of the dipole antenna directly modulated the other transmitter with a bandwidth of 30 kHz. The VLF signals

-7-
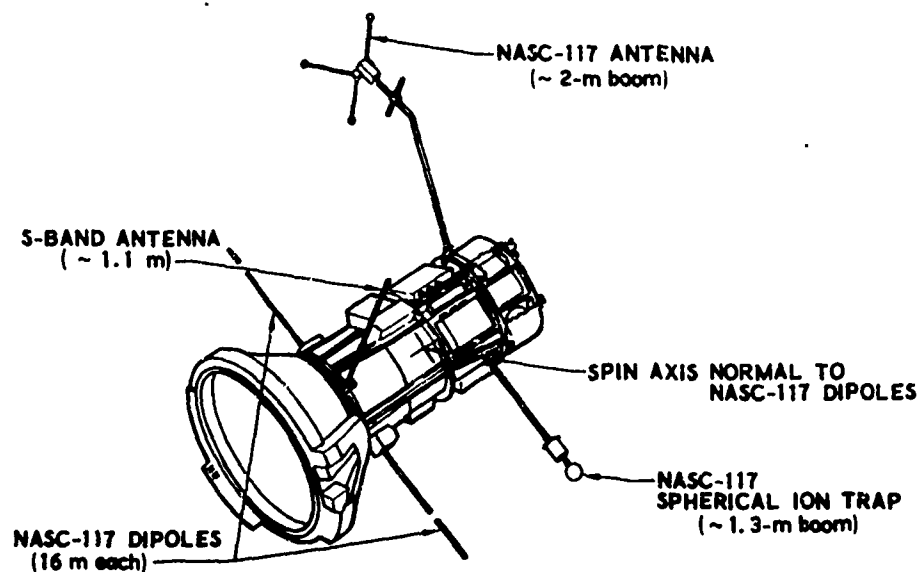
Fig. 2. OV1-21 configuration.
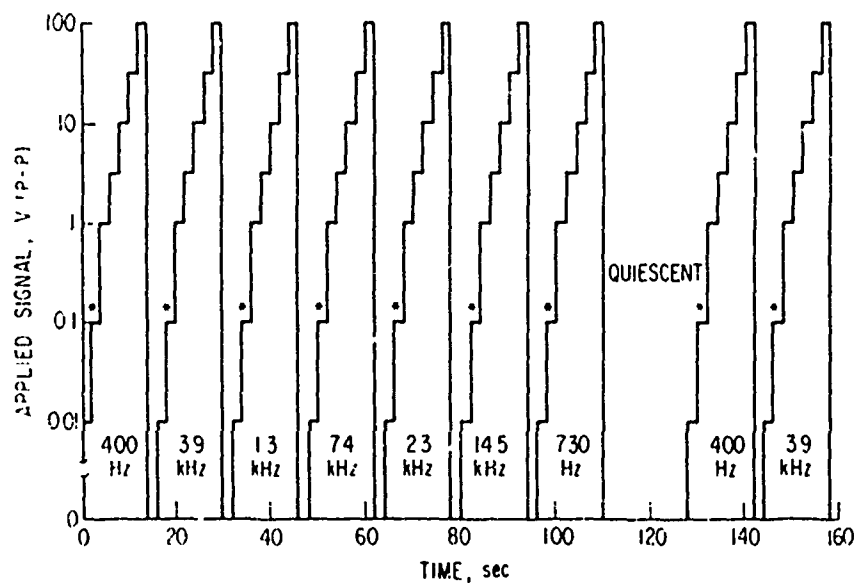
Fig. 3. Excitation sequence of the primary dipole antenna. (The
program repeats with a period of 128 sec. The impedance
of the dual-sphere antenna is measured during the time
periods designated by the asterisks.)
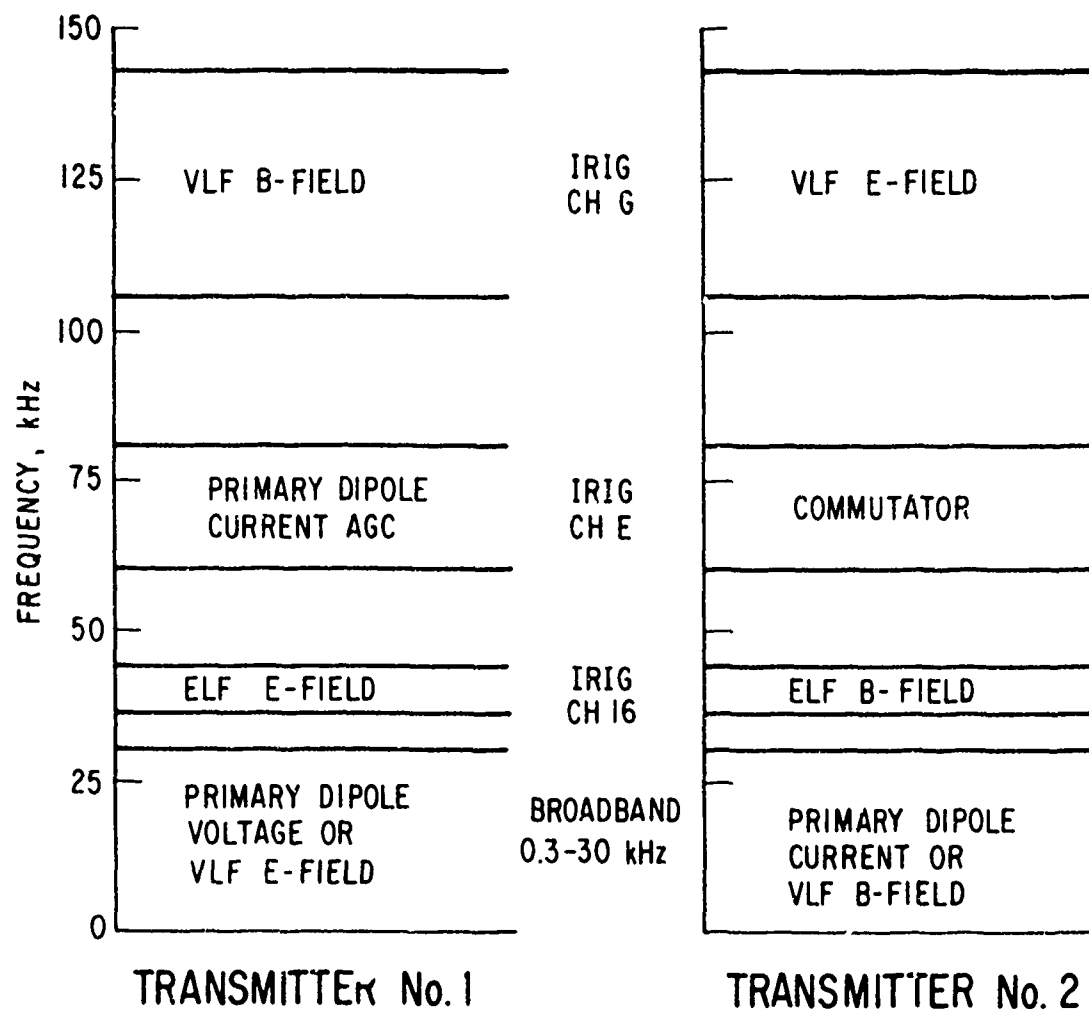
Fig. 4. Channel assignments for the two S-band telemetry transmitters.

detected by the magnetic- and electric-field probes were transmitted on
IRIG channel G's with a bandwidth of 5 kHz and 18 kHz, respectively. The
ELF signals from the probe antennas were transmitted on IRIG channel 16
with a bandwidth of 600 Hz. In addition, data from narrow-band ELF/VLF
receivers and from the ion retarding-potential analyzers were telemetered
on a 512 word-per-second PCM commutator.

III.   PRELAUNCH SUPPORT

Prelaunch support at Vandenberg Air Force Base was provided almost continuously from 9 July to 1 August 1971. A complete set of calibration data was obtained at that time.   These data were reduced and compared with calibration data obtained in the laboratory and at General Dynamics Convair.   The combined calibration sets were used for post-flight data reduction.

IV. CALIBRATIONS

A. PRIMARY DIPOLE IMPEDANCE

A schematic diagram of the circuit used to measure the primary dipole voltage and current is shown in Fig. 5. The current is measured by measuring the voltage drop across the 1.0 kΩ resistor in series with the antenna. Prelaunch calibrations were obtained by placing impedances of known magnitude across the primary dipole. Following the notation shown in Fig. 5, the voltage V_{out} at the output of the automatic gain control (AGC) amplifier is related to the voltage V_{in} at the input of the AGC amplifier by

$$V_{in} = \alpha \, V_{out} \tag{1}$$

where α, the attenuation of the AGC amplifier is derived from preflight measurements of V_{in} and V_{out}.

The voltage across the 1.0 kΩ current measuring resistor is then related to V_{in} by

$$V_{1k} = V_{in}/G \tag{2}$$

where G is the gain of the level matching network between the 1.0 kΩ resistor and the AGC amplifier. This passive network sets the level of the voltage at the input to the AGC amplifier at approximately the same value over the entire range of drive voltages from 0.01 to 100 V. The current through the 1.0 kΩ resistor is then

$$I_{1k} = \frac{V_{in}}{G \times 1000} = \frac{V_{ant}}{1000 + Z_L} \tag{3}$$

Preceding page blank
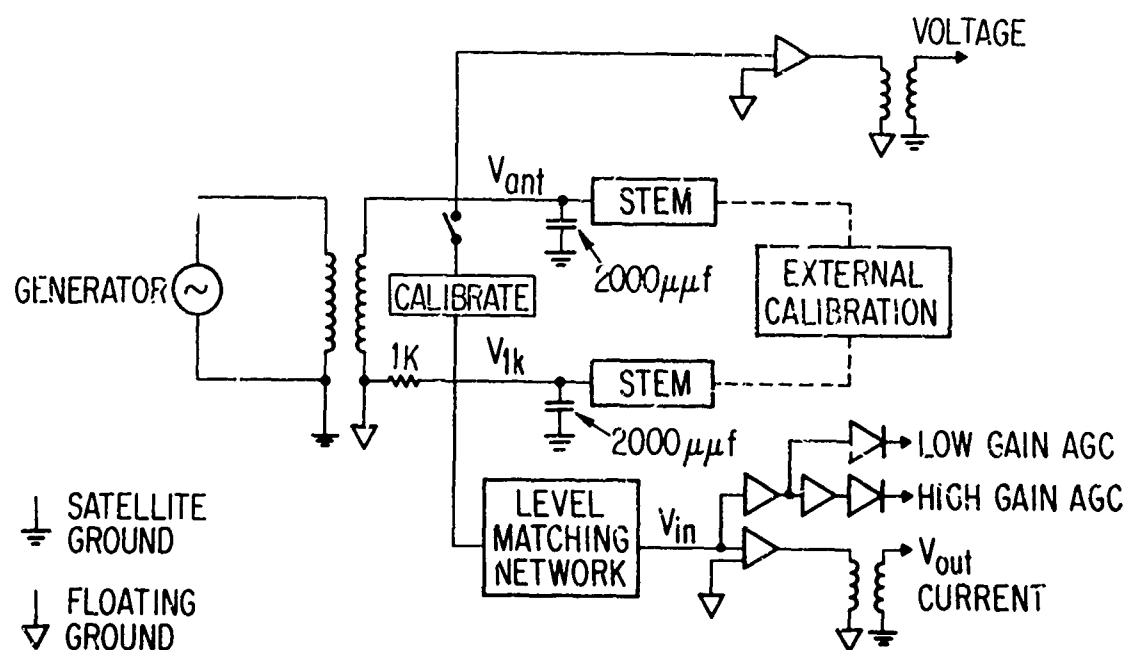
Fig. 5. Circuit that measures the impedance of the primary
dipole antenna. (The internal calibration mode is
selected by ground command. The external calibra-
tions were performed prior to launch.)

and the load (or external calibration) impedance i

$$Z_L = \frac{V_{ant}}{I_{lk}} \approx \frac{1000\, V_{ant}\, G}{V_{in}} - 1000 \qquad (4)$$

For the prelaunch calibrations $Z_L = R_j$ and from Eq. (3)

$$V_{in} \times (1.0k + R_j) = V_{ant}\, G \times 1k \qquad (5)$$

or dividing by 1.0 kΩ

$$V_{in} \times (1 + R/1000) = V_{ant}\, G \qquad (6)$$

From the telemetered flight data the magnitude of the load impedance at low voltage drive is determined from Eq. (4) where $V_{ant}\, G$ is known from preflight calibrations and V_{in} is obtained from the high or low gain AGC measurements in the commutated data. At high voltage drive only the fundamental component of the current waveform is used for I_{lk} in Eq. (4).

Two sets of prelaunch calibration data were obtained and used for the determination of the matrix $V_{ant}\, G$. The first set was obtained on 21 June 1971 at General Dynamics Convair. The second was obtained on 11 July 1971 at Vandenberg Air Force Base. On both dates resistors of known value were placed externally across the primary dipole antenna. With the instrument operating in its normal, high voltage, data taking mode, the data for a complete block of frequencies were obtained for each resistor. The values of the resistors used were 0.5, 1, 2, 4, 8, 10, 20, 40, 80, 100, 200, 400, and 800 kΩ. The 1.0 and 2.0 kΩ data were used as the primary calibration data because they yielded the highest currents and the highest signal-to-noise ratios in the broadband data. The data from the two prelaunch calibrations were statistically combined. The resulting $V_{ant}\, G$ matrix is shown in Table I.

B.   FERRITE-CORE-COIL MAGNETIC ANTENNA

The effective area of the magnetic antenna was measured to be
180 m^2 at 400 Hz. The measured resistance of the 3600 turn coil was 690 Ω.
At 1.0 kHz the measured Q was 13. The 0 dB level was set at approximately
150 mγ for each of the narrowband channels. The range of the intensity mea-
surements was -60 dB to 0 dB.

C.   DUAL-SPHERE ELECTRIC ANTENNAS

The 0 dB level was set at 100 mv for each of the narrowband chan-
nels. The range of the intensity measurements was approximately -60 dB
to 0 dB.

Table I. Matrix of $V_{ant}G$ Values Determined from Preflight
Calibrations

Excitation Voltage (V)	$V_{ant}G$, mV						
	0.01	0.1	1	3	10	30	100
Excitation Frequency (Hz)							
400	299	672	798	1181	967	842	880
3900	309	693	823	1218	998	869	908
1300	305	684	813	1202	985	858	896
7350	294	659	783	1159	949	826	863
2300	326	731	868	1285	1053	916	957
14350	526	1182	1404	2077	1701	1481	1548
730	340	764	907	1342	1100	957	1000

V. ON-ORBIT OPERATION

The SESP Flight 70-2 was launched on 7 August 1971. On-orbit support was provided at the U.S. Air Force, Satellite Test Center (STC) in Sunnyvale, California, continuously from launch until battery depletion occurred on 6 September 1971.

Figure 6 lists the satellite characteristics. Acquisition of telemetry was commonly made at elevation angles of 5° or lower rather than the design value of 15°. This resulted in increased telemetry acquisition time for each station pass.

The despin spin period was changed from 60 to 45 sec prior to launch in order to improve stability.

The antennas were deployed for a predetermined time period based on deployment rates measured by the vendor. The 53-ft extension at the end of the deployment period was considered to be close enough to the planned value of 55 ft so that further adjustments were not necessary.

Two anomalies occurred during orbital operation. Evaluation of NASC-117 data showed that a warmup time was required for the automatic gain control amplifiers that conditioned data for the 30-kHz broadband telemetry channels. The impact of the warmup time was minimized by operating the satellite at a high duty cycle for three or four hours and then leaving it off for the remainder of the day. After two weeks of operation in this mode, the aspect of the satellite to the sun had changed enough so that the warmup period was not required.

The second anomaly was a continuous current leak that developed in the satellite battery system. This leak reduced the active life of the satellite from 60 days to 27 days. Because the satellite operation was monitored continuously, the malfunction in the battery was immediately detected, and the satellite telemetry scheduling was increased to obtain as much data as possible before battery depletion. As a result, a total of 41 hours of operation was obtained instead of the design operation time of 54 hours.

-17-

	PLANNED	ACTUAL
LAUNCH DATE:	JULY 31	AUGUST 6
ORBIT:	450 NM	429 x 498 NM
INCLINATION:	87.6°	87.6°
ACQUISITION:	15°	5°
SPIN RATE:	1 rpm	1.5 rpm
ANTENNA DEPLOYMENT	55 ft	53 ft
SATELLITE LIFETIME	60 days	27 days
HOURS OF OPERATIONS	54 hr	41 hr

Fig. 6. Planned and actual satellite characteristics.

The major effect of the shortened lifetime was to curtail the planned program of OV1-21S coordination with other VLF satellite and ground station receivers. The first several weeks of operation were spent in establishing operations among the various agencies and personnel operating the other receivers. As a result, little simultaneous data recording occurred before the end of life of OV1-21S.

The orbital support is summarized in Fig. 7.

- **27-DAY SATELLITE LIFETIME**

    - **REDUCED FROM 60 to 90 DAYS BY ANOMALOUS DEPLETION OF BATTERY POWER**

- **10 ACQUISITIONS PER DAY**

    - **INCREASED FROM 6 PLANNED**

- **OPERATIONS MONITORED CONTINUALLY FOR 27-DAY LIFETIME**

Fig. 7. Orbital support provided at the Satellite Test Center, Sunnyvale, California.

VI. DATA REDUCTION

A. INTRODUCTION

Figure 8 is a flow diagram of the data reduction procedure. The objective of this procedure is to prepare the telemetered data for analysis.

Each telemetry tape from a **Range Tracking Station (RTS) is** processed in three passes. In the first pass, the PCM data from the commutator (channel E, transmitter 2) is digitized and formated for use in the computer. In the second pass, the analog voltage and current waveforms (transmitter 1 baseband and transmitter 2 baseband, respectively) are digitized for Fourier analysis. For this digitization, the telemetry tapes were run at 30 ips, which is a 4:1 reduction from the speed at which they were recorded at the RTS. Each waveform was sampled at 25,000 samples per second using the Simultaneous Sample and Hold (SS and H) digitization program. One hundred millisecond intervals separated by two seconds were digitized. In the third pass, the analog data were dubbed onto tapes which were sent to Stanford University for RAYSPAN spectral analysis.

Ephemeris data from ADC spacetrack are used to generate tapes with orbital elements at hourly intervals. These tapes are then processed by the BLAMEX computer program to generate ephemeris parameters and magnetic coordinates at one second intervals. These data were then merged with the formated PCM data by the Satellite Merge and Calibrate Program (SMAC). The resulting SMAC tape is then used as input for the aspect and reduction programs.

B. OV1-21 VLF PROGRAM

The VLF program prints the required experiment status, orbit parameters and satellite aspect as well as calibrated data from the experiment sensors. The print out is organized into blocks which contain 128 sec of data. Each block originates at time zero relative to the program

Preceding page blank
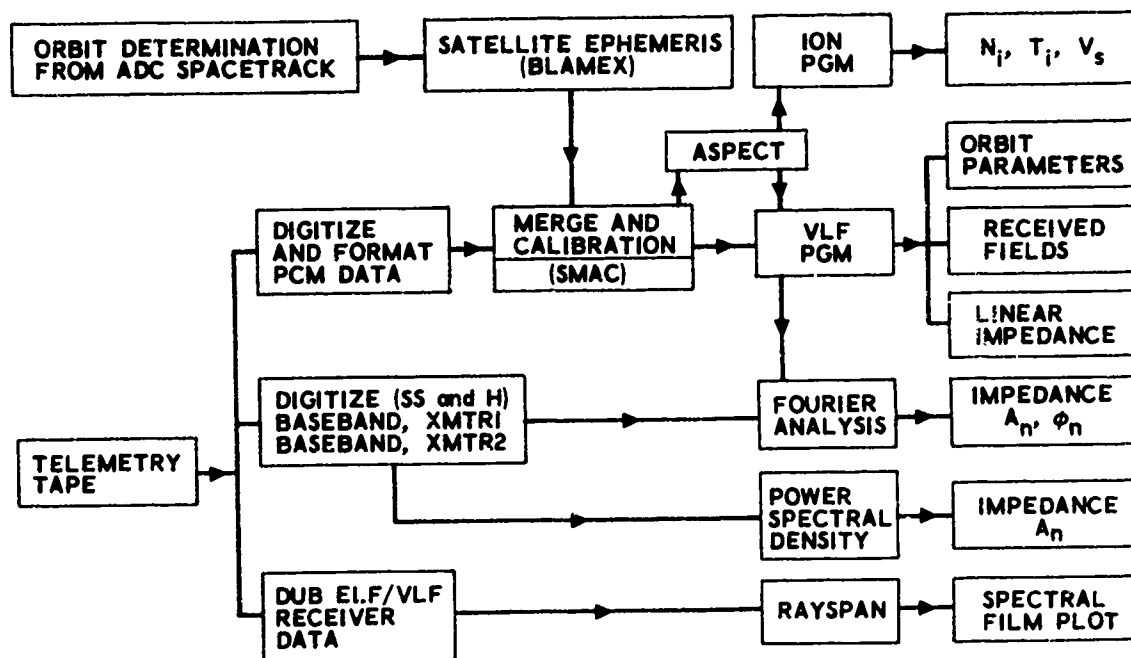
Fig. 8. Data reduction flow diagram.

sequence shown in Fig. 3. Examples of the data printed by this program for one data block are shown in Figs. 9 to 18. These data were acquired by the tracking station on Hawaii during orbit 58.

The first page, shown in Fig. 9, contains the experiment status in the upper left hand corner, SIG for the data mode and CAL for the calibrate mode; B-FIELD if the VLF receiver data are being taken by the magnetic antenna and one electric antenna or E2-FIELD if data are being taken by both electric antennas; and HIGH if the excitation voltage steps extend to 100 V p-p or LOW if the voltage steps terminate at 1 V p-p. For the block shown in Fig. 9 through 13, the status is data mode, with magnetic antenna data, and the voltage steps extend to 100 V p-p as indicated by the words SIG B-FIELD HIGH.

The orbit parameters are printed out every 16 sec at the 0.01 V excitation at each frequency. On the page, shown in Fig. 9, the rms electric potential in millivolts and the rms magnetic-field intensity in milligamma detected by the VLF receiver at the excitation frequency are also displayed. These data are the average values of four samples obtained over the two seconds at each excitation level. The impedance of the electric antenna is measured when the primary dipole excitation is 100 mV; hence, no electric field data is obtained for that step. The data in the column labeled PASS are ambient levels measured when the primary dipole is not excited.

On the next page, shown in Fig. 10, the impedance of the dual sphere electric antenna parallel to the primary dipole, measured four times during the 100-mV p-p excitation step, are displayed together with the rms broadband (the bandwidth is 600 Hz) ELF electric potentials and magnetic-field intensities from the receiver.

During the 18 sec when the primary dipole is not excited following the 730 Hz excitation, the DC potential between one of the monopoles and the spacecraft is measured. These data are contained on the third page shown in Fig. 11, together with orbit parameters, the calculated value of the DC potential, $\vec{V} \times \vec{B} \cdot \vec{l}$, induced by satellite motion through the plasma, and the levels measured by the narrowband channels of the VLF receivers.

-23-

SIG B-FIELD HIGH FREQ KHZ	UTIME SEC	UTIME HR MIN SEC			B GAUSS	L ER	INVL DEG	ALT KM	LT HR	MLT HR	SAT VEL KM/SEC	LAT DEG	ELONG DEG	MLAT DEG	MELONG DEG	SUN
.40	81939.2	22	45	39	.40267	4.71	62.55	841.	15.3	15.2	7.45	51.9	249.1	59.0	305.0	
3.90	81955.2	22	45	55	.40107	4.47	61.78	839.	15.3	15.2	7.45	50.8	249.1	58.1	305.3	
1.30	81971.2	22	46	11	.39931	4.24	60.93	838.	15.3	15.2	7.45	49.9	249.2	57.2	305.6	
7.35	81987.2	22	46	27	.39743	4.00	60.01	837.	15.3	15.2	7.45	48.9	249.2	56.2	305.9	
2.30	82003.2	22	46	43	.39540	3.77	58.99	836.	15.3	15.2	7.45	48.0	249.2	55.3	306.2	
14.35	82019.2	22	46	59	.39324	3.53	57.85	835.	15.3	15.3	7.45	47.0	249.2	54.3	306.4	
.73	82035.2	22	47	15	.39096	3.30	56.59	834.	15.3	15.3	7.45	46.1	249.2	53.4	306.6	
8.00	82051.2	22	47	31	.38853	3.19	55.92	832.	15.3	15.3	7.45	45.1	249.1	52.5	306.9	

ELECTRIC FIELD
(MILLIVOLTS)

FREQ	10MV	100MV	1V	3V	10V	30V	100V	PASS
.40	.555	0.000	.328	1.871	8.483	30.691	122.975	.231
.73	.325	0.000	.468	4.797	16.383	45.585	97.585	.286
1.30	.179	0.000	2.753	11.559	16.710	25.035	67.419	.178
2.30	.196	0.000	2.410	9.385	10.309	14.651	43.343	.189
3.90	.178	0.000	.273	4.013	8.460	15.665	36.895	.178
7.35	.404	0.000	.475	2.804	7.967	13.345	37.908	.465
14.35	.319	0.000	.604	2.524	6.881	17.024	116.699	.258

MAGNETIC FIELD
(MILLIGAMMA)

FREQ	10MV	100MV	1V	3V	10V	30V	100V	PASS
.40	20.304	21.503	21.651	23.697	39.147	100.977	356.276	23.035
.73	29.639	42.426	27.066	68.523	195.685	414.163	414.163	23.059
1.30	.129	4.708	8.452	74.433	207.223	215.484	193.098	.183
2.30	3.582	6.777	48.088	209.206	209.206	209.206	209.205	3.088
3.90	4.021	3.955	10.024	181.748	185.042	185.042	166.024	1.429
7.35	8.626	8.354	21.293	185.619	201.993	201.993	201.993	.571
14.35	9.288	55.018	214.017	214.017	214.017	214.017	214.017	4.270

Fig. 9. Typical printout by VLF program. (This page contains
the orbital parameters for one block of data as well as
the rms potentials and rms magnetic-field intensities
from the narrowband receivers.)

E1-IMPEDANCE
(OHMS)

FREQ	1	2	3	4	AVE
.40	0.	8.41E+05	1.00E+07	1.00E+07	6.95E+05
.73	6.74E+05	9.36E+05	6.96E+05	6.31E+05	7.34E+05
1.30	1.32E+05	1.45E+05	1.51E+05	1.58E+05	1.47E+05
2.30	1.91E+05	1.91E+05	1.91E+05	1.91E+05	1.91E+05
3.90	9.12E+04	9.12E+04	9.12E+04	9.12E+04	9.12E+04
7.35	5.01E+04	5.01E+04	5.25E+04	5.25E+04	5.13E+04
14.35	2.02E+04	2.02E+04	2.02E+04	2.24E+04	2.08E+04

E-ELF
(MILLIVOLTS)

FREQ	10MV	100MV	1V	3V	10V	30V	100V	PASS
.40	8.18	71.97	6.60	32.73	71.97	71.97	71.97	10.28
.73	7.61	9.81	5.62	7.15	16.58	71.97	71.97	8.75
1.30	7.57	5.62	6.70	6.17	6.48	8.46	10.53	9.95
2.30	6.88	5.62	5.75	5.62	5.88	7.56	8.94	8.40
3.90	7.83	5.62	6.38	6.16	6.06	7.19	5.62	8.22
7.35	7.43	5.62	7.85	7.64	5.84	11.03	7.02	9.59
14.35	5.84	5.62	5.83	7.41	8.51	71.97	71.97	7.81

B-ELF
(MILLIGAMMA)

FREQ	10MV	100MV	1V	3V	10V	30V	100V	PASS
.40	5.76	8.22	8.87	31.21	34.77	34.77	34.77	4.59
.73	4.75	4.28	4.45	9.54	34.77	34.77	34.77	4.18
1.30	4.93	4.12	3.96	5.05	11.04	34.39	14.15	7.10
2.30	5.46	4.22	4.70	17.68	29.62	34.77	34.77	4.64
3.90	4.81	4.50	4.01	5.26	10.86	6.91	4.57	11.93
7.35	6.71	5.59	8.19	34.77	34.77	34.77	34.77	6.46
14.35	6.80	25.92	34.77	34.77	34.77	34.77	16.21	5.03

Fig. 10. Typical printout by VLF program. (This page contains the impedance of the dual-sphere antenna measured four times during the 100-mV excitation step at each frequency. The rms broadband ELF potentials and magnetic-field intensities are tabulated for one data block.)

UTIME SEC	G GAUSS	MLAT DEG	DC VOLT	VXB.L VOLT	.40	.73	1.3	2.3	3.9	7.35	14.35	.40	.73	1.3	2.3	3.9	7.35	14.35
	DC VOLTAGE				ELECTRIC NARROWBAND (PASSIVE)							MAGNETIC NARROWBAND (PASSIVE)						
82051.2	.3885	52.5	-.180	-.281	.21	.25	.18	.19	.18	.30	.24	22.70	24.26	.13	2.05	1.46	.87	4.27
82051.7	.3884	52.4	-.180	-.303	.21	.29	.18	.19	.18	.30	.24	23.33	24.26	.13	2.06	1.46	.83	4.27
82052.2	.3884	52.4	-.206	-.316	.21	.29	.18	.19	.18	.30	.24	24.63	24.26	.13	2.11	1.68	.94	4.27
82052.7	.3983	52.4	-.231	-.327	.21	.29	.18	.19	.18	.30	.24	25.31	25.16	.13	2.17	1.52	.92	4.27
82053.2	.3882	52.3	-.257	-.336	.21	.34	.18	.19	.18	.37	.24	20.93	26.08	.13	2.78	1.66	.96	4.27
82053.7	.3881	52.3	-.257	-.344	.21	.29	.18	.19	.18	.37	.24	20.93	26.08	.13	2.73	1.66	.94	4.27
82054.2	.3881	52.3	-.257	-.349	.21	.29	.18	.19	.18	.37	.24	20.33	26.08	.13	2.73	1.60	.96	4.27
82054.7	.3880	52.3	-.282	-.353	.21	.29	.18	.19	.18	.37	.24	20.93	26.08	.13	2.68	1.63	1.08	4.27
82055.2	.3879	52.2	-.282	-.354	.21	.29	.18	.19	.18	.37	.24	20.93	24.26	.13	2.41	1.60	.94	4.27
82055.7	.3878	52.2	-.282	-.354	.21	.29	.18	.19	.18	.37	.24	20.93	24.26	.13	2.45	1.60	.92	4.27
82056.2	.3877	52.2	-.282	-.351	.21	.29	.18	.19	.18	.37	.24	20.93	24.26	.13	2.45	1.60	.89	4.27
82056.7	.3877	52.1	-.282	-.346	.21	.29	.18	.19	.18	.37	.24	20.93	24.26	.13	2.45	1.63	.77	4.27
82057.2	.3875	52.1	-.282	-.340	.21	.29	.18	.19	.18	.37	.24	20.93	24.26	.13	2.45	1.66	1.01	4.27
82057.7	.3875	52.1	-.282	-.331	.21	.29	.18	.19	.18	.37	.24	20.93	24.26	.13	2.45	1.60	.80	4.27
82058.2	.3874	52.0	-.257	-.321	.21	.29	.18	.19	.18	.37	.24	20.93	24.26	.13	2.50	1.54	1.21	4.27
82058.7	.3873	52.0	-.257	-.308	.21	.29	.18	.19	.18	.37	.24	20.93	24.26	.13	2.50	1.52	.99	4.27
82059.2	.3873	52.0	-.231	-.294	.21	.29	.18	.19	.18	.37	.24	20.93	24.26	.13	2.50	1.41	.94	4.27
82059.7	.3872	52.0	-.231	-.278	.21	.29	.18	.19	.18	.37	.24	20.93	24.26	.13	2.50	1.39	.84	4.27
82060.2	.3871	51.9	-.206	-.261	.21	.29	.18	.19	.18	.37	.24	20.93	25.16	.13	2.50	1.39	.81	4.27
82060.7	.3870	51.9	-.180	-.242	.21	.29	.18	.19	.18	.37	.24	20.93	25.16	.13	2.45	1.46	.86	4.27
82061.2	.3869	51.9	-.154	-.222	.21	.29	.18	.19	.18	.37	.24	20.93	25.16	.13	2.33	1.60	.90	4.27
82061.7	.3869	51.9	-.129	-.200	.21	.29	.18	.19	.18	.30	.24	21.50	25.16	.13	2.36	1.60	.96	4.27
82062.2	.3868	51.8	-.103	-.178	.21	.29	.18	.19	.18	.37	.24	20.93	24.26	.13	2.41	1.63	1.19	4.27
82062.7	.3867	51.8	-.078	-.154	.21	.29	.18	.19	.18	.30	.24	20.36	24.26	.13	2.31	1.57	1.21	4.27
82063.2	.3866	51.8	-.052	-.130	.21	.29	.18	.19	.18	.30	.24	20.36	24.26	.13	2.17	1.54	1.10	4.27
82063.7	.3865	51.7	-.027	-.104	.21	.29	.18	.19	.18	.30	.24	19.67	24.26	.13	2.08	1.49	.87	4.27
82064.2	.3865	51.7	-.001	-.079	.21	.29	.18	.19	.18	.30	.24	20.36	24.26	.13	2.11	1.46	1.05	4.27
82064.7	.3864	51.7	.024	-.052	.21	.29	.18	.19	.18	.37	.24	20.36	24.26	.13	2.15	1.31	.89	4.27
82065.2	.3863	51.6	.048	-.026	.21	.29	.18	.19	.18	.30	.24	19.67	18.35	.13	2.06	1.29	1.28	4.27
82065.7	.3862	51.6	.073	.001	.21	.29	.18	.19	.18	.30	.24	20.36	24.26	.13	2.13	1.22	1.47	4.27
82066.2	.3861	51.6	.097	.027	.21	.29	.18	.19	.18	.37	.24	19.67	23.40	.13	2.11	1.22	.83	4.27
82066.7	.3861	51.5	.122	.054	.21	.25	.18	.19	.18	.30	.24	19.67	23.40	.13	2.13	1.20	.81	4.27

Fig. 11. Typical printout by VLF program. (This page contains the data obtained during the 19-sec quiescent period.) It includes the measured DC potential between one STEM antenna and the body of the satellite, the $\nabla \times \overline{B} \cdot \overline{l}$ potential calculated from the model field, and data from the narrowband receivers.)

In Fig. 12, the magnitude in kilohms of the primary dipole impedance, assuming that only the fundamental frequency is present in the current wave-form, is printed as APPROXIMATE IMPEDANCE MAGNITUDE. The true magnitude is computed by the Fourier Analysis Program described below.

The aspect angle of the antennas with respect to the geomagnetic field and the satellite velocity vector are also printed in degrees in Fig. 12. In the coordinate system used, the axis of the primary dipole antenna is parallel to the y axis, the thrust axis of the OV1-20 propulsion module is parallel to the x axis, and the spin axis of the satellite is parallel to the z axis.

In Fig. 13, the voltage induced by the motion of the satellite through the plasma as calculated from the model geomagnetic field is shown for each excitation voltage and frequency step. These data are referred in time to the center of each step.

C. ION TRAP PROGRAM

The SMAC data is also processed by the ION program. This program determines the total ion density, the ion temperature, and the fractional abundance of O^+ using data from the planar ion trap. The data is presented as tables and plots for each RTS acquisition. An example is shown in Figs. 14 and 15.

D. FOURIER ANALYSIS PROGRAM

Amplitude calibrations for the broadband analog current and voltage waveform data from the automatic gain control amplifiers are determined by the VLF program and fed to the Fourier Analysis Program together with the digitized current and voltage waveform date. The Fourier Analysis Program computes the amplitude and phase of the impedance of the primary dipole antenna using four cycles at each frequency. The program also computes the amplitude of each harmonic of the current waveform.

APPROXIMATE IMPEDANCE MAGNITUDE

FREQ	10MV	100MV	1V	3V	10V	30V	100V	PASS
.40	3.644	14.620	25.416	45.418	53.560	44.614	44.134	0.000
.73	2.261	12.935	34.146	36.765	48.195	58.431	59.975	0.000
1.30	4.036	14.381	30.581	41.879	56.930	60.919	64.898	0.060
2.30	3.613	11.238	21.047	47.536	32.008	37.767	50.741	0.000
3.90	3.691	14.089	27.597	65.683	29.621	37.062	40.762	0.000
7.35	1.966	9.858	17.064	39.192	17.270	24.266	36.073	0.000
14.35	2.691	6.085	6.960	11.200	7.355	7.323	5.617	0.000

ASPECT DATA---ANGLE BETWEEN B AND Y

FREQ	10MV	100MV	1V	3V	10V	30V	100V	PASS
.40	150.824	133.960	116.896	99.774	82.630	65.458	48.421	31.496
.73	42.379	25.512	10.002	12.001	27.971	44.891	51.983	79.126
1.30	124.598	141.615	158.297	172.061	164.204	147.898	130.955	113.963
2.30	42.007	59.066	76.202	93.356	110.502	127.617	144.615	161.212
3.90	15.282	8.359	22.375	39.063	56.082	73.191	90.335	107.484
7.35	96.719	79.567	62.431	45.357	28.460	12.532	9.923	25.195
14.35	173.045	161.601	145.026	128.014	110.898	93.750	76.591	59.451

ANGLE BETWEEN V AND X

FREQ	10MV	100MV	1V	3V	10V	30V	100V	PASS
.40	136.887	119.727	102.500	85.258	68.020	50.822	33.747	17.167
.73	24.501	9.472	13.403	29.495	46.474	63.635	80.851	99.078
1.30	140.105	156.952	171.579	165.466	149.148	132.118	114.942	97.713
2.30	58.850	76.053	93.303	110.533	127.720	144.797	161.403	172.799
3.90	7.152	20.210	36.958	54.071	71.279	88.513	105.754	122.972
7.35	80.469	63.243	46.077	29.088	13.000	9.608	24.820	41.710
14.35	161.071	144.427	127.348	110.152	92.924	75.696	58.489	41.360

Fig. 12. Typical printout by VLF program. (This page contains the magnitude in kilohms of the impedance of the primary dipole antenna calculated using the assumption that only the fundamental frequency is present in the current waveform. This page also contains aspect data. (B, y) is the angle in degrees between the geomagnetic field and the axis of the primary dipole antenna and (V, x) is the angle in degrees between the satellite velocity vector and the thrust axis of the propulsion module.)

-28-

| | | | (V X B) . L | | | | | |
FREQ	10MV	100MV	1V	3V	10V	30V	100V	PASS
.40	.076	-.039	-.150	-.247	-.322	-.367	-.378	-.355
.73	-.350	-.308	-.238	-.147	-.043	.065	.167	.253
1.30	.374	.363	.318	.245	.149	.040	-.073	-.179
2.30	.034	.142	.236	.309	.353	.365	.344	.291
3.90	-.299	-.216	-.113	-.001	.112	.214	.296	.351
7.35	-.268	-.332	-.365	-.366	-.333	-.270	-.182	-.077
14.35	.212	.113	.005	-.104	-.203	-.283	-.336	-.360

Fig. 13. Typical printout by the VLF program. (This page contains the computed value of the voltage, $\overline{v} \times \overline{B} \cdot \boldsymbol{l}$, induced along the antenna by its motion through the plasma in the presence of the geomagnetic field.)

φV1-21 REV 84.4 VTS

	U.TIME	MAG.AT	SOLZEN	N TOTAL	TEMP	VAR*1.0E5	O+/10
1	82620.00	59.01	54.19	0.	0.	0.	0.
	82630.00			0.	0.	0.	0.
2	82665.74	56.62	53.61	4.9304130E+04	2.0770480E+03	1.0525000F+02	4.2364150E+03
	82675.74			4.9128180E+04	2.6500180E+03	2.0747000E+01	4.6189460E+03
3	82706.73	54.23	52.89	4.7828840E+04	2.6248570E+03	4.1616000E+02	4.2735200E+03
	82716.73			4.5686400E+04	2.8992910E+03	1.4461000E+01	4.5592500E+03
4	82749.00	51.83	52.25	4.2806500E+04	1.8154520E+03	3.2487000E+03	3.4819000E+03
	82759.00			4.1902270E+04	2.8377960E+03	2.7263000E+02	3.7843660E+03
5	82788.04	49.42	51.68	5.1719500E+04	2.3750000E+03	4.5611000F+02	4.3982330E+03
	82798.04			5.2015540E+04	3.0884380E+03	1.5687000E+01	4.6970330E+03
6	82828.32	47.02	51.19	5.5210370E+04	2.1310710E+03	9.2767000F+02	4.5884390F+03
	82838.32			5.5751170E+04	2.8794220E+03	4.4065000E+01	4.9155080E+03
7	82869.70	44.62	50.78	5.6311730F+04	2.3750000E+03	1.1173000E+02	4.8908380E+03
	82879.70			5.7161630E+04	2.9771070E+03	1.2954000E+01	4.8398790E+03
8	82909.34	42.21	50.44	5.9015370E+04	2.6979070E+03	3.5970000E+02	4.7495120F+03
	82919.34			5.8965250E+04	2.3834010E+03	1.7393000E+02	5.0586050F+03
9	82951.28	39.80	50.20	6.0035330E+04	2.2317990E+03	1.3114000E+02	4.7999110E+03
	82961.28			5.9684180E+04	2.2915100E+03	2.0530000E+02	4.8864020E+03
10	82992.15	37.40	50.03	6.0755310E+04	2.3655060F+03	2.1524000E+02	4.8648400E+03
	83002.15			6.2045040E+04	3.3103920E+03	8.6476000E+01	5.7562020E+03
11	83032.87	34.94	49.95	0.	0.	0.	0.
	83042.87			0.	0.	0.	0.
12	83073.76	32.58	49.96	6.9014990E+04	2.6768500E+03	8.4589000E+02	5.8094300E+03
	83083.76			6.8571840E+04	2.8231500E+03	6.8513000E+01	6.0723290E+03
13	83114.67	30.17	50.05	7.1921020E+04	2.7291150F+03	1.2950000E+02	6.0424410F+03
	83124.47			7.2303450E+04	2.8765620E+03	9.0681000E+01	6.3555740F+03

Fig. 14. Typical printout by Ion Density program.
(The parameters are the Universal Time in
seconds, the magnetic latitude in degrees,
the solar-zenith angle in degrees, the total
ion density in particles per cubic centimeter,
the ion temperature in degrees Kelvin, the
ion temperature in degrees Kelvin, the variance
of the fit to the ion trap data and the oxygen ion
density divided by 10 in particles per cubic
centimeter.)
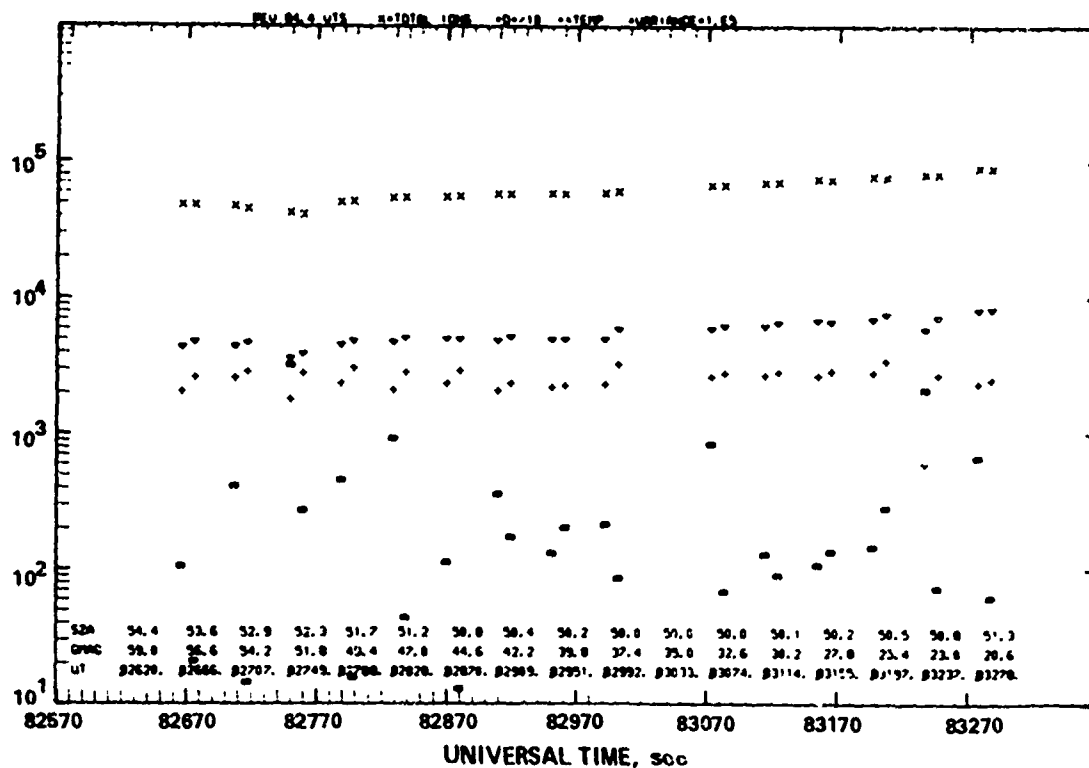
Fig. 15. Microfilm plot of the total ion density in cm^{-3} ($\times$), oxygen
ion density divided by 10 in cm^{-3} (∇), ion temperature in
$°K(+)$, and 10^5 times the variance of the fit to the planar
ion trap data ($\boxdot$). (The data is plotted as a function of
Universal Time in seconds. The solar-zenith angle and
magnetic latitude in degrees are annotated on the plot.
Data acquired at Vandenberg Tracking Station during
Rev. 84 on 12 August 1971.)

-31-

The voltage waveform is sinusoidal and expressed as

$$V_i = V_o/2 + V_{s1} \sin \omega t_i + V_{c1} \cos \omega t_i \qquad (7)$$

where

$$V_o = \frac{2}{(N-1)\,\Delta t} \sum_{j=1}^{N} V_j \,\Delta t \qquad (8)$$

$$V_{s1} = \frac{2}{(N-1)\,\Delta t} \sum_{j=1}^{N} V_j \sin \omega t_j \,\Delta t \qquad (9)$$

$$V_{c1} = \frac{2}{(N-1)\,\Delta t} \sum_{j=1}^{N} V_j \cos \omega t_j \,\Delta t \qquad (10)$$

In Eqs. (8) to (10) the measured voltage waveform value at t_j is V_j and Δt is the digitization interval.

The current waveform is taken to have L-1 harmonics where L varies with excitation frequency as shown in Tabel II.

Table II. Number of Harmonics Used in the Expansion of
the Current Waveform

Frequency (kHz)	L
0.40	25
0.73	25
1.30	15
2.30	8
3.90	5
7.35	2
14.50	1

The current waveform is then expressed as

$$I_i = I_o/2 + \sum_{n=1}^{L} [I_{sn} \sin n\, \omega t_i + I_{cn} \cos n\, \omega t_i] \qquad (11)$$

where

$$I_o = \frac{2}{(N-1)\,\Delta t} \sum_{j=1}^{N} I_j\, \Delta t \qquad (12)$$

$$I_{sn} = \frac{2}{(N-1)\,\Delta t} \sum_{j=1}^{N} I_j \sin n\, \omega t_i\, \Delta t \qquad (13)$$

and

$$I_{cn} = \frac{2}{(N-1)\,\Delta t} \sum_{j=1}^{N} I_j \cos n\, \omega t_i\, \Delta t \qquad (14)$$

The current waveforms calculated from Eq. (11) using the coefficients calculated from Eqs. (12), (13), and (14), are plotted together with the original digitized waveforms for a visual check of the fits obtained. Several examples are shown in Figs. 16 to 20.

The amplitude of each harmonic of the current waveform is

$$A_n = \left(I_{sn}^2 + I_{cn}^2\right)^{1/2} \qquad (15)$$

By definition the amplitude of the impedance is the rms voltage at the fundamental frequency divided by the rms current at the fundamental frequency. A schematic diagram of the circuit used to measure these parameters is shown in Fig. 21.
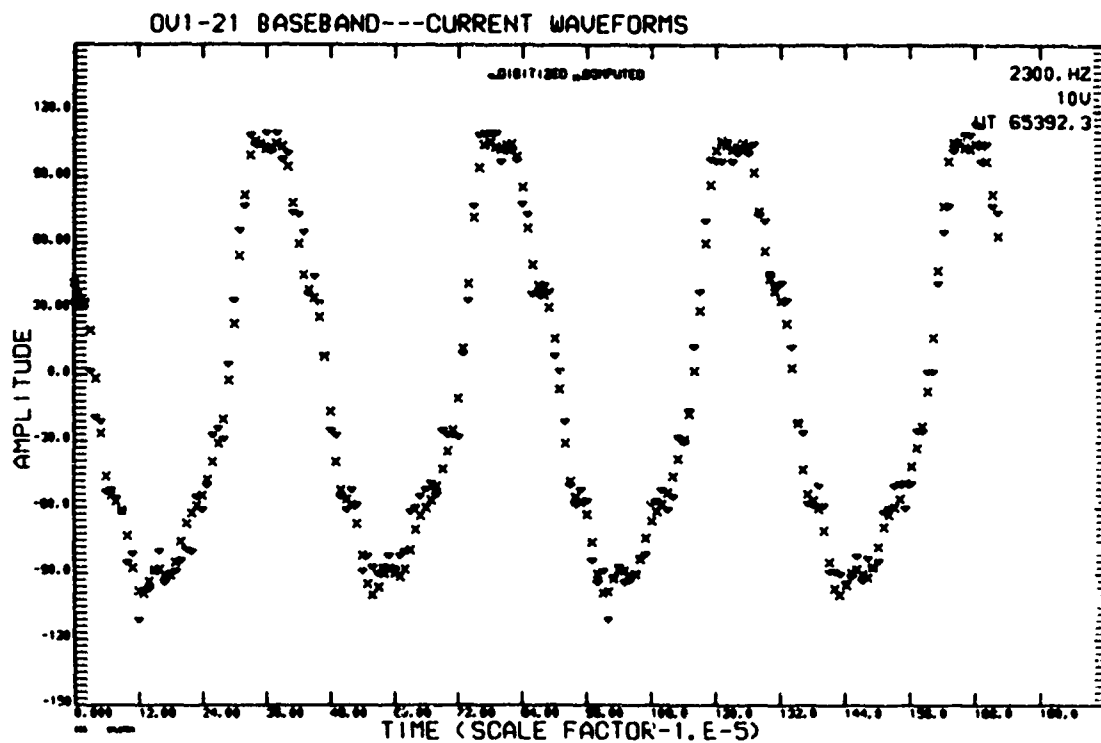
Fig. 16. Microfilm plot showing a comparison of the digitized
current waveform and the waveform computed using
Eq. (11) for 10-V excitation at 2300 Hz. The ion den-
sity is 1.26×10^4 cm^{-3}. (Data acquired at 18.09 UT
on 16 August 1971. Satellite position − alt: 916 km,
INVL: 20.2°; B: 0.262 g, LT: 03:18.)

Fig. 17. Microfilm plot showing a comparison of the digitized
current waveform and the waveform computed using
Eq. (11) for 3-V excitation at 1300 Hz.   The ion density
is 1.36×10^4 cm^{-3}.   (Data acquired at 18:09 UT
on 16 August 1971. Satellite position – alt: 916 km,
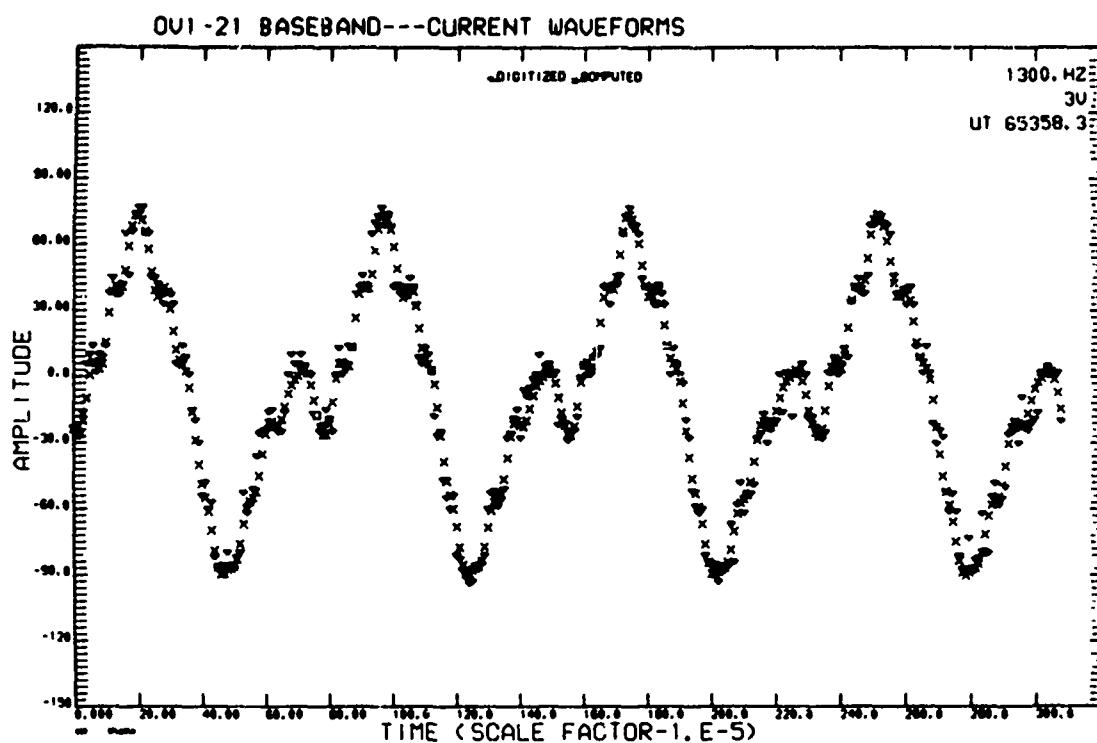INVL: 20.8°, B: 0.268 g, LT: 03:18.)

Fig. 18. Microfilm plot showing a comparison of the digitized
current waveform and the waveform computed using
Eq. (11) for 3-V excitation at 7350 Hz. The ion density
is 1.3×10^4 cm^{-3}. (Data acquired at 18:09 UT
on 16 August 1971. Satellite position — alt: 916 km,
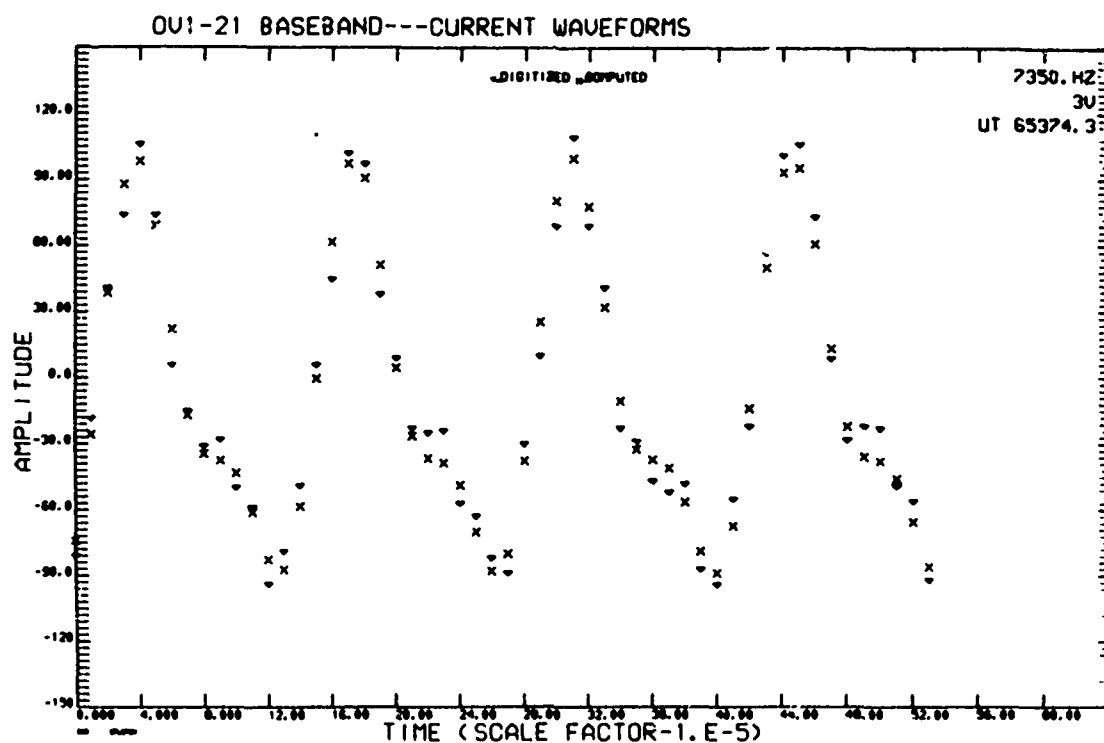INVL: 20.5°, B: 0.265 g, LT: 03:18.)

Fig. 19. Microfilm plot showing a comparison of the digitized current waveform and the waveform computed using Eq. (11) for 30-V excitation at 1300 Hz. The ion density is 1.36×10^4 cm^{-3}. (Data acquired at 18:09 UT on 16 August 1971. Satellite position — alt: 916 km, INVL: 20.8°, B: 0.268 g, LT: 03:18.)
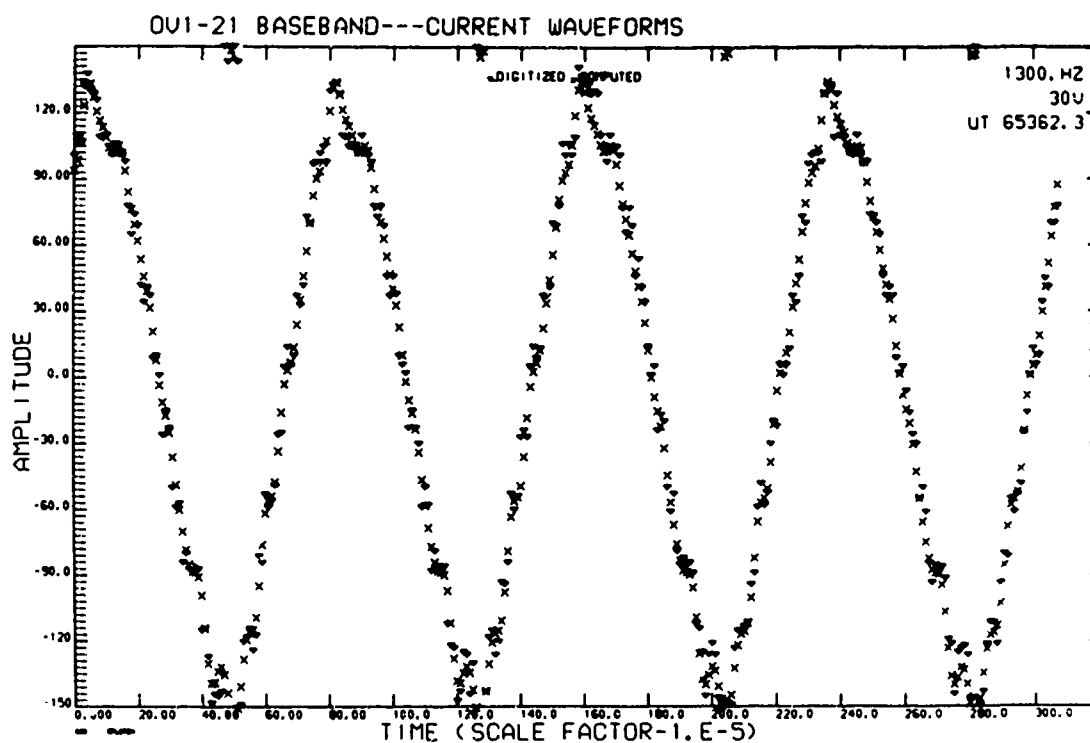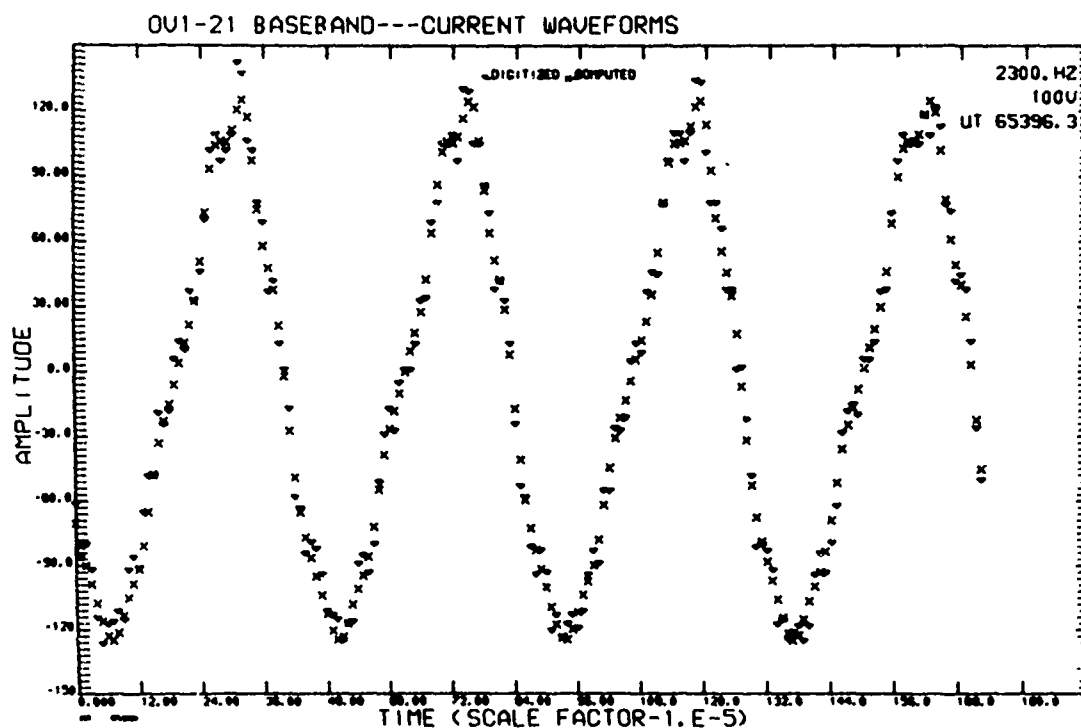
Fig. 20. Microfilm plot showing a comparison of the digitized
current waveform and the waveform computed using
Eq. (11) for 100-V excitation at 2300 Hz. The ion den-
sity is 1.2×10^4 cm^{-3}. (Data acquired at 18:09 UT
on 16 August 1971. Satellite position – alt: 916 km,
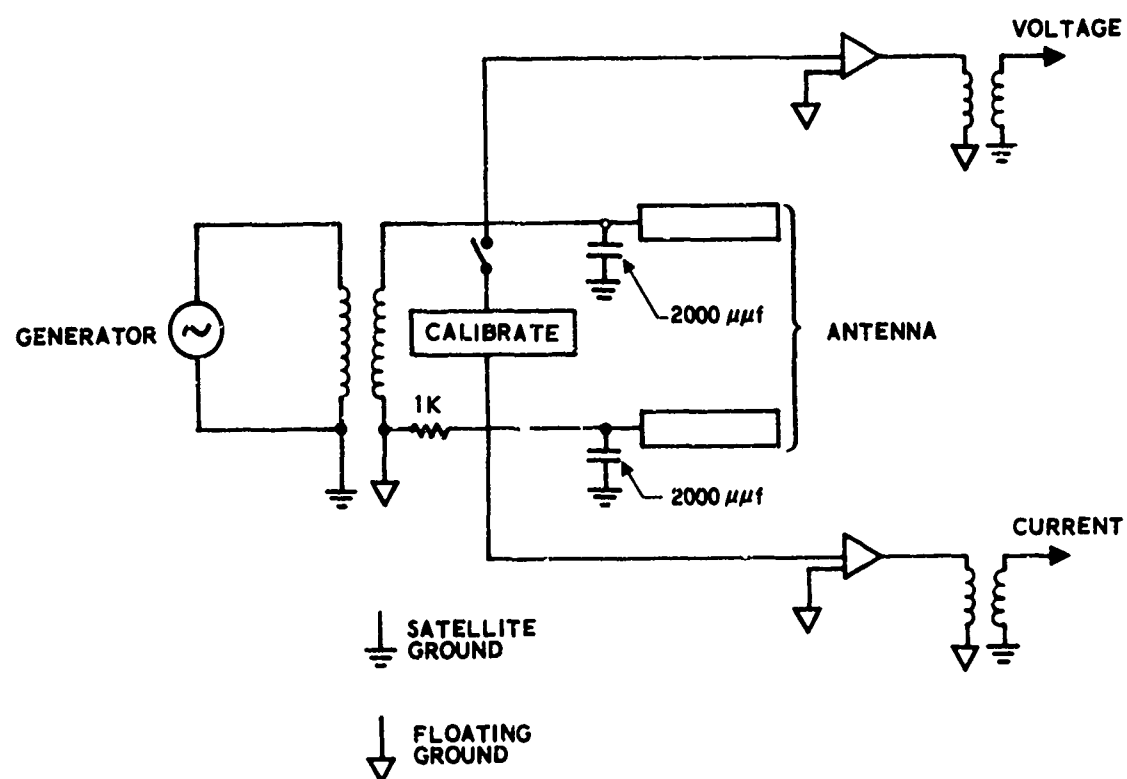INVL: 20.2°, B: 0.262 g, LT: 03:18.)

Fig. 21. Primary dipole excitation and impedance measuring circuit.

The magnitude of the impedance is obtained using Eq. (4) by multiplying the total current, measured by V_{in}, by the ratio of the fundamental current amplitude to the total current amplitude.

$$|Z_L| + 1000 = \frac{V_{ant} G}{I_{1k} (A_1 / \Sigma A_n)} = \frac{1000\ V_{ant} G}{V_{in} (A_1 / \Sigma A_n)} \quad (16)$$

$V_{ant} G$ is tabulated in Table I, V_{in} is obtained from the commutated data, and and $A_1 / \Sigma A_n$ is computed by the Fourier Analysis Program.

The relative phase ϕ_v of the voltage waveform is obtained from Eq. (7)

$$\phi_v = \tan^{-1} V_{s1}/V_{c1} \quad (17)$$

The relative phase ϕ_i of the fundamental frequency of the current waveform is obtained from Eq. (11).

$$\phi_i = \tan^{-1} I_{s1}/I_{c1} \quad (18)$$

The relative phase of the impedance is

$$\phi_z = \phi_i - \phi_v \quad (19)$$

where the convention is chosen that positive ϕ_z represents inductive reactance and negative ϕ_z represents capacitive reactance.

The absolute phase is determined by normalization to the phase of the 100-V excitation step during the calibrate mode. During the calibrate mode, which is turned on by ground command for two minutes each acquisition, resistors and capacitors are switched into the impedance measuring

circuit as shown in Fig. 21. The internal calibration elements are changed with each voltage step as shown in Table III.

Examples of the phase angles obtained during the calibrate mode at a frequency of 2.3 kHz during Rev. 55 are shown as closed circles in Fig. 22. At the lower drive voltages, the impedance of the primary dipole antenna dominates the circuit. As the drive voltage increases, the magnitude of the antenna impedance increases and the impedance of the calibration circuit elements decrease until the 1.0 kΩ calibration resistor at the 100-V step dominates the parallel combination circuit. At the 100-V step, the impedance is essentially 2.0 kΩ resistive (the other 1 kΩ is the current measuring resistor shown in Fig. 21).

The phase angles for an entire acquisition are normalized to the phase angle of the appropriate frequency during the 100-V step of the calibrate mode. This phase angle is taken to be zero. Three blocks of phase angle data from Rev. 55 are shown as open symbols in Fig. 22. These data, taken over a period of eight minutes, vary systematically with voltage step and demonstrate the general consistency of the phase measurements.

Examples of data printed by the Fourier Analysis Program are shown in Figs. 23 to 27.

Table III. Circuit Elements Inserted to Calibrate
the Primary Dipole

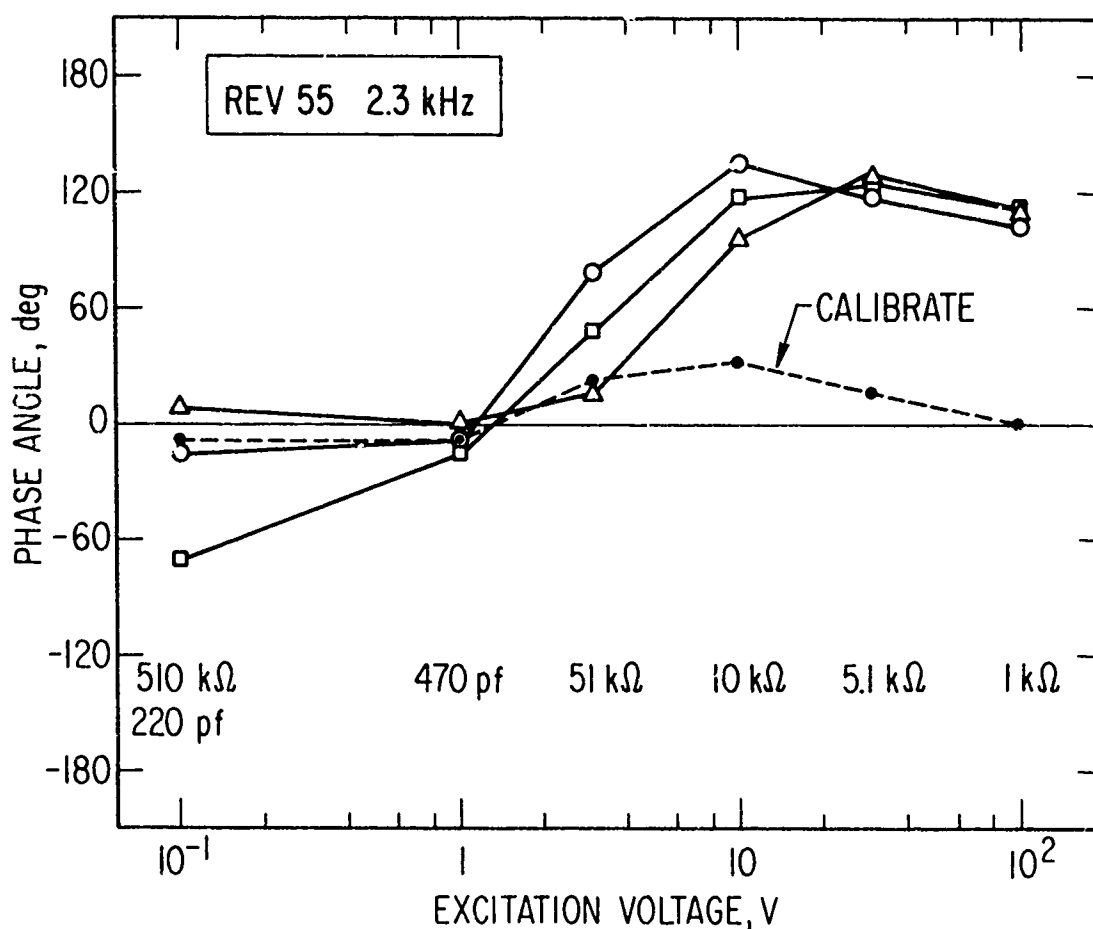| Voltage (V)	Resistance	Capacitance
0.01	1.0 MΩ	-
0.10	510 kΩ	220 pF
1.0	-	470 pF
3.0	51.0 kΩ	-
10.0	10.0 kΩ	-
30.0	5.1 kΩ	-
100.0	1.0 kΩ	-

Fig. 22. Phase angle plotted vs excitation voltage for four blocks of data (indentified by the four symbols) in the SIGNAL mode and one block in the CALIBRATE mode for excitation at 2:3 kHz. (Data acquired between 21:37 and 21.45 UT on 10 August 1971. Satellite position -- alt: 854-818 km, INVL: 67.4-41.3°, B: 0.409-0.328 g, LT: 15:30-15:42. The impedance parameters are the values of the circuit elements placed across the antenna in the CALIBRATE mode.)

Figure 23 contains the amplitude of each harmonic of the current waveform for excitation at 2.3 kHz. The units are arbitrary. The harmonics read from left to right with the fundamental listed first for each voltage step.

In Fig. 24, the phase for each frequency during the 100-V step of the calibration mode is printed out. The phase angles of the impedance for each voltage step are tabulated by block at the bottom of the page. The angles are taken relative to those of the 7th voltage step of the calibration mode as explained above. On the next two pages shown in Figs. 25 and 26, the amplitude of the fundamental A, and the amplitude of the total current ΣA_n = ATOT are printed in arbitrary units for each data block.

Finally the magnitude of the impedance calculated from Eq. (16) is printed for each block in Fig. 27. The 0.01-V p-p data are deleted because the signal-to-noise ratio in the broadband data was too small to obtain a good fit with the Fourier Analysis Program and the channels measuring V_{in} were dominated by noise. Although the broadband data were acceptable for the 0.1-V p-p excitation, the channels measuring V_{in} were still dominated by noise. Hence, the impedance data at 0.1 V p-p are not valid. Both the broadband and AGC data (i.e., V_{in}) were measured with adequate signal to noise at all excitation voltages from 1 to 100 V p-p. In some instances, the low gain commutated data measuring V_{in} were saturated during the 30-V p-p excitation. At these times, the broadband data were generally valid and could be used to determine the phase of the impedance. However, the magnitude could not be obtained since the measurement of V_{in} was invalid.

All of the reduced data were carefully checked for each of these anomalies. Only broadband and commutated data free from such anomalies were used in the parametric studies discussed in section VII.

```
AMPLITUDES FOR  8 HARMONICS AT  2.30 KHZ
VOLTAGE STEP 1
   .137E+02  .168E+01  .154E+01  .162E+01  .205E+01  .214E+01  .278E+01  .136E+01
VOLTAGE STEP 2
   .530E+02  .170E+00  .365E+01  .403E+00  .352E+01  .976E+00  .258E+00  .112E+00
VOLTAGE STEP 3
   .992E+02  .823E+01  .778E+00  .270E+01  .150E+01  .231E+01  .667E+00  .298E+01
VOLTAGE STEP 4
   .850E+02  .276E+02  .478E+01  .203E+01  .373E+01  .304E+01  .240E+01  .311E+01
VOLTAGE STEP 5
   .102E+03  .173E+02  .673E+01  .248E+01  .353E+01  .469E+01  .104E+01  .137E+01
VOLTAGE STEP 6
   .106E+03  .817E+01  .190E+01  .841E+00  .260E+01  .631E+01  .160E+01  .428E+00
VOLTAGE STEP 7
   .104E+03  .188E+02  .863E+01  .423E+01  .636E+01  .151E+02  .824E+01  .287E+01
```

Fig. 23.   Typical printout by Fourier Analysis Program.
(This page contains the amplitude of the current
waveform at the fundamental frequency, 2.3 kHz
in this case, and the first seven harmonics. The
units are arbitrary.)

-44-

7TH VOLTAGE CAL MODE P'ASE

.40	3.90	1.30	7.35	2.30	14.35	.73	
33.15	87.64	.31.19	80.79	-53.61	74.63	48.05	

PHASE ANGLES RELATIVE TO 7TH VOLTAGE CAL MODE
BLOCK START TIME 71271.0

.40	-116.213	-96.750	-81.779	-79.483	-31.614	-16.029	.339
.73	-18.576	7.373	-135.701	-78.245	-14.048	-122.424	-78.191
1.30	-73.123	-104.753	-35.733	-68.828	-34.619	-42.441	-61.417
2.30	33.033	142.335	22.422	75.338	28.801	102.231	-8.792
3.90	-277.055	-130.363	-25.995	-89.254	-122.769	-73.955	6.357
7.35	-128.643	-96.567	-45.928	-56.389	-27.688	1.069	6.388
14.35	172.895	79.507	24.420	-232.275	85.179	-295.017	-333.716

BLOCK START TIME 71399.9

.40	-51.219	37.842	42.344	33.569	-110.218	-96.896	-106.181
.73	-12.451	-1.223	-56.910	-71.887	-47.770	18.952	-27.187
1.30	-84.902	-68.836	-46.903	-52.865	-13.291	-85.665	-17.283
2.30	128.867	106.573	61.117	54.757	47.025	52.646	132.177
3.90	-390.263	-82.561	-344.675	-113.979	-20.239	-67.027	-118.014
7.35	-104.461	-20.005	-40.200	-13.456	-28.685	-88.797	-348.642
14.35	-7.983	-323.713	5.533	66.758	77.925	101.944	83.706

Fig. 24.   Typical printout by Fourier Analysis Program.   (This
page contains the phase angle in degrees of the current
waveform with respect to the voltage waveform for the
seventh voltage step of the calibration mode data.   It
also contains the phase angles in degrees for the other
data blocks relative to that of the seventh voltage step
of the calibration mode data.   Data acquired between
19:47 and 19:54 UT on 10 August 1971.   Satellite position –
alt: 888-872 km, INVL: 88.9-78.4°, B: 0.396-0.399 g,
LT: 14:42-15:24.)

```
UNNORMALIZED TOTAL CURRENT AMPLITUDES
BLOCK START TIME  71271.0
     .40    16.204    13.399    67.975    98.941   109.957   129.180   134.296
     .73     8.354    22.390    81.659    82.195    87.820    94.452   128.233
    1.30     6.791    50.925   101.386    87.231    87.520    70.987    86.502
    2.30    13.871    43.178    98.414    92.564    99.291    93.866   111.100
    3.90     6.448    43.376    91.487    84.568    80.021    95.300   100.688
    7.35    17.789    44.868    78.960    69.900    69.223    90.490   109.219
   14.35    24.859    63.807    81.035    86.794    92.049    92.904    92.350


BLOCK START TIME  71399.9
     .40     4.477    47.562    91.660    97.276   115.736   132.665   116.341
     .73     7.957    42.869    99.362    87.340    97.134    87.417   123.936
    1.30    10.530    35.256    99.844    90.944   106.183    78.807    80.443
    2.30    12.383    26.985    85.902    89.909   115.219   106.169   107.713
    3.90    12.058    52.962    96.158    80.630    88.459   110.236   113.413
    7.35    19.025    39.955    75.401    70.349    79.202   100.539   118.992
   14.35    11.835    62.391    85.499    86.554    90.709    96.527    97.708
```

Fig. 25.   Typical printout by Fourier Analysis Program.
(This page contains the total current amplitude
in arbitrary units computed using Eq. (11). Data
acquisition parameters identical to those in Fig. 24.)

UNNORMALIZED FUNDAMENTAL AMPLITUDES
BLOCK START TIME 71271.0

.40	15.847	12.822	66.438	94.360	104.654	125.630	124.741
.73	7.384	21.131	79.647	72.962	79.544	92.207	123.563
1.30	5.933	50.321	100.931	81.043	54.685	52.024	69.447
2.30	13.688	42.208	97.819	84.515	90.285	87.982	108.858
3.90	6.092	43.006	91.383	82.169	74.412	93.387	99.277
7.35	17.532	44.677	78.805	55.166	54.021	78.317	104.078
14.35	24.859	63.807	81.035	86.794	92.049	92.904	92.350

BLOCK START TIME 71399.9

.40	.763	46.996	91.094	94.305	111.065	126.719	108.432
.73	1.598	42.458	98.974	82.855	80.256	84.105	118.950
1.30	8.628	34.524	99.410	84.630	76.639	65.022	66.487
2.30	10.913	26.053	85.638	85.087	99.375	102.670	105.352
3.90	11.913	52.676	95.976	73.189	80.698	107.717	111.962
7.35	18.803	39.512	75.317	59.527	65.503	90.676	113.931
14.35	11.835	62.391	85.499	86.554	90.709	96.527	97.708

Fig. 26. Typical printout by Fourier Analysis Program.
(This page contains the amplitude of the current
waveform at the fundamental frequency in arbi-
trary units. Data acquisition parameters
identical to those in Fig. 24.)

IMPEDANCE MAGNITUDE CALCULATION
VG/(A1/ATOT)*VI

.40	3.0	14.2	42.9	55.4	63.7	44.2	39.9
.73	2.0	11.9	27.6	35.9	49.2	36.9	52.3
1.30	3.8	9.2	18.8	36.1	78.6	85.5	125.8
2.30	1.7	9.7	17.7	33.0	33.6	41.8	78.7
3.90	3.3	10.6	17.8	39.8	25.2	32.7	47.0
7.35	2.7	9.4	12.6	46.1	18.3	24.4	38.5
14.35	2.6	6.0	7.0	11.2	7.2	6.7	5.4

.40	8.7	7.7	14.3	26.0	41.2	40.9	36.4
.73	8.1	5.1	16.8	32.8	68.2	45.6	58.7
1.30	2.2	9.4	18.1	28.5	68.1	71.7	122.2
2.30	1.8	9.6	21.6	29.0	44.6	38.9	72.7
3.90	1.6	8.4	13.6	34.8	23.4	32.8	44.6
7.35	1.6	4.7	11.5	31.5	17.0	21.9	36.8
14.35	2.6	5.9	7.0	11.2	5.9	5.7	4.9

.40	6.8	8.9	18.2	27.8	38.3	40.7	36.2
.73	1.8	5.7	16.9	21.2	12.2	5.1	2.2
1.30	7.7	6.0	23.0	37.5	60.9	72.4	120.8
2.30	3.3	3.5	11.9	34.1	27.5	4.9	2.1
3.90	2.9	10.9	19.1	33.1	29.2	32.7	46.7
7.35	1.4	3.7	11.7	32.7	21.3	26.6	34.9
14.35	1.7	5.2	7.0	11.0	3.8	3.0	1.3

.40	4.6	7.4	25.7	21.9	11.0	4.3	2.2
.73	3.4	5.7	16.9	21.9	13.6	17.3	12.5
1.30	1.9	4.2	13.6	18.9	6.0	5.3	2.3
2.30	1.7	4.5	15.4	19.6	12.9	4.9	79.8
3.90	1.6	4.4	11.9	27.9	14.2	4.7	2.0
7.35	1.5	3.6	8.2	27.4	7.4	4.9	1.7
14.35	2.6	5.9	7.0	11.2	5.9	5.5	4.9

Fig. 27. Typical printout by Fourier Analysis Program. (This
page contains the magnitude of the primary dipole
impedance in kilohms. The columns represent the
seven voltage drive levels in increasing order. Data
acquired during adjacent blocks starting at 19:47 UT on
10 August 1971. At that time the satellite position was
alt: 888 km, INVL: 88.9', B: 0.996 g, LT: 14:42.)

E.   DATA REDUCTION STATUS

The data reduction status as of 30 March 1973 is shown in Table IV.

The data analysis and results contained in this report are based on the data reduced by 30 March 1973.

Table IV.   Data Reduction Summary as of 30 March 1973

Range Tracking Station Acquisitions	252
High Voltage Mode Acquisitions	163
E2 - Field Acquisitions	22
Tapes Received From RTS	248
Tapes Rayspanned	134
Tapes Digitized	175
SMAC Tapes Generated	89
Tapes Processed by VLF Program	56
Tapes Processed by Fourier Analysis Program	20
Tapes Processed by Ion Density Program	21

VII. DATA ANALYSIS

A. PRIMARY DIPOLE IMPEDANCE

The circuit used to measure the impedance of the primary dipole antenna is shown in Fig. 21.

1. LINEAR IMPEDANCE

a. Magnitude

The equivalent circuit that includes the linear ion sheath which surrounds the antenna immersed in the magnetospheric plasma is shown in Fig. 28. The sheath resistance R_{sh} is given by (Refs. 19, 20, 21)

$$R_{sh} = kT_-/e^2 A_+ \left[N_{H+} \left(v_S^2 + v_{H+}^2 \right)^{1/2} + N_{O+} \left(v_S^2 + v_{O+}^2 \right)^{1/2} \right] \qquad (20)$$

where k is Boltzmann's constant, T_- is the electron temperature, N is the electron density, e is the electron charge, A_+ is the ion collection area, v_S is the satellite velocity, v_{H+} is the proton thermal velocity and v_{O+} is the oxygen ion thermal velocity. In an oxygen dominated plasma v_S^2 is the only significant term in the sum. In a hydrogen dominated plasma $v_S^2 \simeq v_{H+}^2 \gg v_{O+}^2$. Equation (20) ignores possible effects caused by the motionally induced $\bar{v} \times \bar{B}$ potential. Such effects have not been observed in the NASC-117 data.)

The sheath capacitance C_{sh} is approximately the capacitance between the antenna element of radius r and the plasma at an effective radius of

$$r_{sh} \sim 2\pi \lambda_D + r \qquad (21)$$

where λ_D is the plasma Debye length (Ref. 12). Thus

$$C_{sh} = 2\pi \epsilon_o \lambda_D l / \ln(r_{sh}/r) \qquad (22)$$

-51-
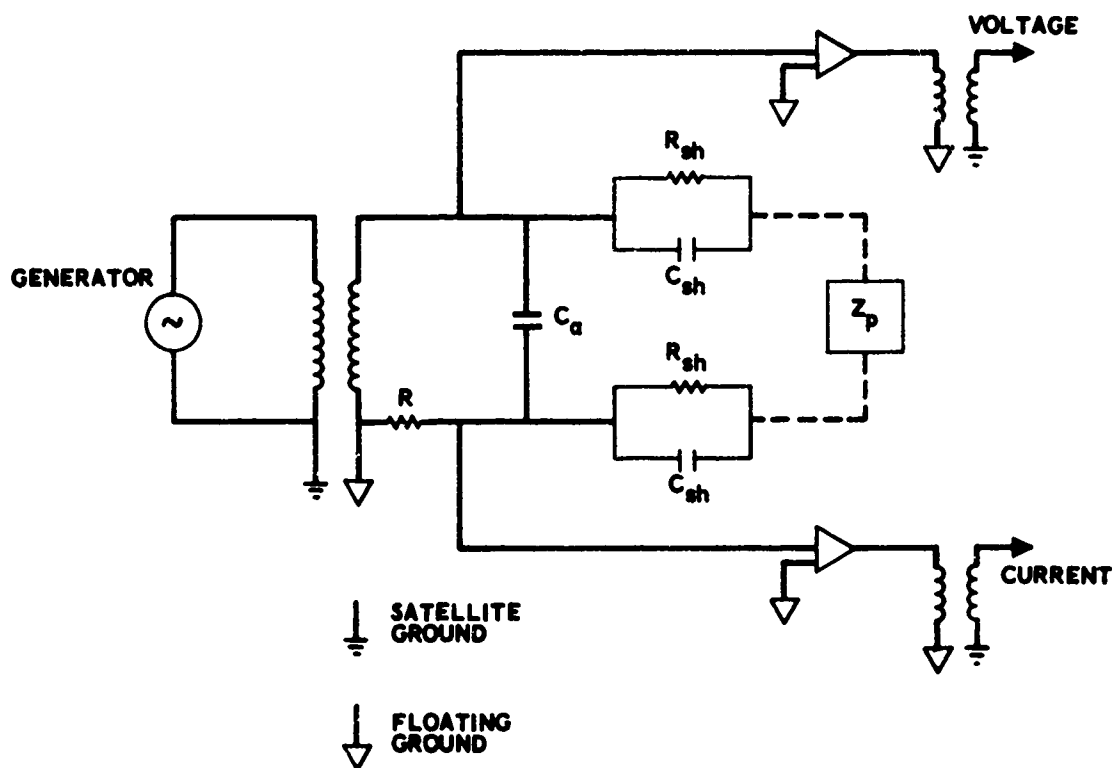
Fig. 28. Equivalent circuit for the linear sheath model of
the primary dipole antenna.

The circuit parameters are listed in Table V.

For the OV1-21 orbit and experiment frequencies, the plasma is assumed to be infinitely conducting. The only exception to this approximation is when the excitation frequency equals the low hybrid resonance frequency. According to available data, when this condition occurs the plasma impedance is about ten percent of the sheath impedance.[1] A swept frequency system would have been more effective for detecting this LHR effect.

Table V. Primary-Dipole Antenna and Impedance Measuring Circuit Parameters

Symbol	Parameter	Value
R	Resistance	$1 \text{ k}\Omega$
C_a	Capacitance	1000 pF
ℓ	Antenna length	16.15 m
r	Antenna radius	0.00635 m
A_+	$2r\ell$	0.205 m^2
v_S	Satellite velocity	7.5 km/sec

The magnitude of the impedance Z_m measured by the circuit (Fig. 28) is then

$$Z_m = R + |2Z_a Z_{sh}/(Z_a + 2Z_{sh})| \qquad (23)$$

where

$$Z_a = 1/j\omega C_a \qquad (24)$$

---

[1] Private communication from Frank Palmer, Communications Research Centre, Ottawa, Canada.

and

$$\frac{1}{Z_{sh}} = \frac{1}{R_{sh}} + j\omega \, C_{sh} \tag{25}$$

and

$$\omega L << R$$

As an example, the values of the sheath resistance and sheath capacitance of the primary dipole antenna calculated from Eqs. (20) and (22) for an electron temperature of 1200°K are plotted as a function of electron density in Fig. 29. The linear impedance Z_m expected for the antenna is plotted as a function of electron density in Fig. 30. It should be noted that over most of the density range applicable to the NASC-117 experiment, the measured linear impedance at the lower frequencies is proportional to T_-/N. Hence, Fig. 30 can be scaled to obtain the value of T_-/N applicable to an individual measurement.

Three examples of the data are shown in Figs. 31 to 33. The impedance measured at 1 V p-p is plotted as a function of frequency in each figure. The data for each plot was obtained over one frequency block or 128 sec. The total ion density N_i and ion temperature T_+ as determined by the planar ion trap during this 128-sec period are included on each figure.

Also included are theoretical curves obtained from Eq. (23). The only free parameter is the electron temperature T_-. The agreement between the value of T_- required to fit the impedance data and the value of T_+ measured by the ion trap in many cases such as those shown in Figs. 31 and 32 is quite good. This represents one of the most complete validations of the linear ion-sheath model for electric antennas in the magnetoplasma.

In some cases, such as the one shown in Fig. 33, there is a marked discrepancy between T_- and T_+ with the value for T_- obtained from the sheath
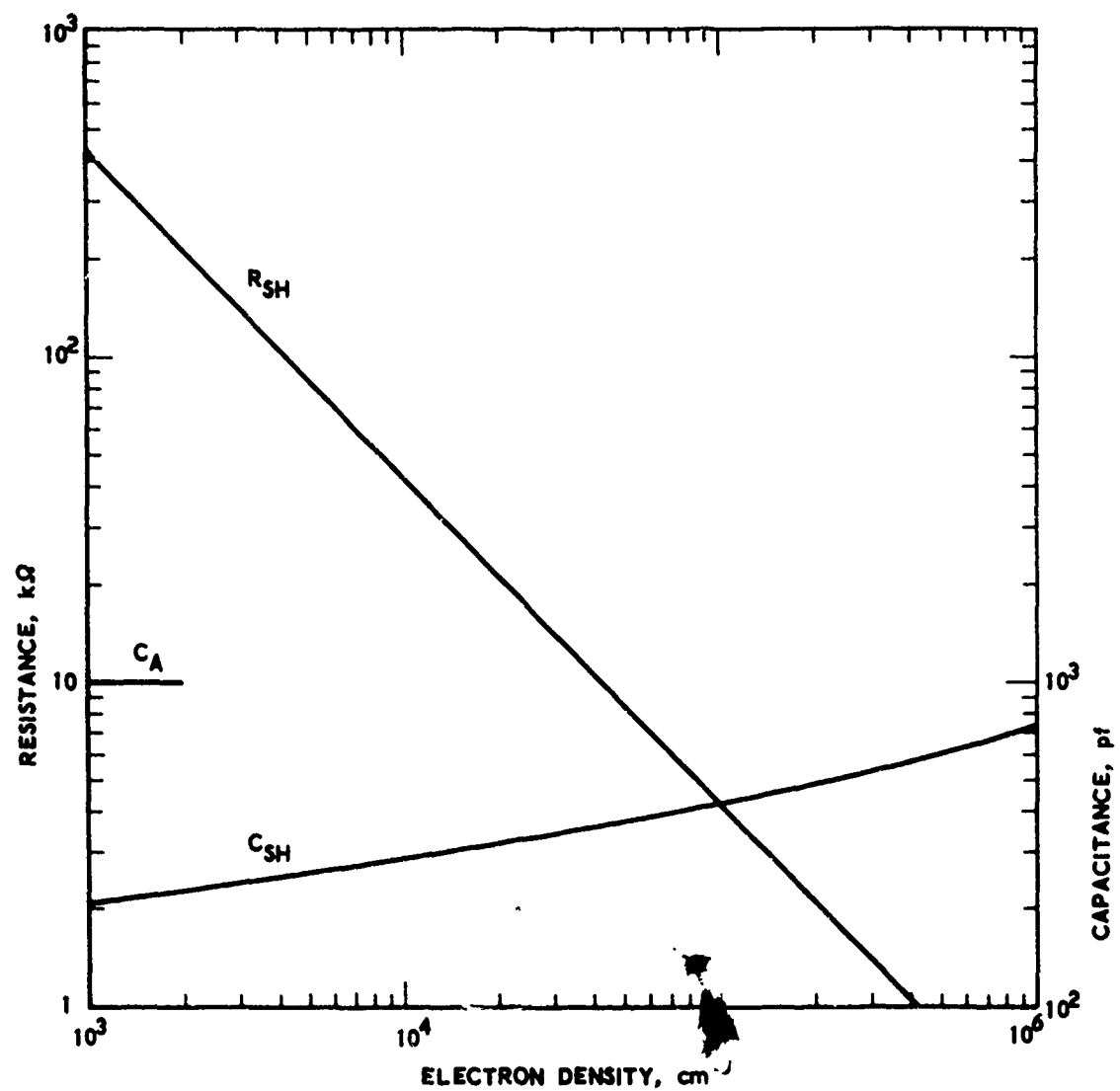
Fig. 29. Sheath resistance and sheath capacitance plotted vs
ambient electron density for a linear ion sheath
surrounding the primary dipole. (The electron
temperature is taken to be 1200°K.)

-55-
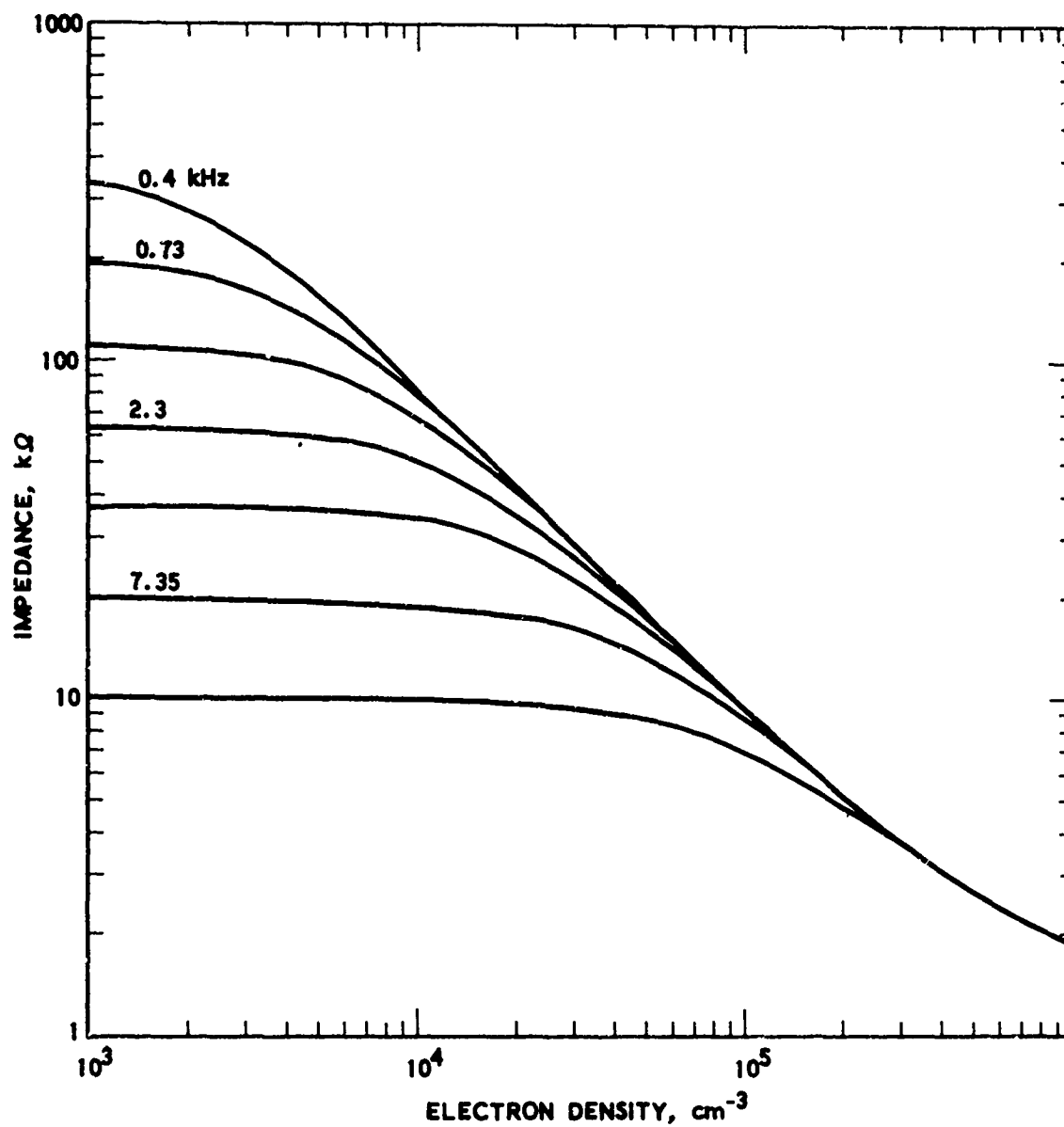
Fig. 30. Value of the measured impedance expected as
a function of electron density as predicted by
linear sheath model.
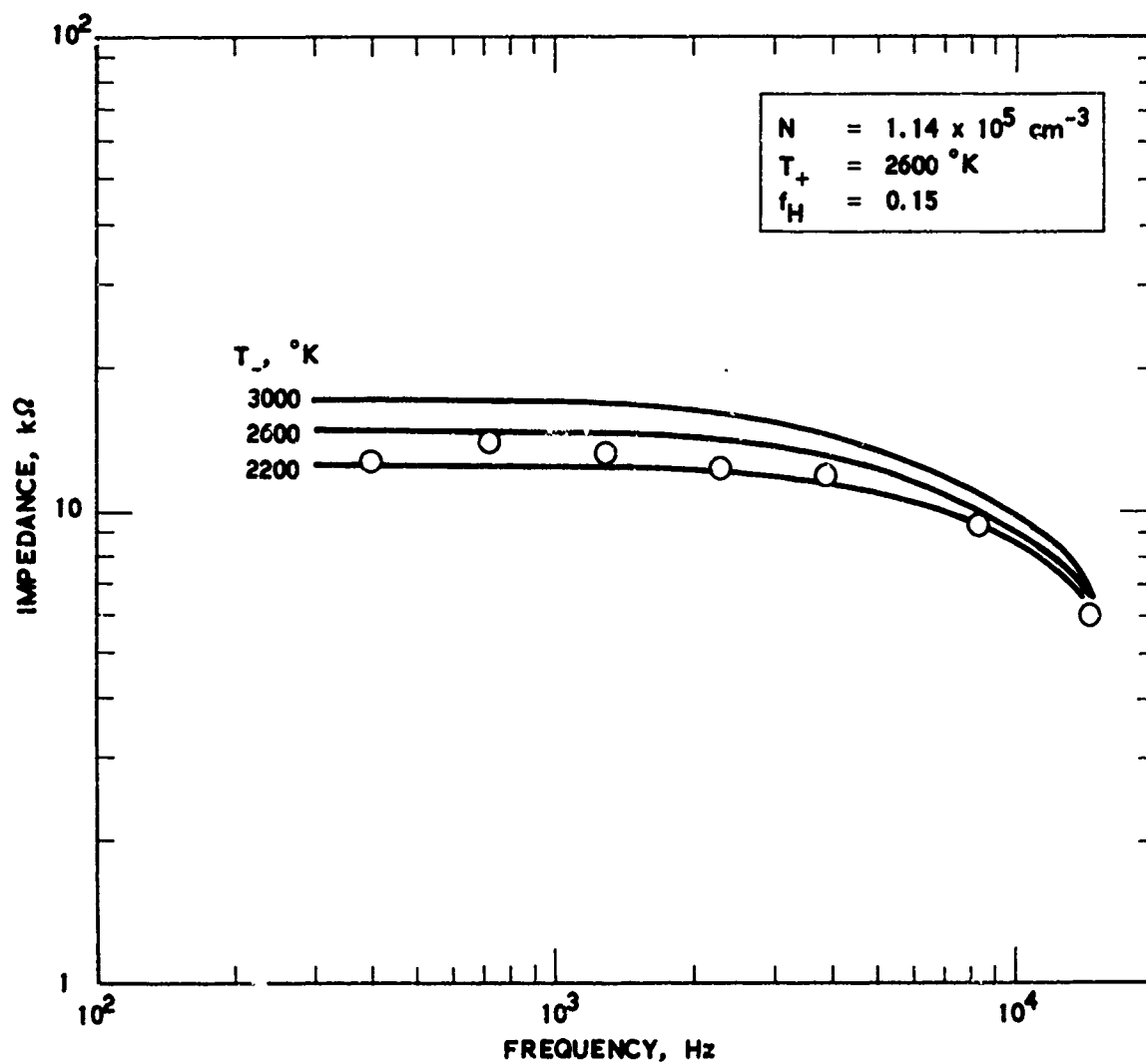
Fig. 31. Impedance measured at 1 V as a function of excitation
frequency for a data block starting at 02:52 on 11 August
1971. (The measured ion density was $1.14 \times 10^5 cm^{-3}$
and the measured ion temperature was 2600°K. The-
oretical curves are drawn for electron temperatures of
2400, 2600, and 3000°K. Satellite position — alt: 817 km,
INVL: 29.1° B: 0.257 g, LT: 15:42.)
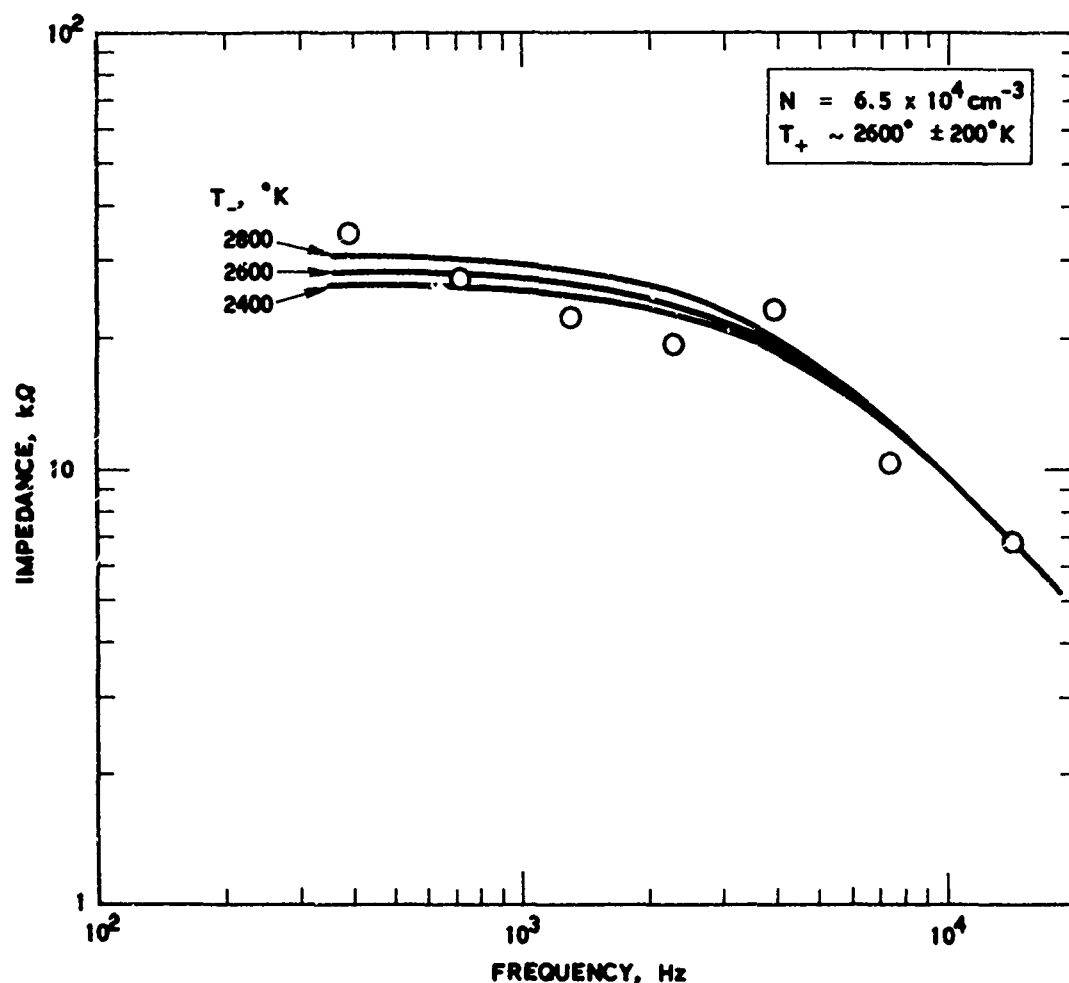
Fig. 32. Impedance measured at 1 V as a function of excitation
frequency for a data block starting at 19:43 UT on
10 August 1971. (The measured ion density was 3.3
$\times 10^4$ cm^{-3} and the measured ion temperature was
2600°K. The theoretical curve is drawn for an elec-
tron temperature of 2400, 2600, and 3800°K.
Satellite position — alt: 903 km, INVL: 76.8,
B: 0.399 g, LT: 05:06.)
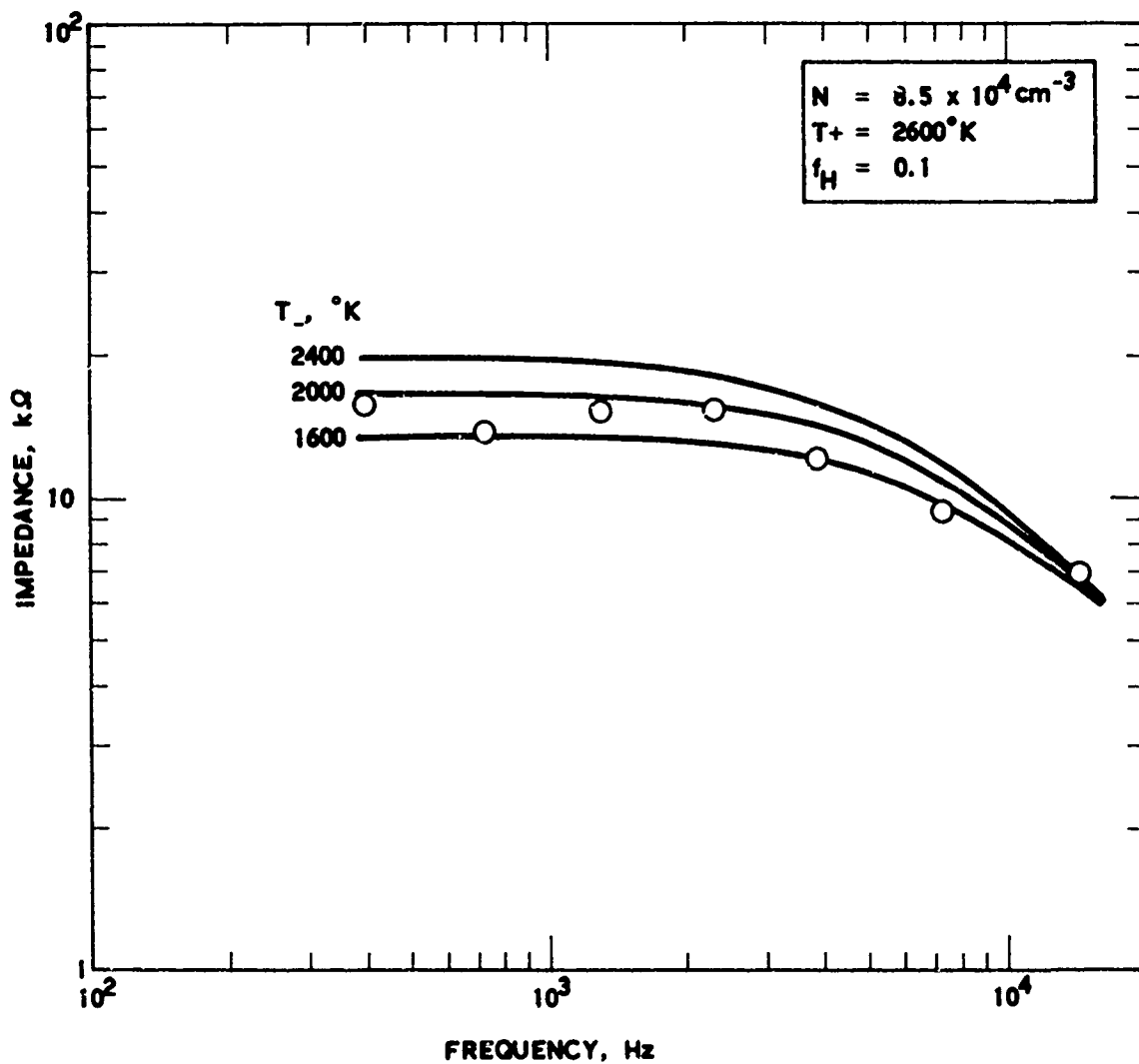
Fig. 33. Impedance measured at 1 V as a function of excitation
frequency for a data block starting at 22:54 UT on
13 August 1971. (The measured ion density was 8.5
$\times 10^4$ cm^{-3}. The measured ion temperature was
2600°K. Theoretical curves are drawn for elec-
tron temperatures of 1600, 2000, and 2400°K.
Satellite position — alt: 807 km, INVL: 34.8°,
B: 0.299 g, LT: 15:24.)

impedance significantly less than the value for T_+ measured by the ion trap. This is a physically unreasonable result and further analysis is planned to determine if ion composition, vehicle potential, or photoelectron currents contribute to this discrepancy.

Analysis of the effect of photoelectron currents on the antenna impedance has been done for a terminator crossing. The impedances measured during the frequency blocks immediately before and after a terminator crossing are shown in Fig. 34. The sheath resistance is decreased by the photoelectron current. Equation (20) for R_{sh} must be modified to account for the photoelectron current by the addition of the term $j_{pe}A_{pe}$ in the denominator, where j_{pe} is the photoemission current density and A_{pe} is the total emission area. Thus

$$R_{sh} = kT_-/[Ne^2 A_+(v_S^2 + v_+^2)^{1/2} + j_{pe} A_{pe}] \qquad (26)$$

Assuming $A_{pe} = A_+$ and $v_S^2 = v_+^2$, Eq. (26) simplifies to

$$R_{sh} = \frac{kT_-/e}{A_+ (\sqrt{2} \ Nev_S + j_{pe})} \qquad (27)$$

The planar ion trap measured $N_i = 1.2 \times 10^{10}$ m^{-3} while $v_S = 7.4$ km/sec during this terminator crossing. Hence, the first term of the sum in the denominator of Eq. (27) is

$$j_i = N_i v_S = 1.96 \times 10^{-5} \ \text{Am}^{-2} \qquad (28)$$

At 1.3 kHz, the impedance drops from 74 kΩ to 19 kΩ between eclipse and sunlight. Assuming there is no change in T_- across the terminator (no change in T_+ was measured by the planar ion trap), the total current in the denominator of Eq. (27) must increase by a factor of 3.9 from
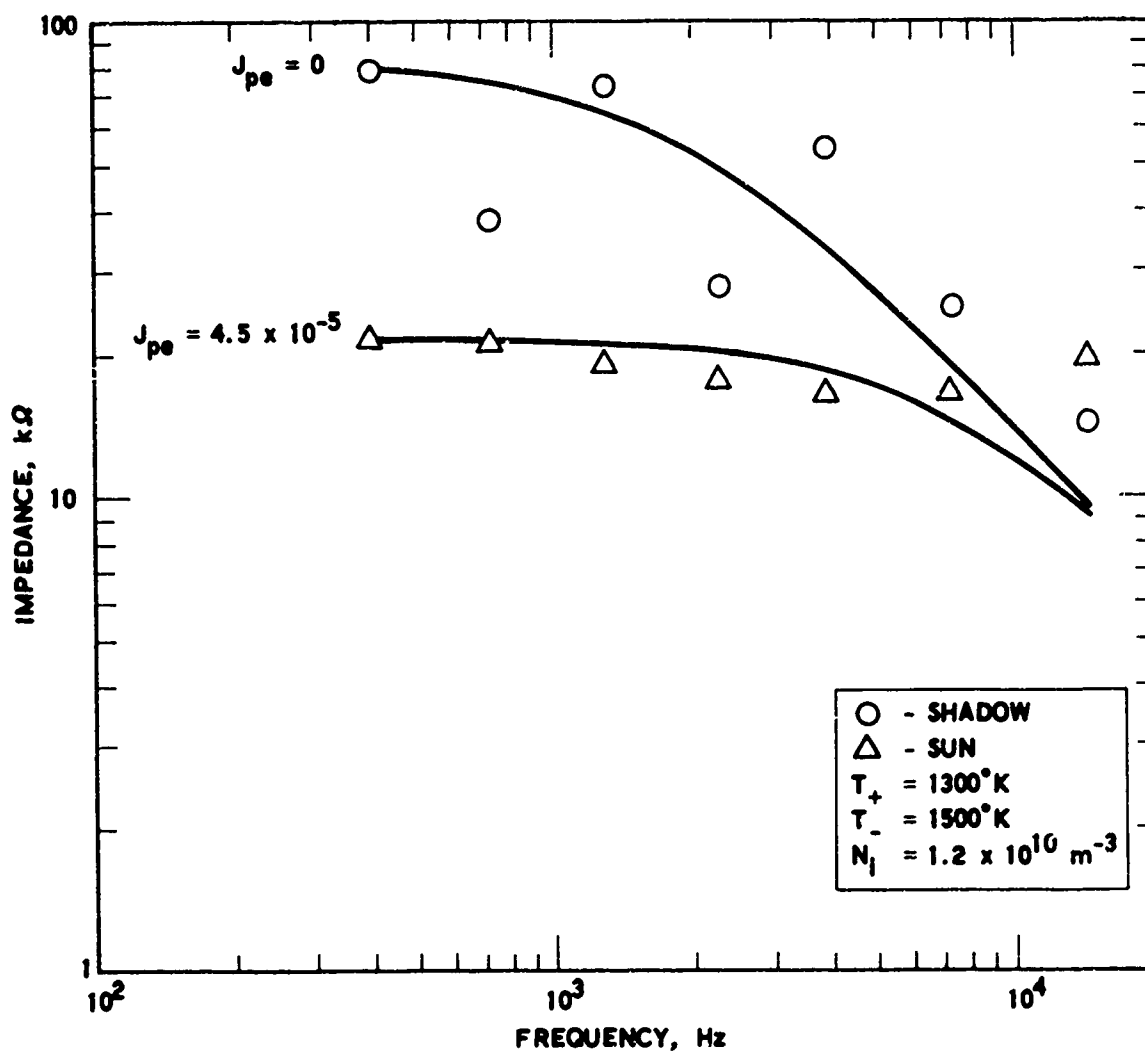
Fig. 34. Impedance measured at 1 V as a function of excitation
frequency for two data blocks between 17:04:59 and
17:11:07 UT on 13 August 1971. (The satellite
crossed the terminator between 17:07:39 and 17:07:55
UT. Satellite position — alt: 916 km, INVL: 18.7°,
B: 0.233 g, LT: 03:30.)

eclipse to sunlight. This yields a value of photoemission current density $j_{pe} = 5.7 \times 10^{-5}$ Am^{-2} for the silvered elements of the primary dipole antenna. This compares favorably with the value of $j_{pe} = 8 \times 10^{-5}$ Am^{-2} for the silver spheres on Injun 5 (Ref. 13).

b.   Density Dependence

The magnitude of the impedance in the linear regime (1V p-p) is plotted at 1.3 and 2.3 kHz as a function of plasma density as measured by the planar ion trap in Figs. 35 and 36. The theoretical curves for $T_- = 2400°$K and theoretical curves for $T_- = 2400°$K with a photoelectron flux $j_{pe} = 6 \times 10^{-5}$ Am^{-2} are included in Fig. 35. Further analysis will be performed to determine if the spread in the data can be attributed to the ion composition, ion temperature, or the ram angle of the electric dipole with respect to the plasma flow.

The relatively low impedances at the lower densities are most likely due to the photoelectron currents from the silvered antenna elements. Data obtained when the satellite is eclipsed yield significantly higher impedances than data when the satellite is illuminated by sunlight.

2.   NONLINEAR IMPEDANCE

a.   Magnitude

The magnitude of the impedance Z_m of the primary dipole is shown as a function of the applied voltage in Fig. 37 for a single frequency block during Rev. 58.4. The magnitude of the impedance increases, as expected as the applied voltage increases. In Table VI, the average impedance magnitudes and the standard deviations are tabulated for all of the available reduced data at 1.3 and 3.9 kHz. Each average was obtained from 47 data points. The maximum and minimum impedance is also tabulated at each voltage level.

The magnitude of the impedance is plotted as a function of the driving frequency in Fig. 38 for a block of data at 21:38 UT during Rev. 55. The line drawn on each plot is the magnitude of the impedance $|1/j\omega\, C_a|$ of the isolation capacitors.
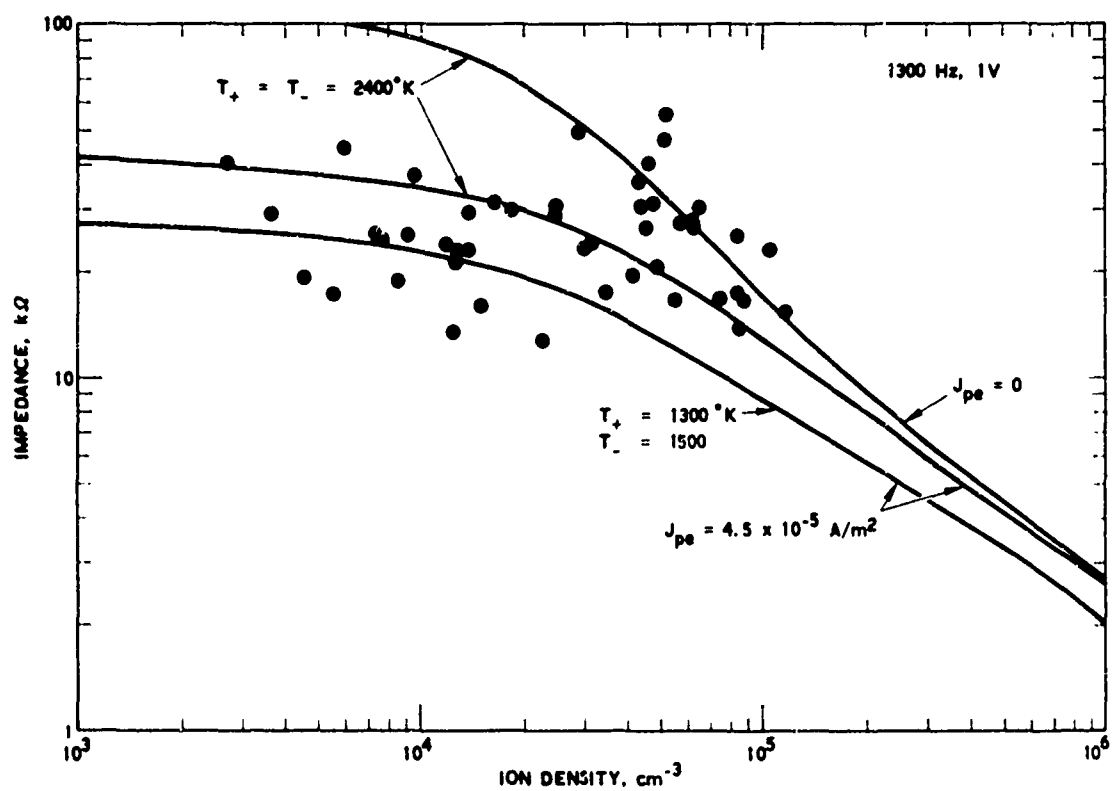
Fig. 35. Impedance measured during 1-V excitation at 1.3 kHz
as a function of ion density.
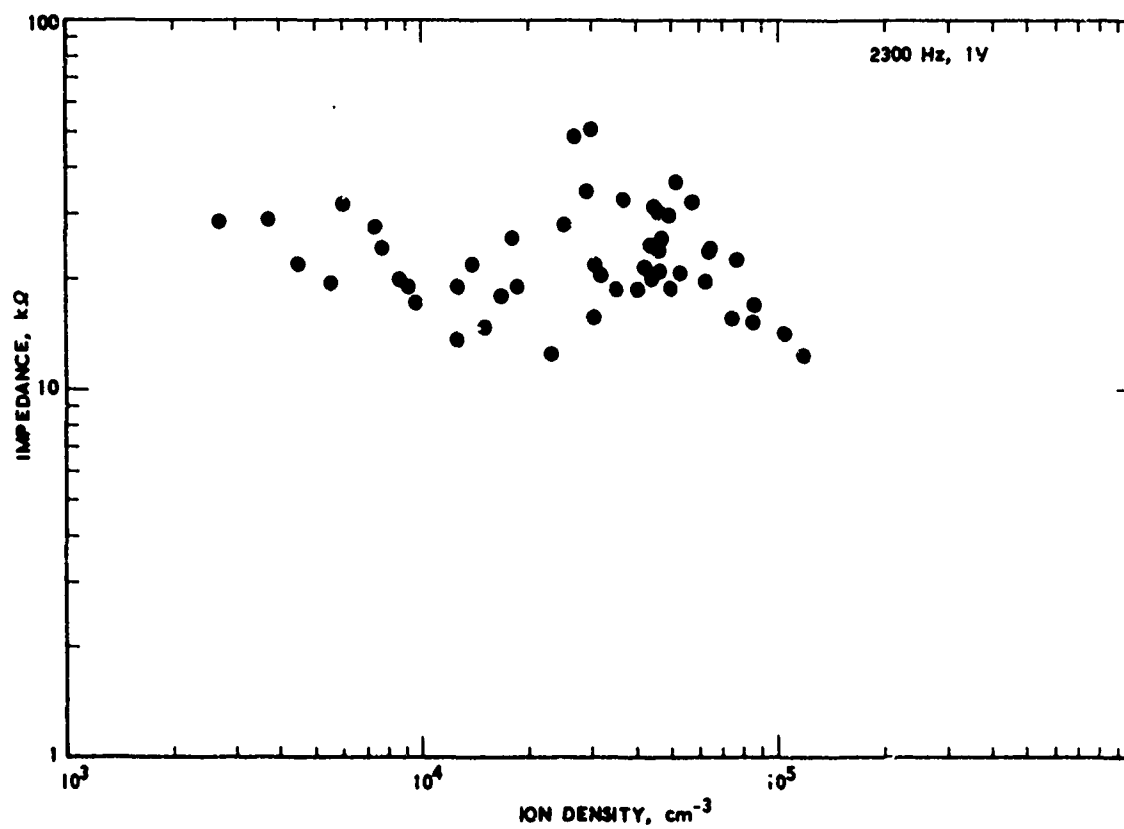
Fig. 36. Impedance measured during 1-V excitation at 2.3 kHz
as a function of ion density.
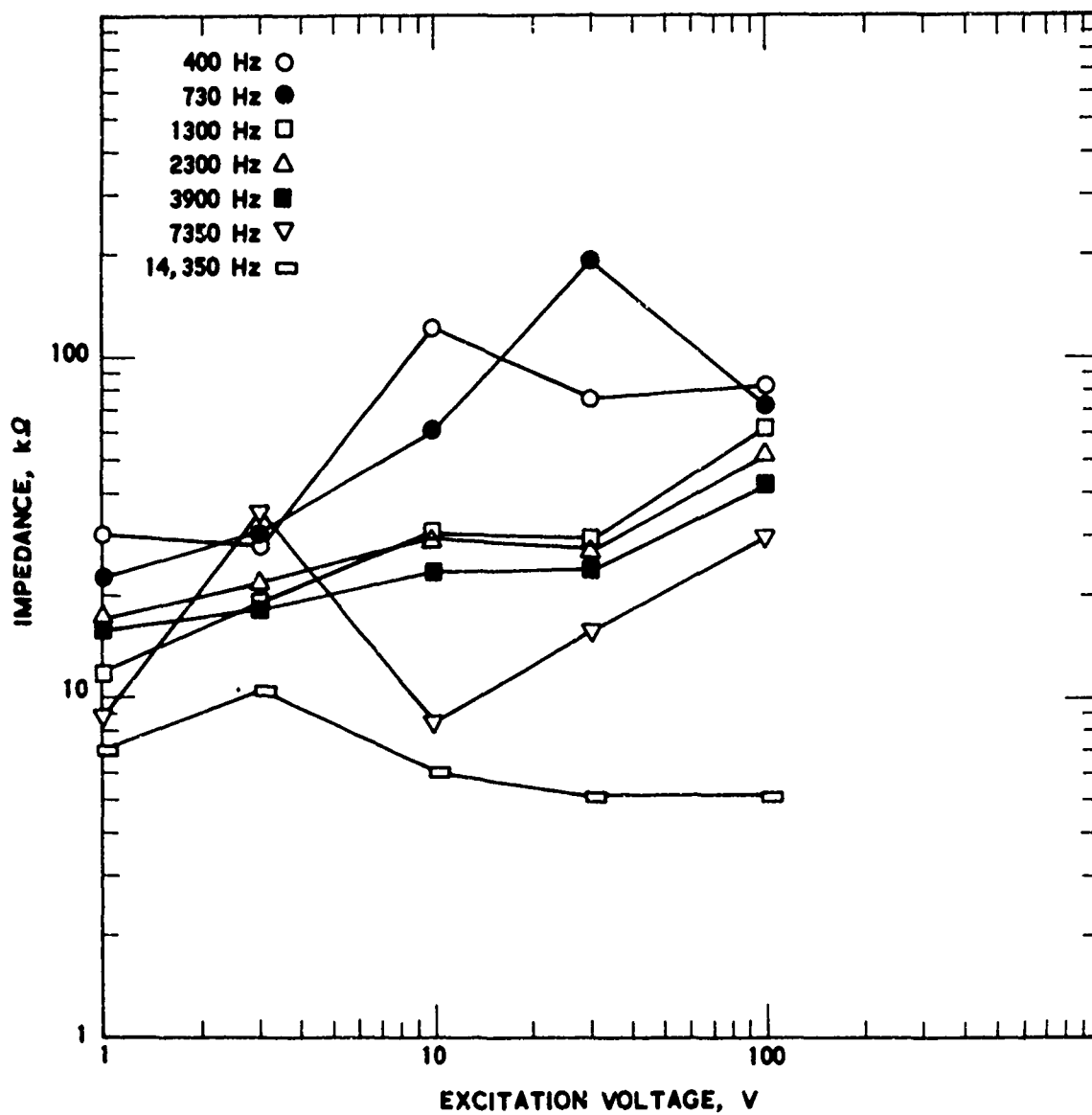
Fig. 37. Primary dipole impedance plotted vs excitation
voltage for the data block starting at 02:50 UT
on 11 August 1971. (Satellite position – alt:
825 km, INVL: 34.5°, B: 0.278 g, LT: 15:42.)
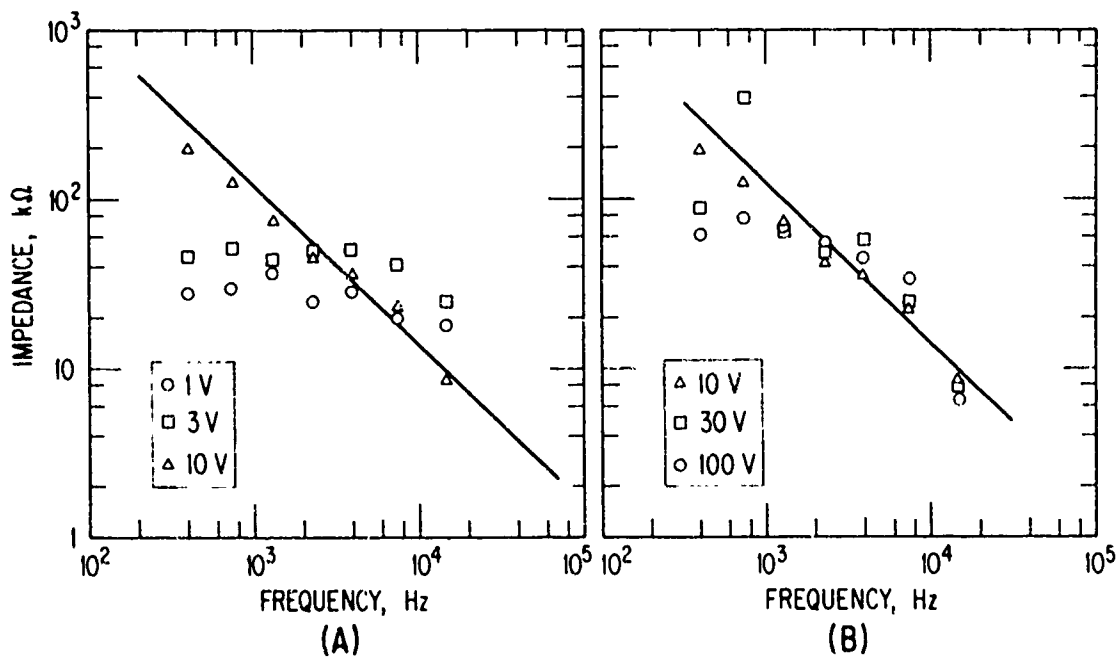
Fig. 38. Primary dipole impedance plotted vs excitation
frequency for the data block starting at 21:37 UT
on 10 August 1971. (Satellite position – alt:
854 km, INVL: 67.5°, B: 0.409 g, LT: 15:30.)

b.   Density Dependence

The magnitude of the impedance in the nonlinear regime (10 to
100 V p-p) is plotted at 400 Hz, 1.3, 2.3, and 3.9 kHz as a function of
plasma density in Figs. 39 to 42.

Table VI.   Average Impedance, Standard Deviation, Maximum and
Minimum Impedance at 1.3 and 3.9 kHz

Excitation Frequency (kHz)	Excitation Voltage (V)	Average Impedance (kΩ)	Minimum Impedance (kΩ)	Maximum Impedance (kΩ)
1.3	10	76.6 ± 23.3	32.8	131.7
1.3	30	68.8 ± 20.2	32.1	118.1
1.3	100	115.1 ± 25.1	54.6	131.8
3.9	10	34.5 ± 7.6	16.2	52.5
3.9	30	34.4 ± 5.6	22.2	41.4
3.9	100	46.9 ± 3.9	40.3	54.8

c.   Comparison with Theory

The magnitude of the impedance of the NASC-117 antenna has been
calculated by means of theory and computer programs by Shkarofsky (Ref. 10).
The input parameters, listed in Table VII, are those appropriate for an
OV1-21 data acquisition during Rev. 58 on 11 August.   The average sheath
conductance and average sheath capacitance obtained from Shkarofsky's cal-
culation are plotted as a function of applied voltage in Fig. 43.   The conduc-
tance predicted for the lower density, $N_i = 1 \times 10^{10}$ m^{-3}, is shown for
comparison.

In Fig. 44, the value of Z_m obtained from Shkarofsky's data in
Fig. 43 using Eq. (23) is plotted as a function of the peak voltage drive.
The measured values of Z_m obtained when $N - 1.2 \times 10^{11}$ are also shown
on the graph for three frequencies
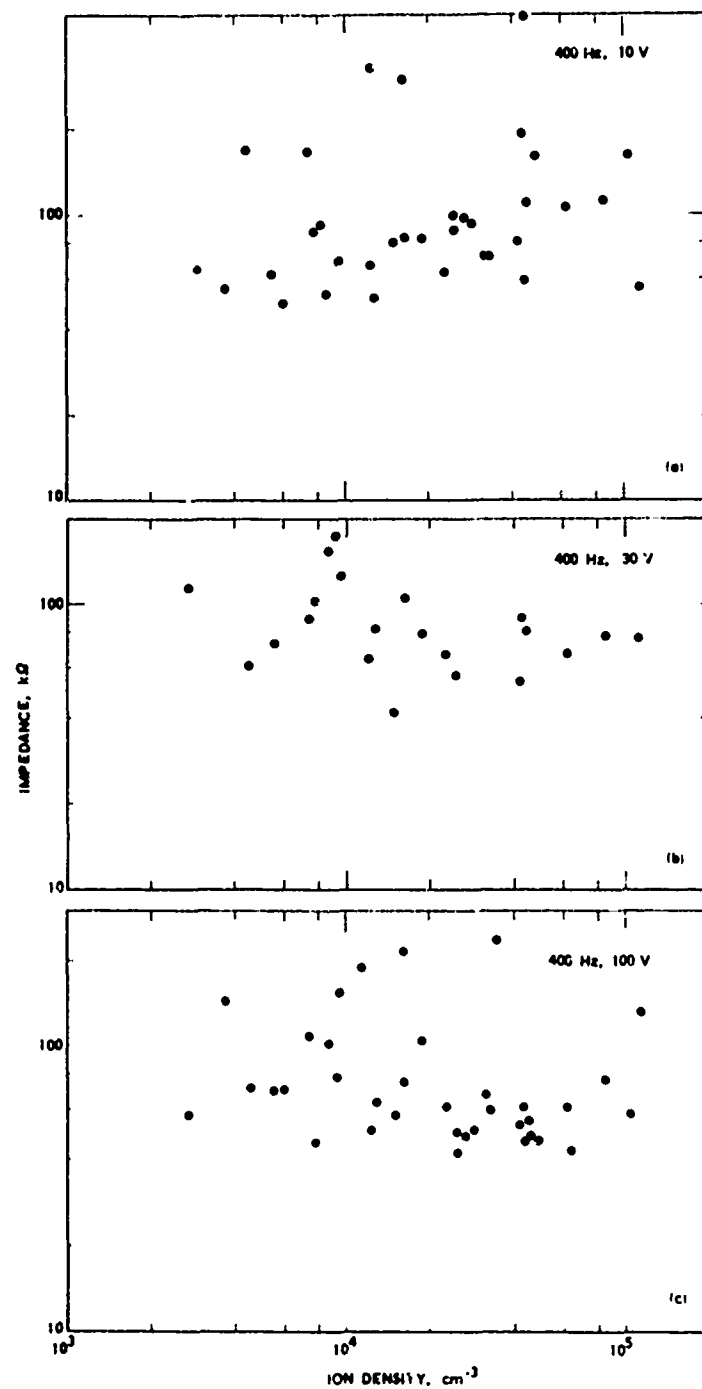
Fig. 39. Primary dipole impedance for 10-,
30-, and 100-V excitation at 400 Hz
as a function of total ion density.
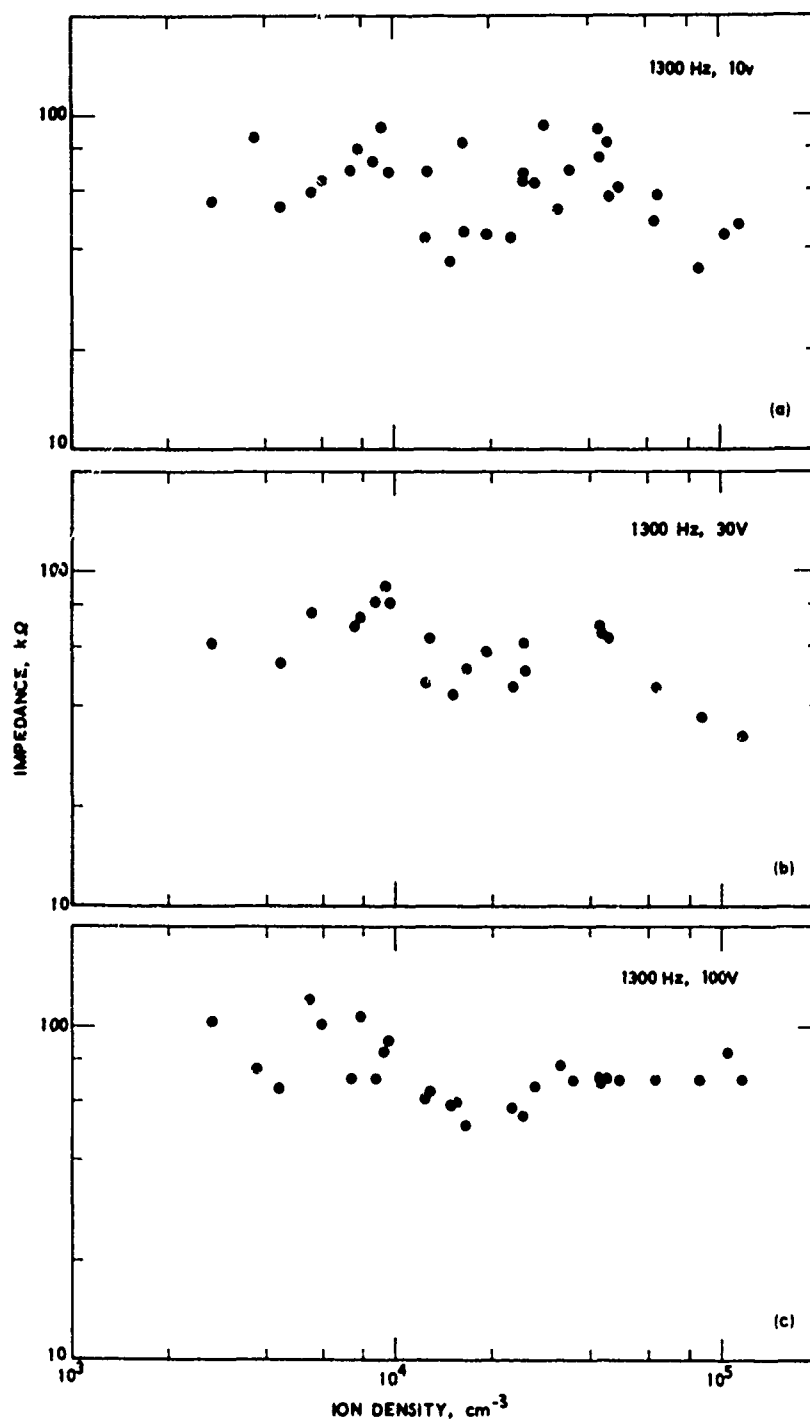
Fig. 40. Primary dipole impedance for 10-, 30-,
and 100-V excitation at 1.3 kHz as a
function of total ion density.
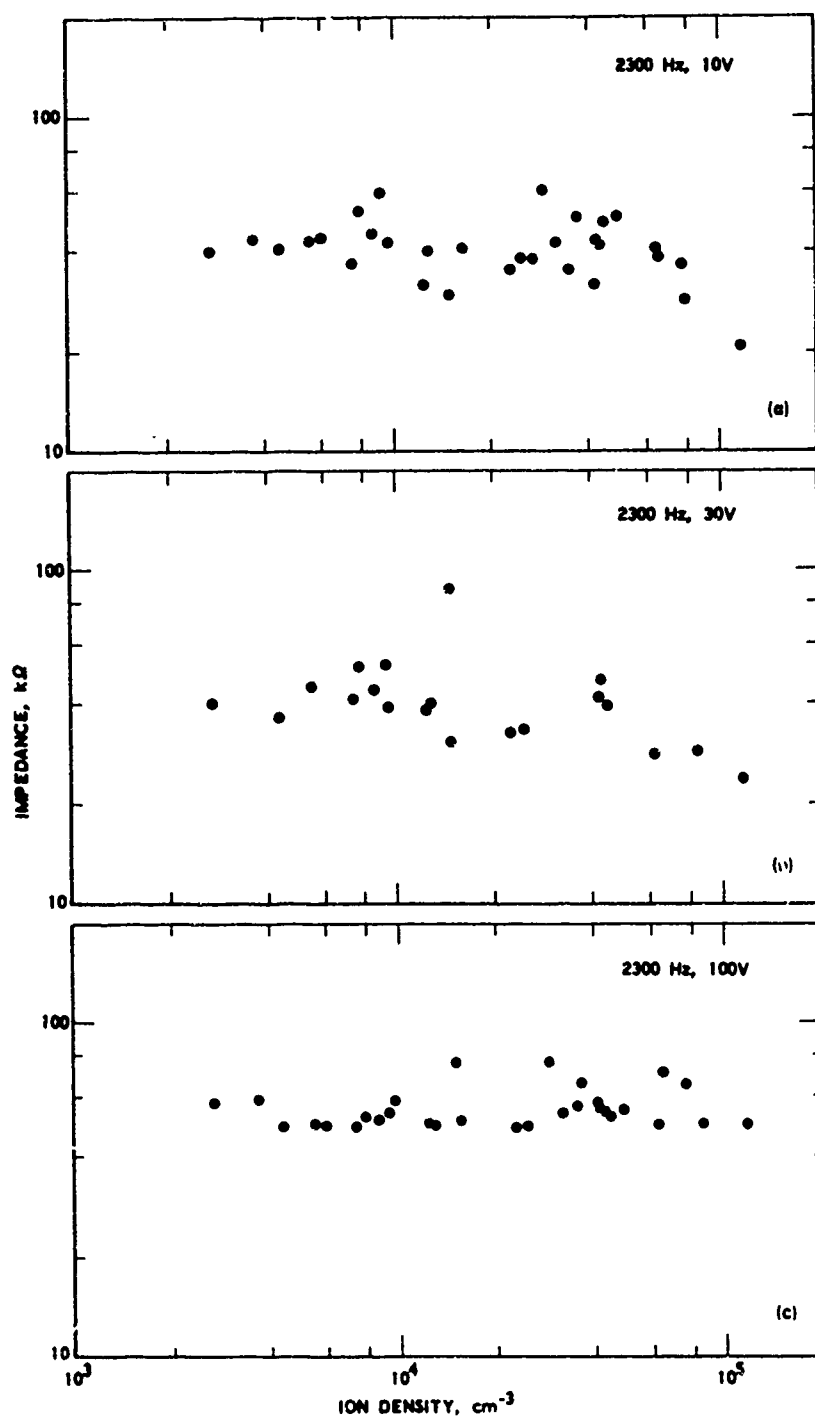
Fig. 41. Primary dipole impedance for 10-, 30-, and 100-V excitation at 2.3 kHz as a function of total ion density.
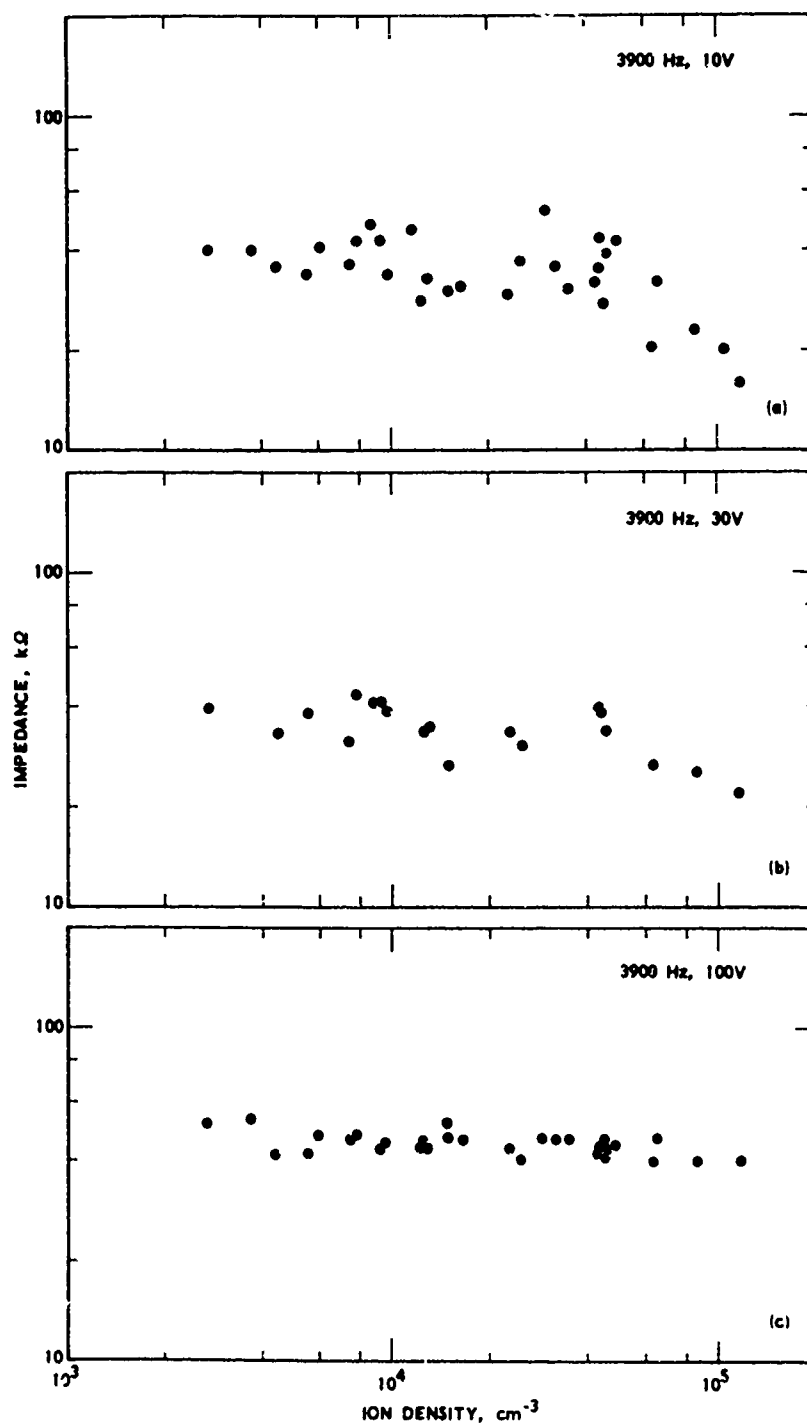
Fig. 42.   Primary dipole impedance for 10-, 30-,
           and 100-V excitation at 3.9 kHz as a
           function of total ion density.
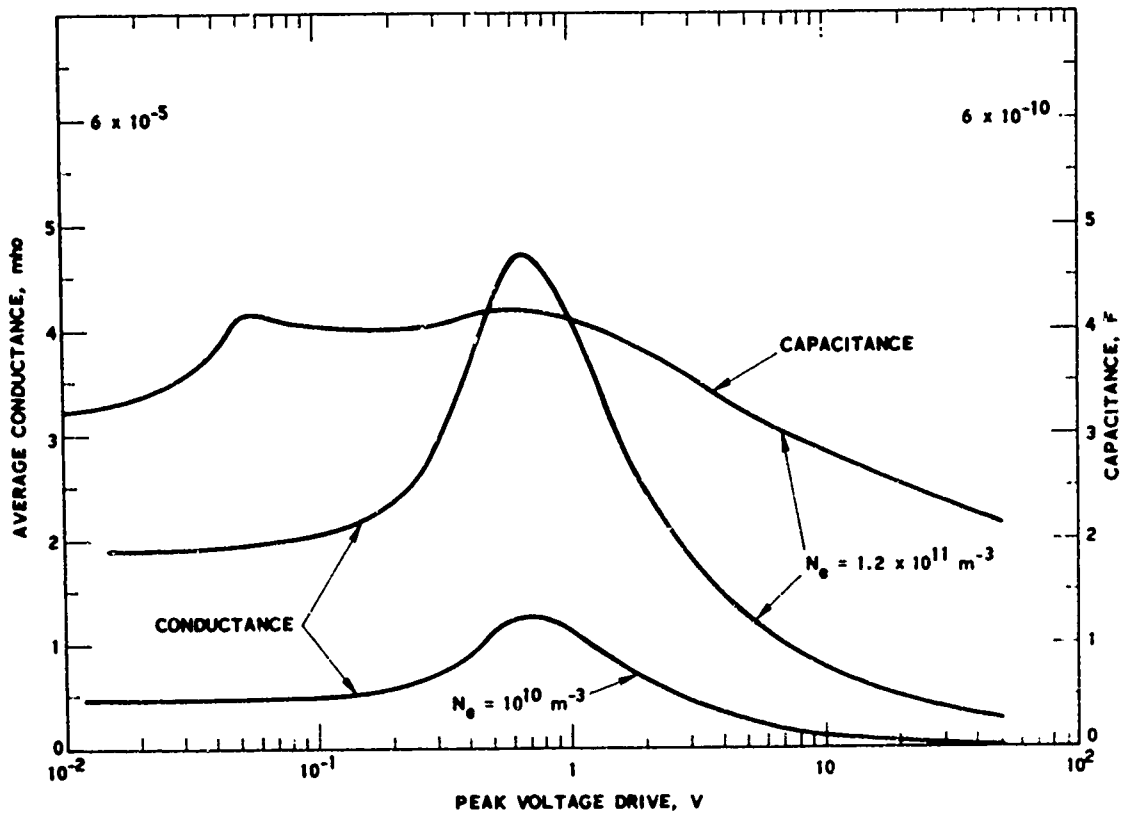
Fig. 43. Sheath conductance and sheath capacitance predicted by nonlinear quasistatic sheath model for electron densities of 1×10^{10} m^{-3} and 1.2×10^{11} m^{-3} (provided by Shkarofsky).

10^3

O 400 Hz
□ 730
△ 1300

10^2

IMPEDANCE, kΩ

10^1

1

0.01   0.1   1.0   10.0   100

EXCITATION VOLTAGE, V p-p
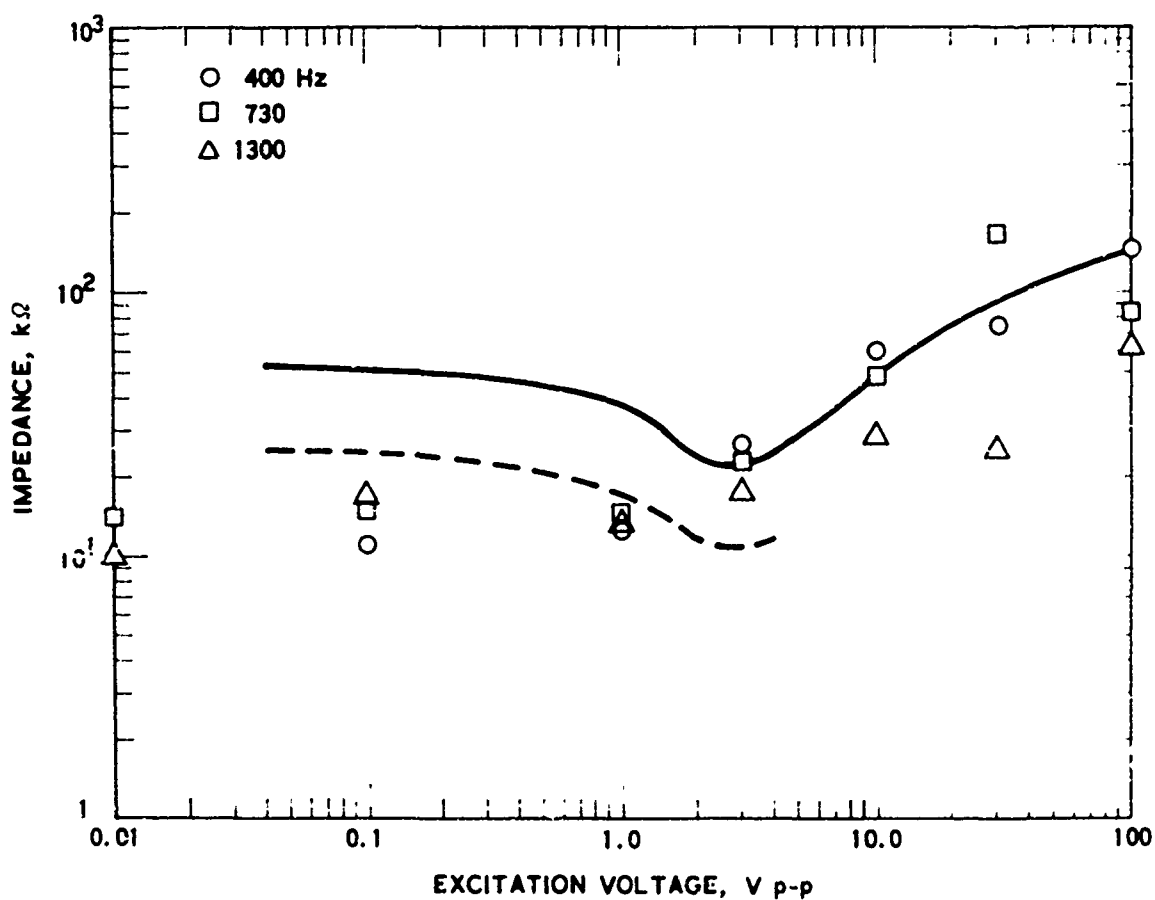
Fig. 44. Comparison of measurements of primary dipole impedance with prediction of nonlinear quasistatic sheath model. (Data acquired at 02:52 UT on 11 August 1971. Satellite position – alt: 817 km, INVL: 29.1°, B: 0.257 g. Ion density: $1.2 \times 10^5 cm^{-3}$.)

Table VII. Input Parameters for Shkarofsky's Nonlinear Sheath Calculations

Case	1	2
Antenna radius (m)	0.00635	0.00635
Antenna half length (m)	16.0	16.0
Separation of feed points (m)	0.75	0.75
$\bar{v} \times \bar{B} \cdot \bar{l}$ voltage (V)	0.4	0.4
Altitude (km)	815	815
Electron Density (m^{-3})	1.2×10^{11}	1.0×10^{10}
H$^+$/e concentration	0.1	0.1
He$^+$/e concentration	0	0
C^+/e concentration	0.9	0.9
Magnetic field, B (Tesla)	2.47×10^{-5}	2.47×10^{-5}
Electron temp (°K)	1300	1300
Ion temp (°K)	1300	1300
$\sin\alpha_{ram}$	0.68	0.68
$\sin\alpha_{sun}$	0.95	0.95
$\bar{v} \times \bar{B} \cdot \bar{l}/vBl$	0.13	0.13

The discrepancy at low voltages in the linear impedance regime is in part due to the use of an incorrect electron temperature for the computer calculations. The value of 1300°K was provided to Shkarofsky before the planar ion trap measurements of ion temperature were available. The measured temperature is 2900°K. This will decrease the magnitude of the theoretical impedance by a factor of 2.2 at low voltages (to the dashed line in Fig. 44).

d.   Phase

At low drive voltages, the current and voltage are approximately in phase at the higher ion densities as shown in Fig. 45. At low densities the current lags the voltage as expected. As the drive voltage increases, the current advances with respect to the voltage waveform at all frequencies. The phase angle as a function of excitation voltage for the seven frequencies is shown in Fig. 46. The phases are normalized to the 100-V p-p data obtained during the calibrate mode. At that voltage step, a 1-kΩ resistor is inserted in parallel with the antenna. Since this resistance is much less than the sheath impedance at 100 V p-p, the phase angle is essentially zero for that step. The phase angle from the calibrate data is also shown in Fig. 46.

The phase angle for the six largest voltage steps are shown as a function of frequency in Fig. 47. In Figs. 46 and 47, the data plotted with open symbols do not follow the general trend of the majority of the data. Since the reason for each discrepancy is not understood, they are not connected to the other data points.

It is apparent from Figs. 46 and 47 that the phase advances with increasing voltage drive and increasing frequency. This phase advance implies an inductive reactance in the circuit. Such a result is contrary to existing nonlinear sheath models which predict an increasing capacative reactance as frequency and voltage increase (Refs. 10, 14).

This discrepancy is most likely due to the breakdown in the quasi-static analysis used by these investigators. The basic assumption that under lies their calculations is stated by Shkarofsky (Ref. 10)"... that the VLF applied voltage can be considered as a dc effect for each instant during its oscillation." When this is not the case, the transit time of ions across the sheath must be taken into account. Bunching and debunching of the ions as they cross the sheath is the most likely explanator for the observed inductive phase shifts.

B.   HARMONIC CONTENT

An example of the voltage and current waveforms at 1.3 kHz for each voltage step is shown in Fig. 48. The voltage is shown at the top of
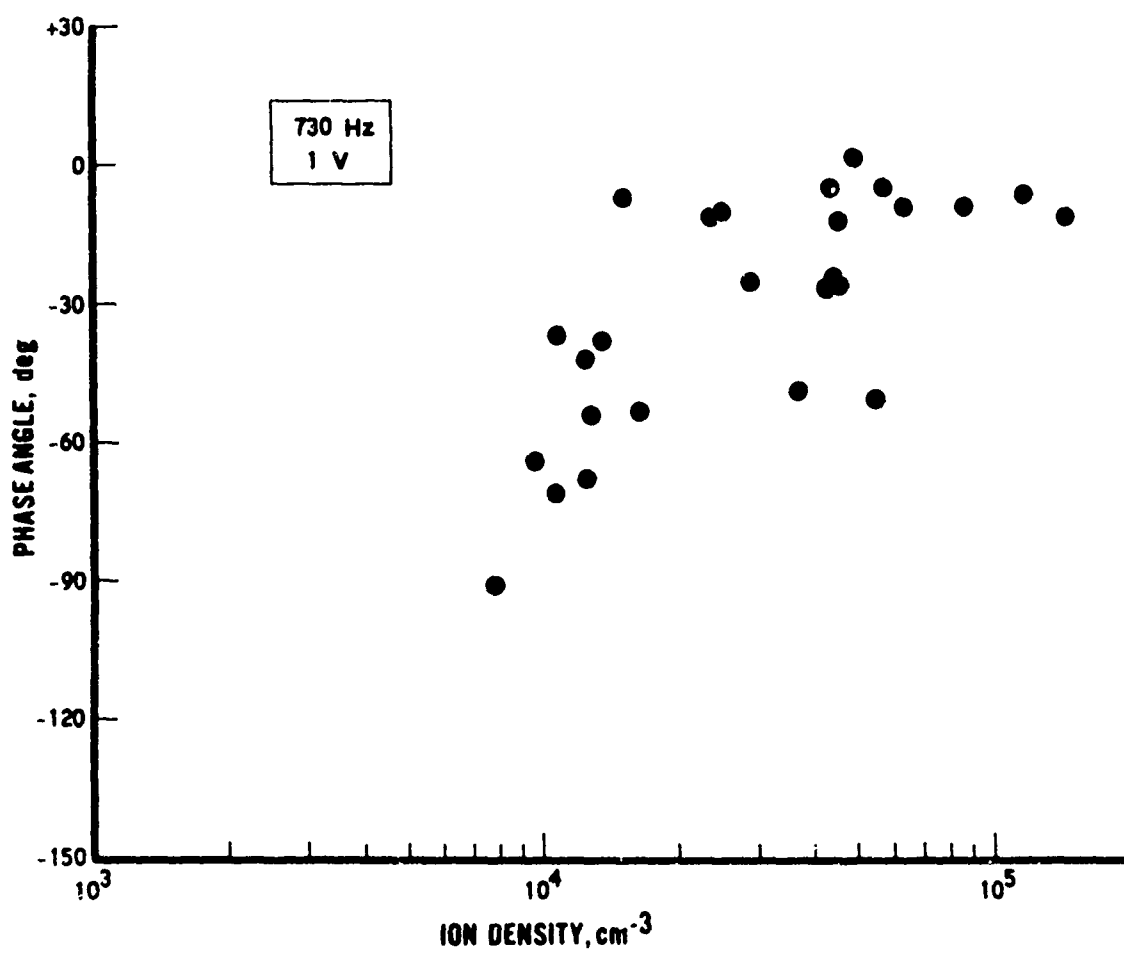
Fig. 45.   Phase angle of current waveform with respect to voltage waveform
as a function of ion density for 1-V excitation at 730 Hz.
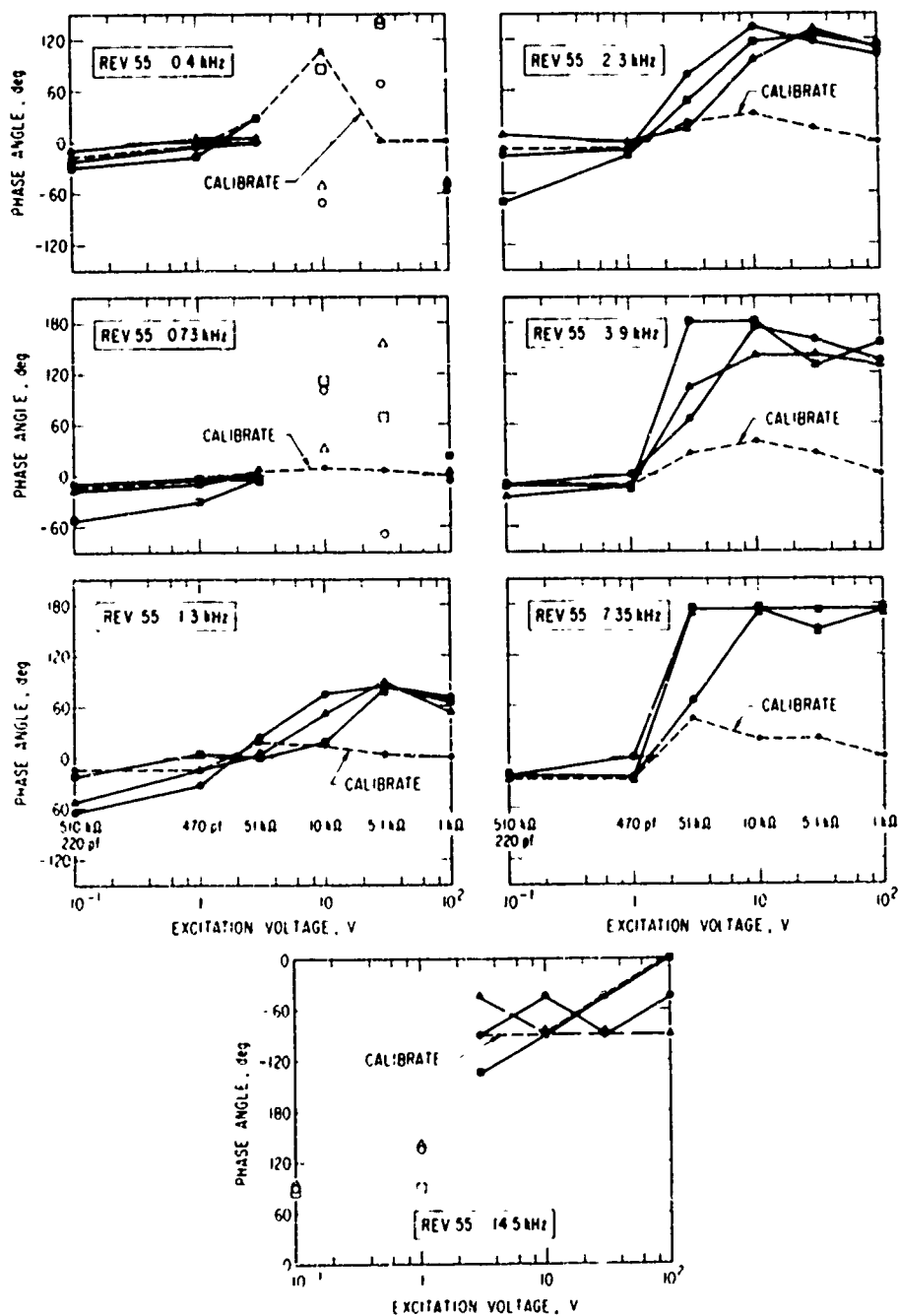
Fig. 46. Phase angle plotted vs peak excitation voltage for
four data blocks during Rev. 55. (The data
obtained in the calibrate mode is connected by
a dashed line. Satellite position same as for
Fig. 22.)
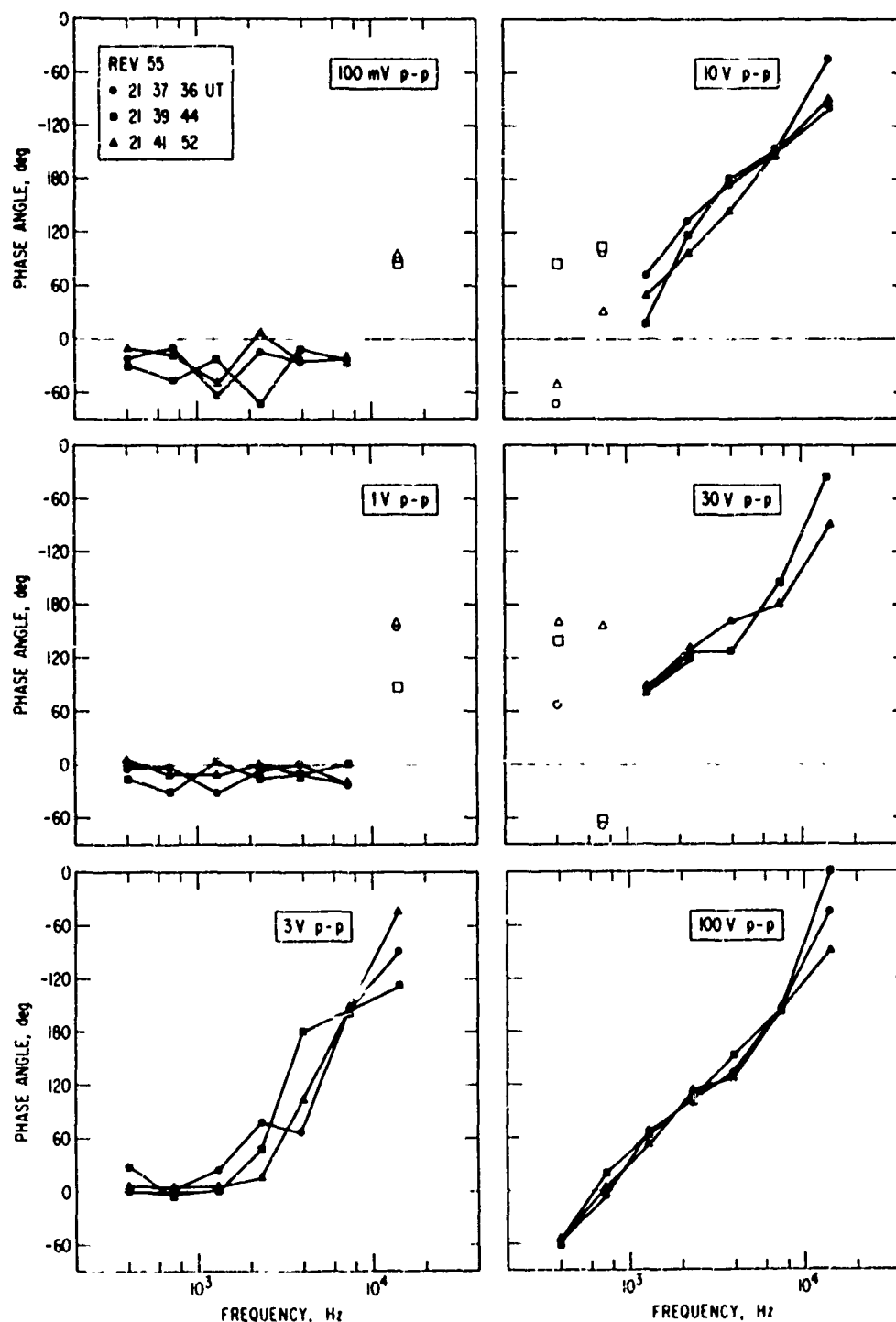
Fig. 47. Phase angle plotted vs excitation frequency for
          three data blocks during Rev. 44. (Same satellite
          position as for Fig. 22.)

REV 58.4   1.3 kHz
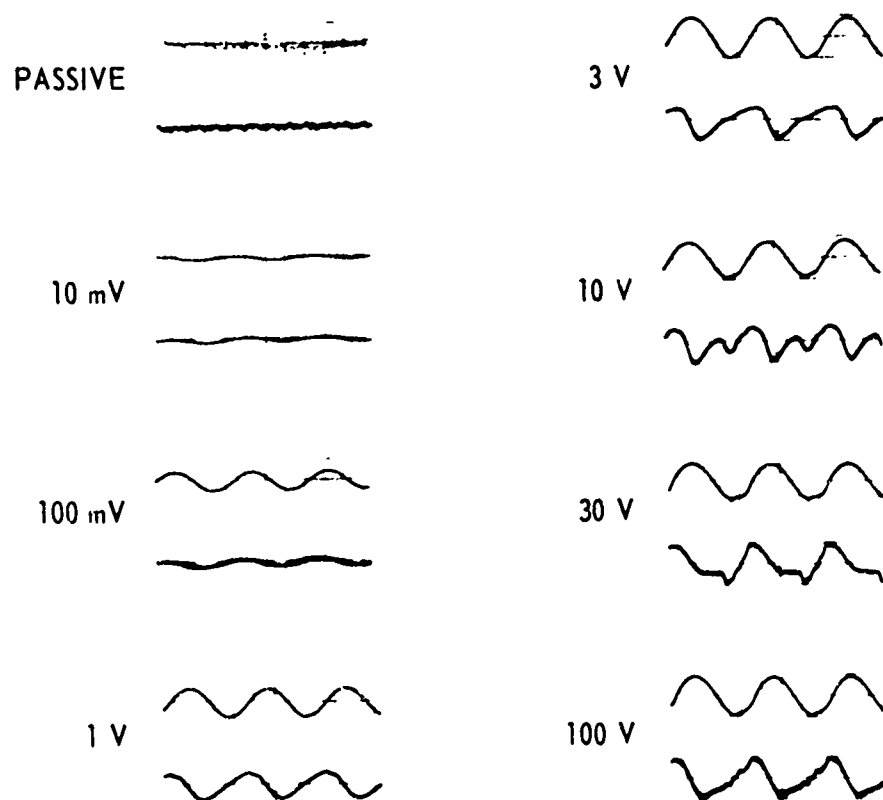
Fig. 48.   Voltage (top) and current (bottom) waveforms
for the seven excitation voltages at 1.3 kHz.
(Data from the electric receiver (top) and
magnetic r∩ceiver (bottom) is displayed dur-
ing the passive time period.   Data acquired
at 02:52 UT on 11 August 1971.   Satellite
position – alt: 815 km, INVL: 27.7°, B: 0.252 g,
LT: 15:42.)

each frame, the current at the bottom. The voltage waveforms remain sinusoidal at all excitation levels. The current waveforms are sinusoidal at the lowest three voltage levels. At higher voltage levels, the current waveforms are distorted with the harmonic content occasionally exceeding the power at the fundamental frequency.

The harmonic content in the voltage, current and field-intensity waveforms can be qualitatively determined by RAYSPAN spectral analysis of the analog data. Sample RAYSPAN spectrograms for an excitation frequency of 1.3 kHz are shown in Fig. 49. Generally the harmonic content of the **electric-probe signal is similar to that of the excitation voltage,** whereas the harmonic content of the magnetic-probe signal is similar to that of the dipole current.

A consistent feature of the data is a decrease in the harmonic power content at the higher voltage levels. The maximum harmonic power relative to the fundamental occurs at 10 V or 30 V peak-to-peak. The power spectral density in arbitrary units is shown plotted vs frequency in Fig. 50 for excitation at 10 and 100 V peak-to-peak at 2.3 kHz. At 10 V, the power at the first harmonic is -10.8 dB below the fundamental while at 100 V, the power at the first harmonic is -18.3 dB below the fundamental.

C.   RECEIVED FIELDS

Electric potentials at the seven excitation frequencies were measured by the dual electric probe antennas. One antenna measured potentials $V_{||}$ parallel to the axis of the primary dipole antenna. The other measured potentials $V_{\perp}$ perpendicular to that axis. Magnetic field intensities were measured by a ferrite-core, coil antenna. The geometry is shown in Fig. 2.

The impedance of the dual-probe antenna is measured during the 0.1-V p-p excitation step at each frequency. These data are used to validate the linear impedance model that is used to determine the electric field intensities from the measured potentials.

1.3 kHz

PRIMARY DIPOLE VOLTAGE

PRIMARY DIPOLE CURRENT

MAGNETIC ANTENNA

EI ANTENNA

EXCITATION VOLTAGE, V
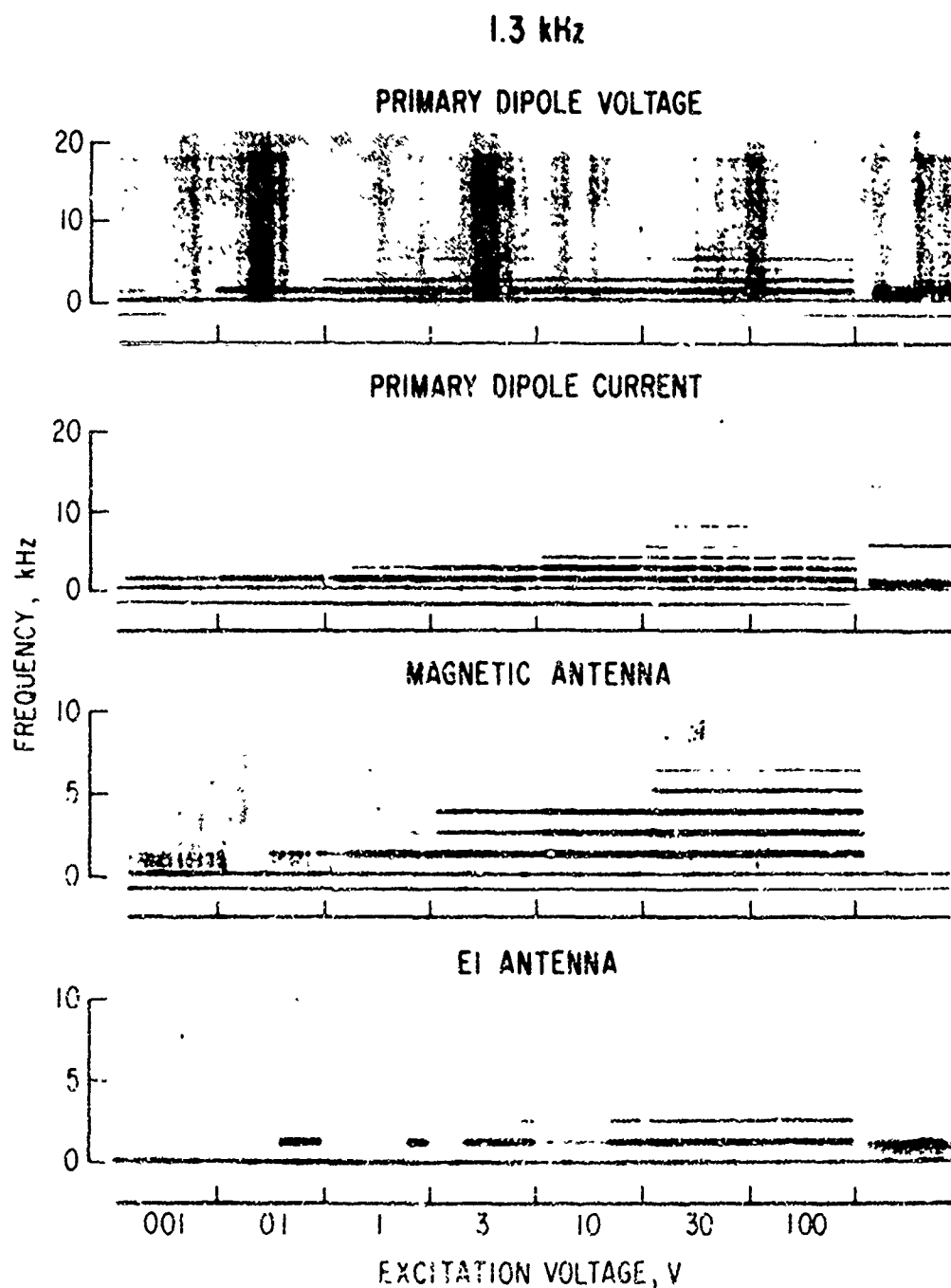
Fig. 49. Rayspan spectrograms of the antenna excitation
and received signals for excitation at 1.3 kHz.
(Data acquired at 02.52 UT on 11 August 1971.
Satellite position – alt 815 km, INVL: 27.7°.
B: 0.252 g, LT: 15:42.)

-81-
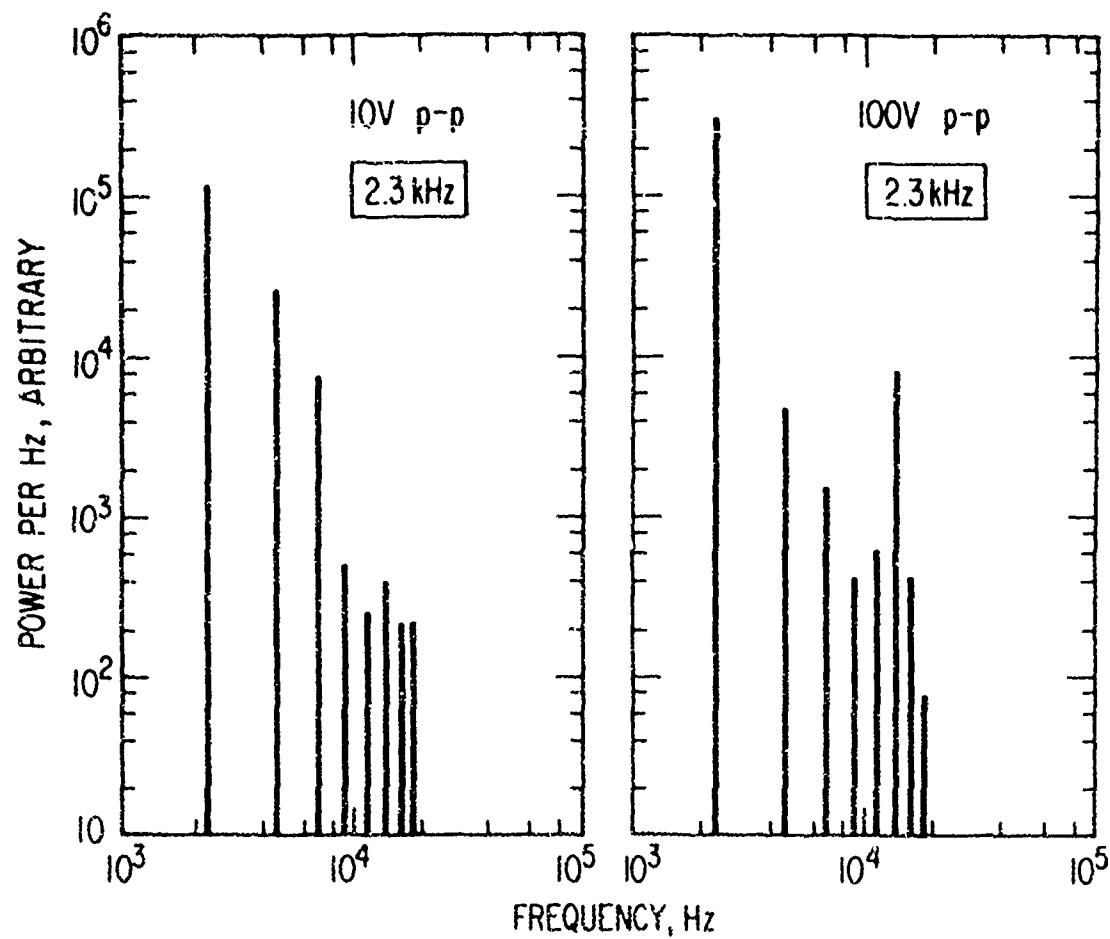
Fig. 50. Power spectral density plots for 10- and 100-V
excitation at 2.3 kHz. (Data acquired at 02:53 UT
on 11 August 1971. Satellite position – alt: 813 km,
INVL: 26.2°, B: 0.248 g, LT: 15:42.)

1. ELECTRIC ANTENNA IMPEDANCE

The model of the circuit used to measure the impedance of the dual-sphere electric antenna is shown in Fig. 51. The equations governing the behavior of the sheath are essentially those used to describe the linear sheath of the primary dipole antenna. Equation (22) must be modified to spherical geometry, i.e.,

$$C_{sh} = \frac{4\pi \epsilon_o \, r \, r_{sh}}{r_{sh} - r} \tag{29}$$

The magnitude of the antenna impedance is

$$Z_m = |2Z_a \, Z_{sh}/(Z_a + Z_{sh})| \tag{30}$$

and the ratio of the voltage φ_{in} at the input to the preamplifier to the source voltage φ_s between the spheres is

$$\frac{\varphi_{in}}{\varphi_s} = \left| \frac{Z_a}{Z_a + 2Z_{sh}} \right| \tag{31}$$

The circuit parameters are listed in Table VIII.

The ratio φ_{in}/φ_s computed from Eq. (31) for $T_- = 2200°\mathrm{K}$ is plotted as a function of electron density in Fig. 52. At low densities, the impedance of the antenna capacitance C_a dominated the circuit. An example of such low density data is shown in Fig. 53. The measured impedance is fitted by the line which corresponds to an impedance of $1/\omega \, C_a$.

At higher densities, the sheath resistance begins to dominate the impedance at the lower frequencies. It is only at these higher densities that the model can be quantitatively validated. An example of such data obtained at higher densities during Rev. 242 is shown in Fig. 54.
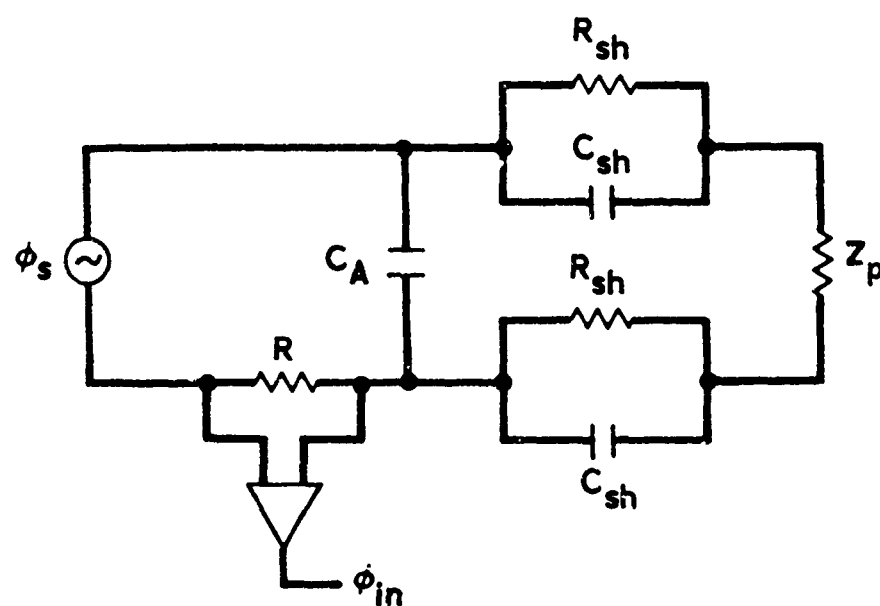
Fig. 51.   Equivalent circuit for the linear sheath model of
the dual-sphere electric antenna.
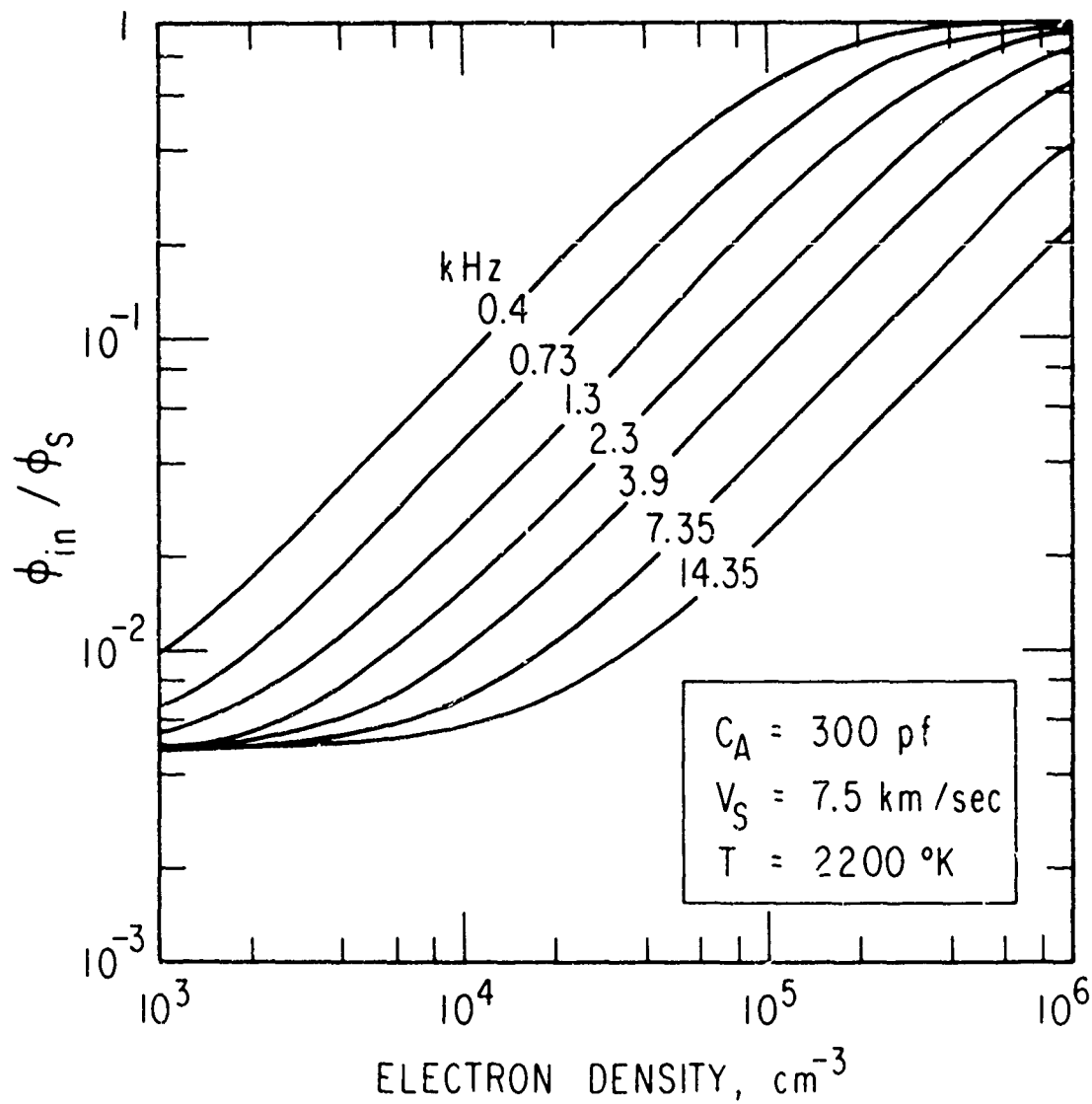
Fig. 52.   Electron density dependence of ϕ_{in}/ϕ_s for the dual-sphere
electric antenna for an electron temperature of 2200°K.
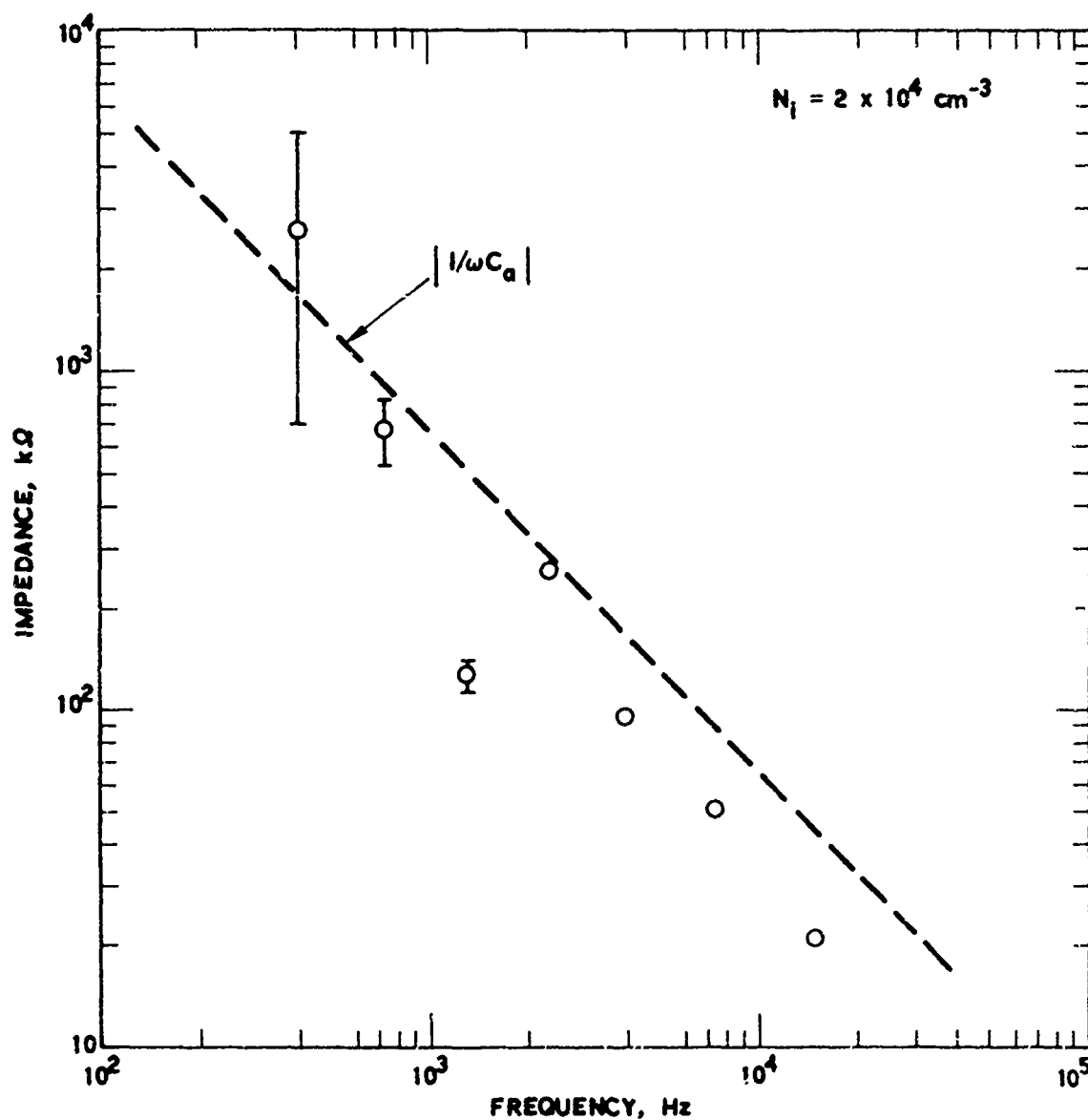
Fig. 53. Impedance of the dual-sphere electric antenna when $N_i = 2 \times 10^4$ cm^{-3}. The line represents $|Z_m| = 1/\omega C_a$. (Data acquired at 18:52 UT on 13 August 1971. Satellite position – alt: 918 km, INVL: 23.6°, B: 0.272 g, LT: 03:36.)
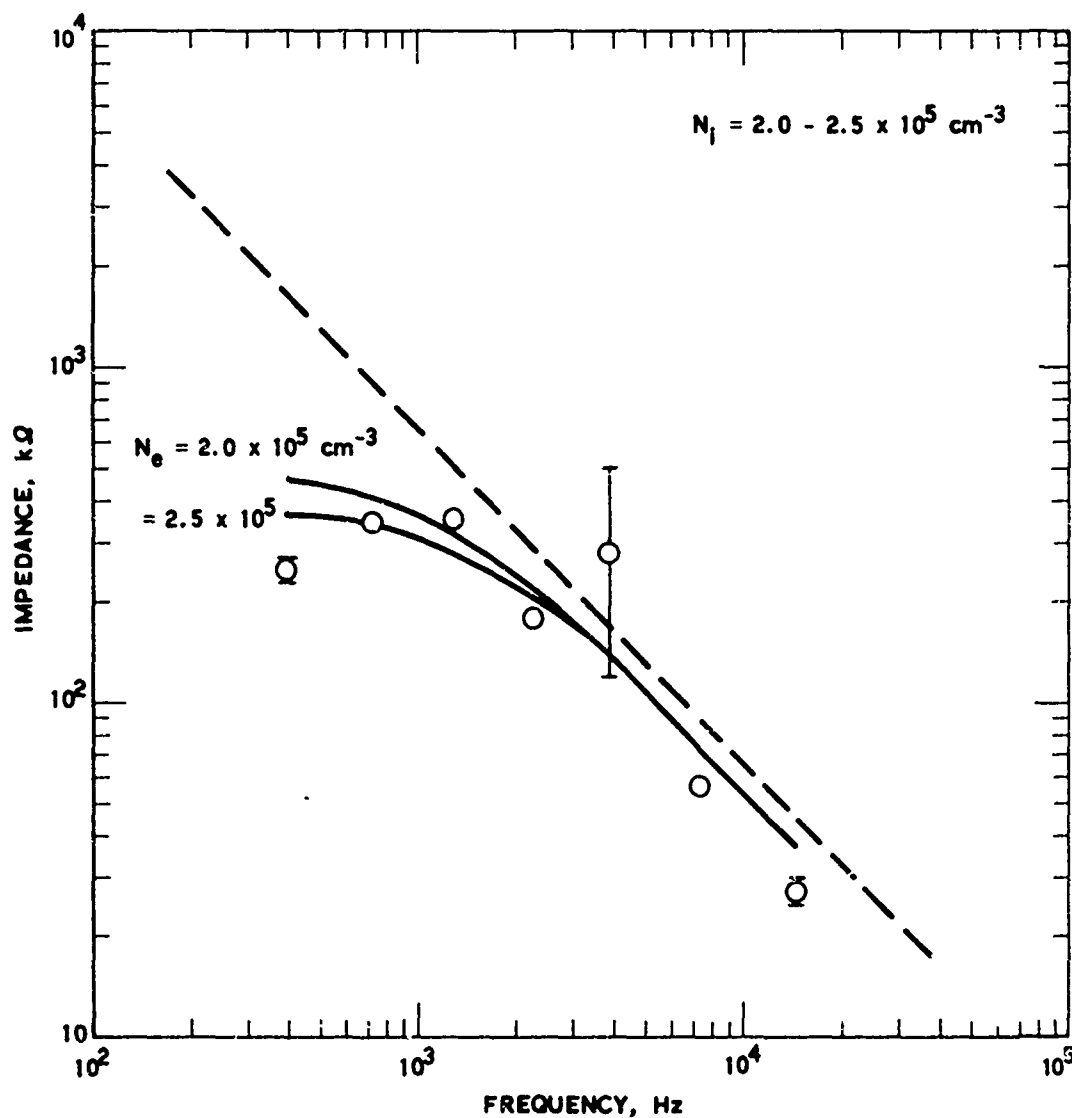
Fig. 54. Impedance of the dual-sphere electric antenna when N_i = 2.0 - 2.5 × 10⁵ cm⁻³. (The line represents $|Z_m|$ = 1/ωCₐ and the curves are calculated using Eq. (30) for N_e = 2.0 × 10⁵ cm⁻³. Data acquired at 03:51 UT on 24 August 1971. Satellite position − alt: 789 km, INVL: 17.5°, B: 0.243 g, LT: 14:42.)

Table VIII. Electric Antenna Parameters

Symbol	Parameter	Value
r	Antenna Radius	0.0254 m
A_+	πr^2	0.002 m^2
v_S	Satellite Velocity	7.5 km/sec
C_a	Capacitance	300 pf

The reduction in Z_m at the lower frequencies is apparent. The theoretical curves for Z_m, calculated using Eq. (30) with $N = 2 \times 10^{11}$ and 2.5×10^{11} m^{-3} are drawn for comparison with the measured values.

The electric field intensities are obtained from the electric potentials measured by the dual-probe electric antennas by dividing the measured potential by $0.8 \times \varphi_{in}/\varphi_s$. The factor 0.8 is the probe separation in meters. Hence

$$E_{||} = V_{||}/(0.8 \times \varphi_{in}/\varphi_s) \tag{32}$$

where φ_{in}/φ_s is obtained from Fig. 52 which can be scaled for other electron temperatures.

2.   ELECTRIC FIELDS

In the normal operating mode, the rms magnetic-field intensities and the rms electric potentials parallel to the primary dipole were measured by the narrowband receivers twice per second.

An example of typical $V_{||}$ potentials measured during a higher density day time pass is shown in Fig. 55. The data are averages of four samples obtained at a rate of two samples per second. At any given excitation level, there is spread in measured potentials of somewhat less than an order of magnitude.
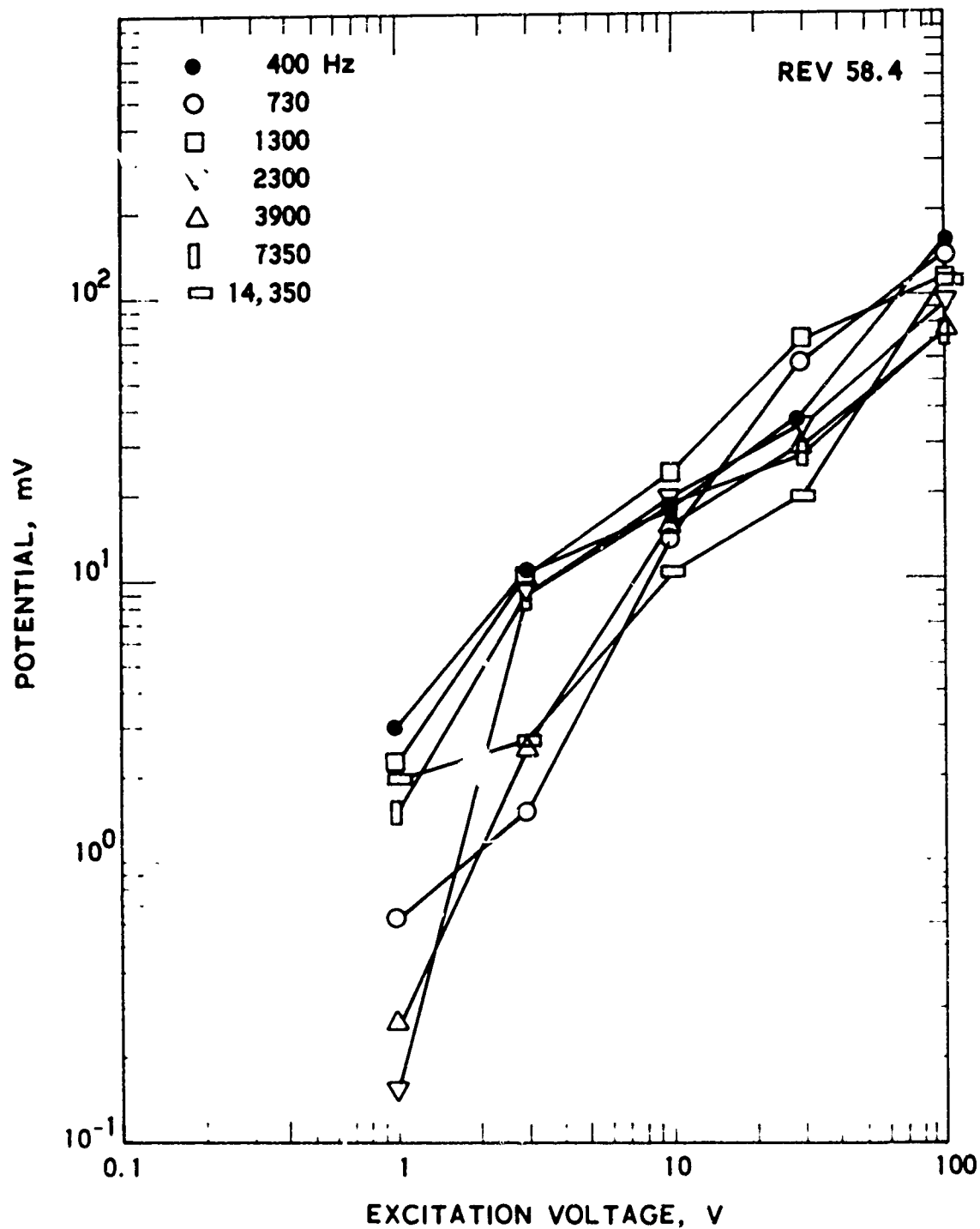
Fig. 55. Electric potentials plotted as a function of the primary dipole antenna excitation voltage. (Data acquired at 02:50 UT on 11 August 1971. Satellite position – alt: 825 km, INVL: 34.5°, B: 0.278 g, LT: 15:24.)

-89-

Upon command from the RTS, the data from the dual-sphere probe perpendicular to the axis of the primary dipole antenna replace the magnetic field intensity data in both the broadband and narrowband telemetered data. An example of typical $V_{||}$ and $V_{\perp}$ potentials measured simultaneously in this manner is shown in Fig. 56. In general, the magnitudes of $V_{||}$ and $V_{\perp}$ are comparable at the location of the dual-probe antennas.

a.   Density Dependence

At the highest excitation voltage, the measured $V_{||}$ potentials increase with electron density as shown in Fig. 57. A larger data set exhibits the same behavior for the 30-V p-p drive voltage at 2.3 kHz in Fig. 58.

The potentials shown in Fig. 57 were converted to electric fields using the procedure described previously. The resulting fields are shown in Fig. 59. The increasing potential with density maps into a decreasing field with density. Hence, the increasing potential is primarily due to an increase in φ_{in}/φ_{s}, which outweighs the decreasing electric field intensity as the density increases.

The dependence of the potential and electric field intensity on frequency is illustrated in Fig. 60.

3.   MAGNETIC FIELDS

The sensitivity of the magnetic field receiver was set to measure minimum field intensities of approximately 1 mγ. This is the level expected for naturally occurring ELF/VLF emissions and was chosen in order to monitor these e, sions. With this sensitivity, the range of the instrument was insufficient to measure magnetic fields at the highest primary dipole drive voltages. The magnetic field intensity at which the magnetic measurement saturates is listed in Table IX.

Typical magnetic field intensities measured at the excitation frequency during a block of data are shown in Fig. 61. At the higher frequencies, the magnetic receiver saturates at the 1-V p-p excita ion. At the lower frequencies, the data suggest that the magnetic field intensity increases roughly in proportion to the excitation voltage.
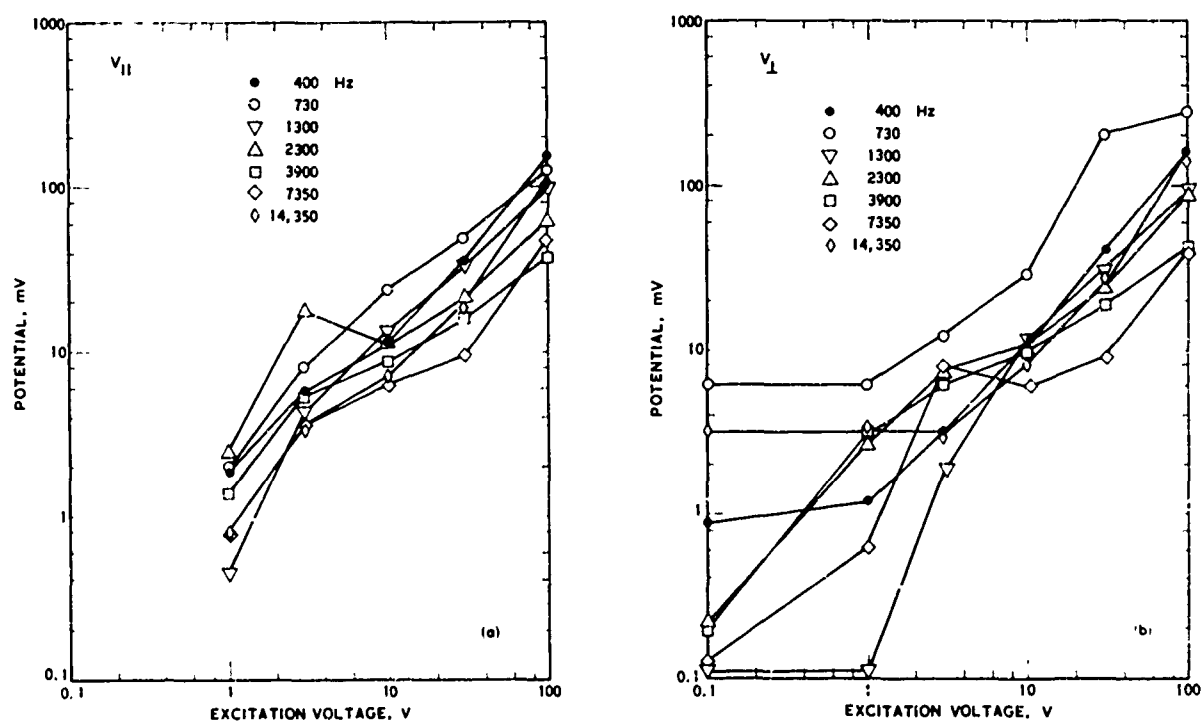
Fig. 56. Electric potentials parallel (a) and perpendicular (b) to the axis of the primary dipole antenna as a function of excitation voltage. (Data acquired at 01:49 UT on 16 August 1971. Satellite position – alt: 822 km, INVL: 43.9°, B: 0.320 g, LT: 15:12.)
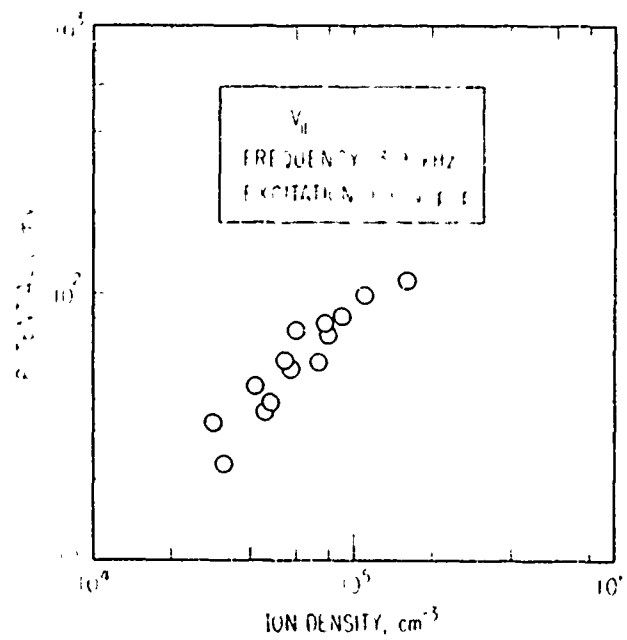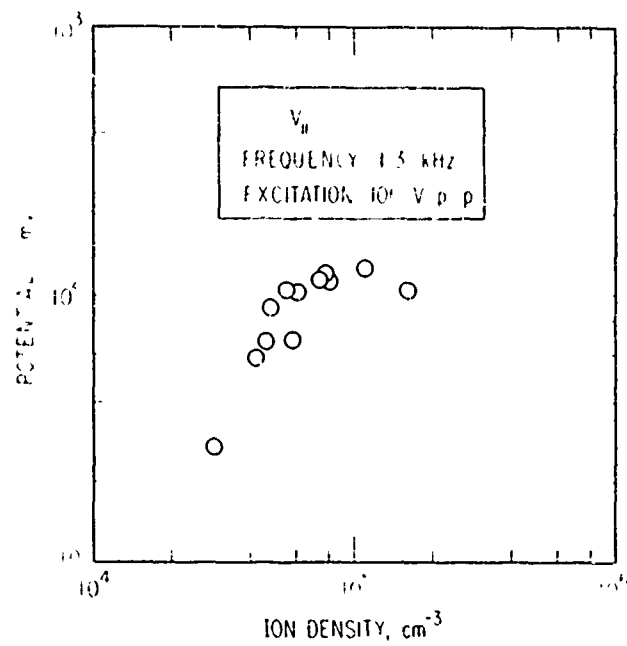
Fig. 57. Electric potentials plotted vs ion density for 100-V excitation at 1.3 and 3.9 kHz.
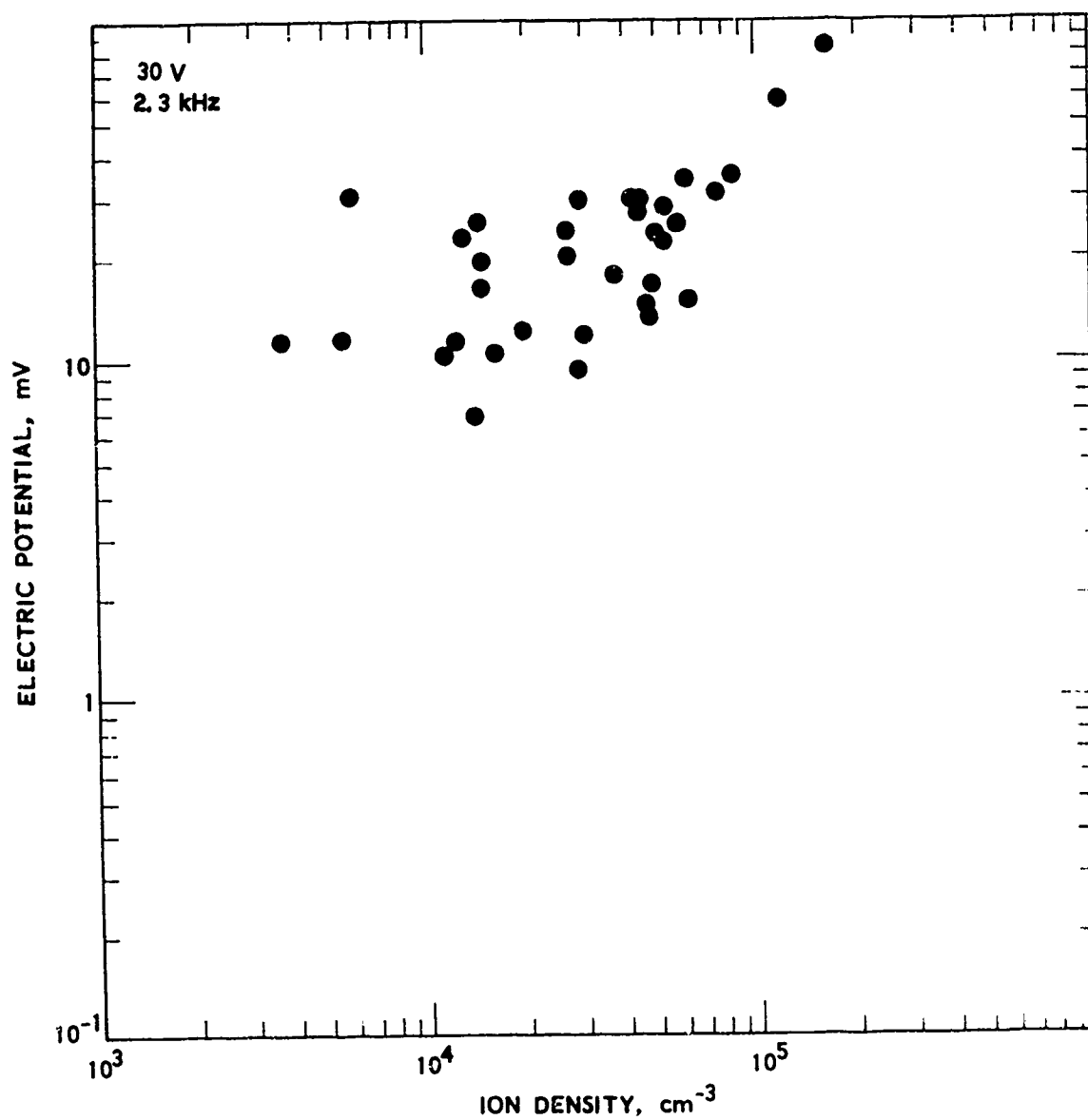
Fig. 58. Electric potentials plotted vs ion density for 30-V excitation at 2.3 kHz.
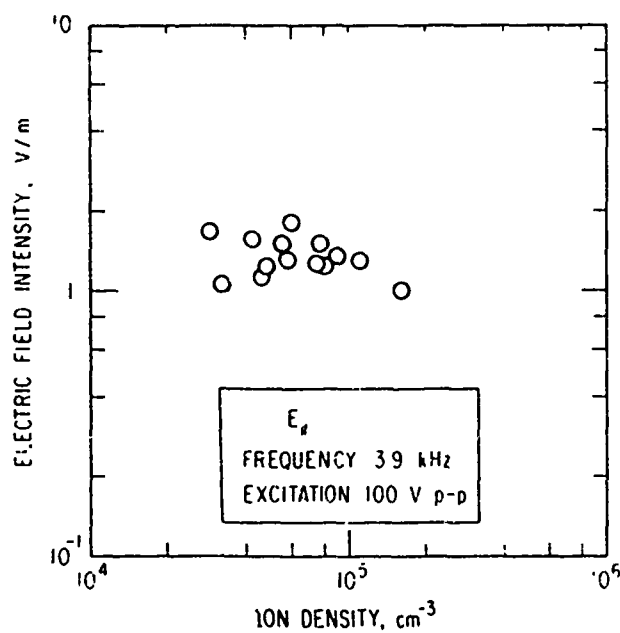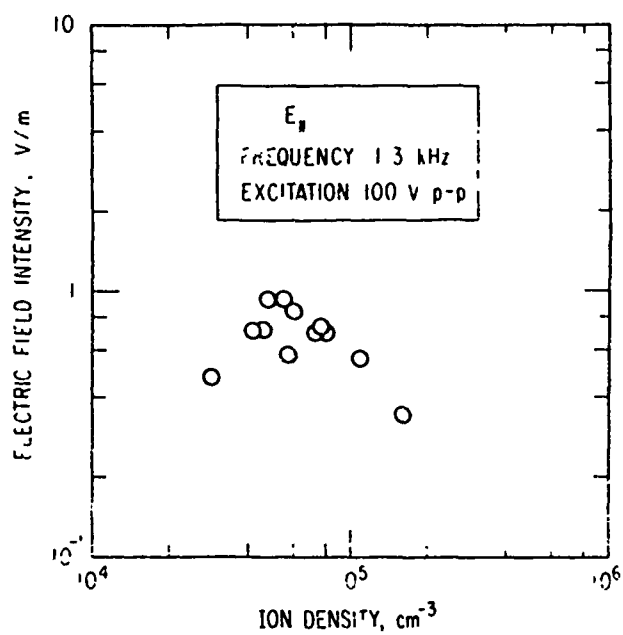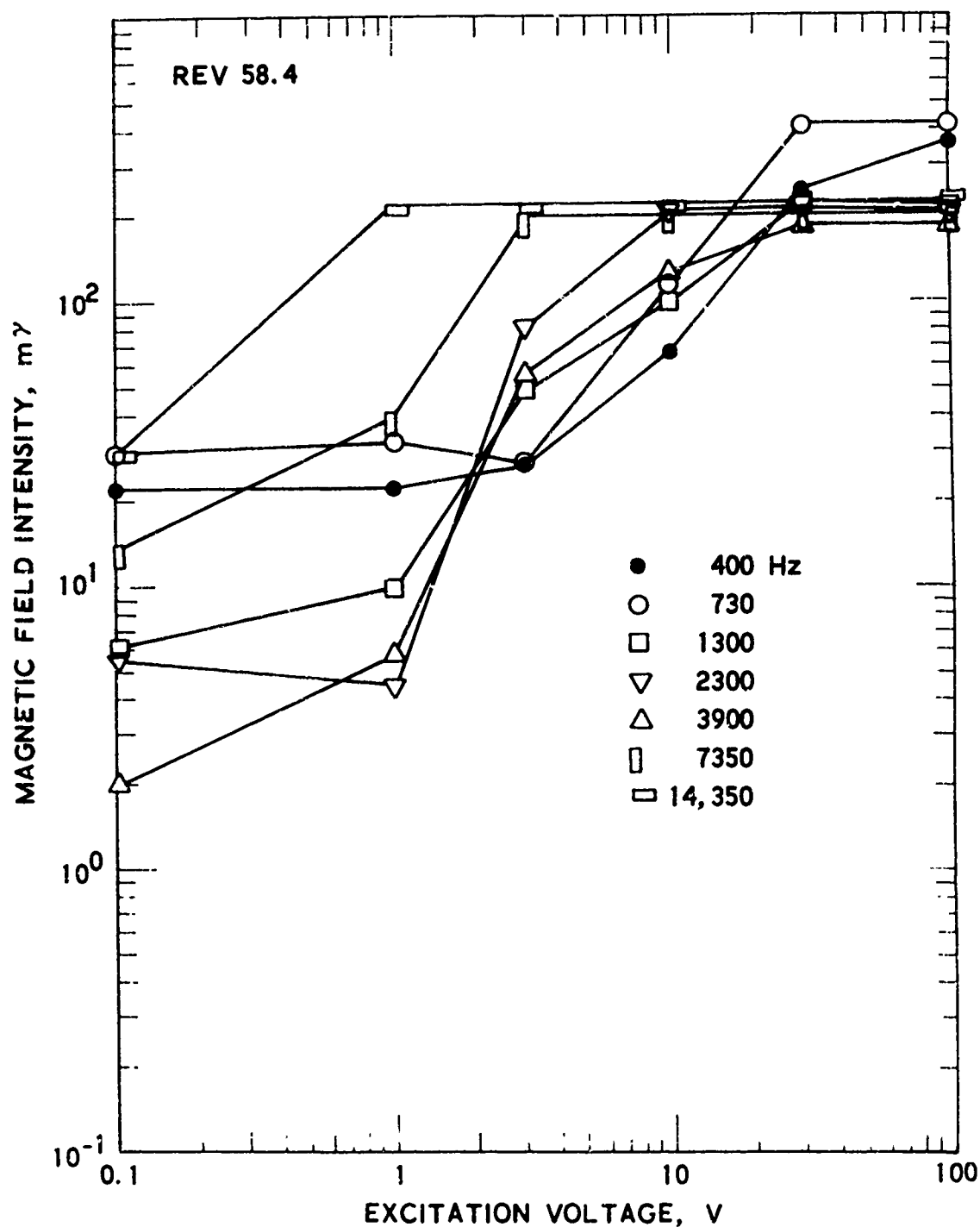
Fig. 59. Electric fields parallel to primary dipole antenna plotted vs density for 100-V excitation at 1.3 and 3.9 kHz.
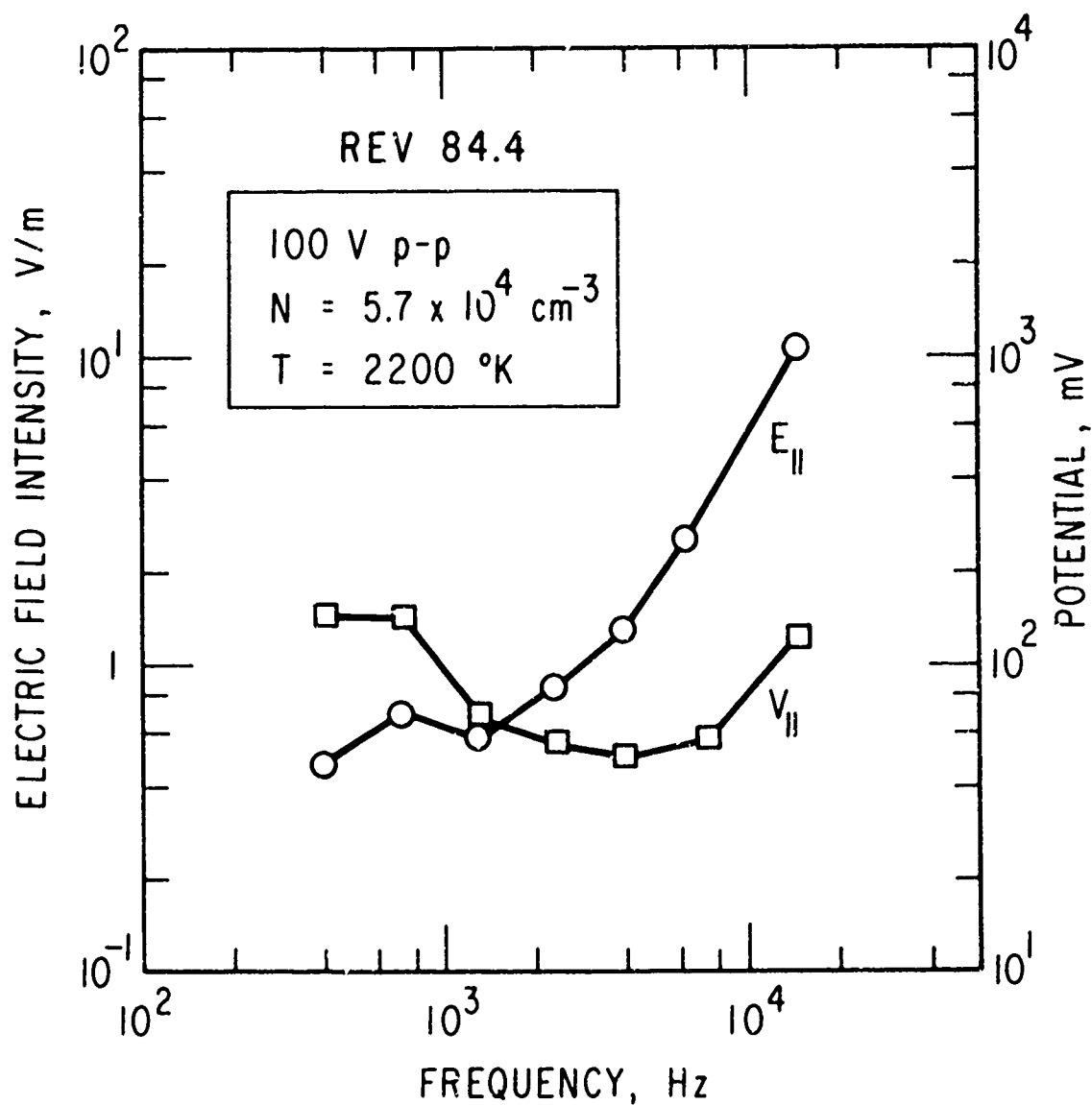
Fig. 60. Frequency dependence of potential and electric field intensity.
(Data acquired at 23:01 UT on 12 August 1971. Satellite position –
alt: 827 km, INVL: 48.6°, B: 0.364 g, LT: 15:24.)

Fig. 61. Magnetic field intensity plotted vs primary dipole
antenna excitation voltage. (Data acquired at
02:50 UT on 11 August 1971. Satellite position –
alt: 825 km, INVL: 34.5°, B: 0.278 g, LT:
15:24.)

Table IX.   Magnetic Receiver Saturation Levels

Frequency (kHz)	Maximum Magnetic Field (mγ)
0.40	356.3
0.73	414.2
1.30	219.5
2.30	209.2
3.90	185.0
7.35	202.0
14.35	214.0

4.   ASPECT DEPENDENCE

When plotted as a function of Universal Time, the received potentials at the higher voltage drives vary slowly over a single acquisition which may include four or five blocks, i.e., measurements, at a given frequency and excitation voltage.   However, at lower excitation voltages the measured potentials change by more than an order of magnitude in an apparently erratic manner.   Examples of electric field intensities derived from such data are shown in Figs. 62 and 63.

When these data are replotted as a function of the angle $(\overline{V}, \overline{X})$ between the propulsion module axis and the satellite velocity vector, the data becomes ordered as shown in Figs. 64 and 65.   When this angle is 180°, the primary dipole antenna is in ram with the plasma flowing from the primary dipole toward the receiving antennas.   When this angle is 90°, the plasma is flowing parallel to the axis of the primary dipole antenna.   When this angle is 0°, the plasma is flowing from the primary dipole away from the receiving antenna.

We hypothesize that the signal detected by the receiver at the lower drive voltages is caused by a damped ion acoustic wave propagating from the primary dipole to the receiving antennas.   If the wave phase velocity is
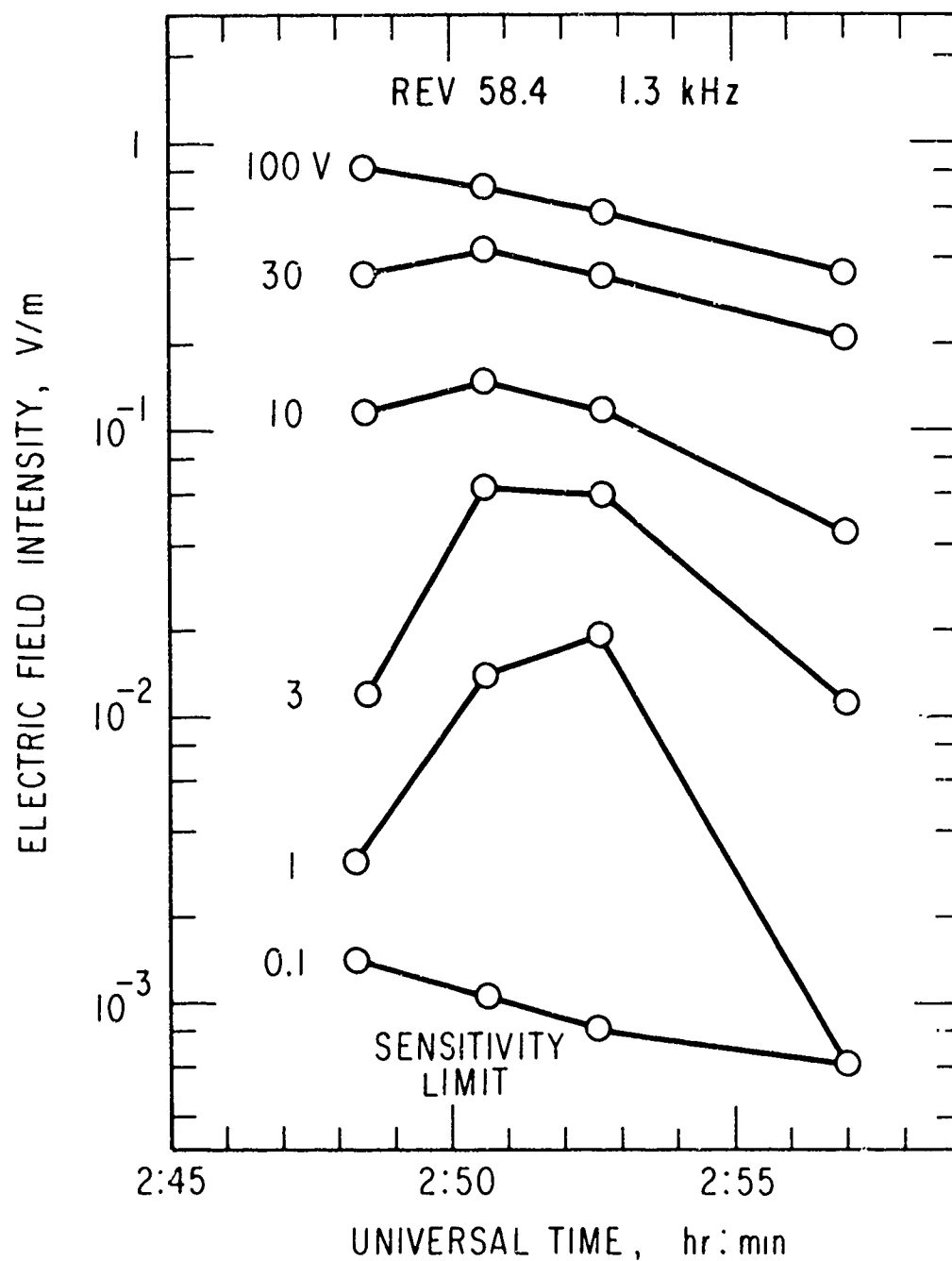
Fig. 62. Electric Field Intensity vs time for excitation at 1.3 kHz.
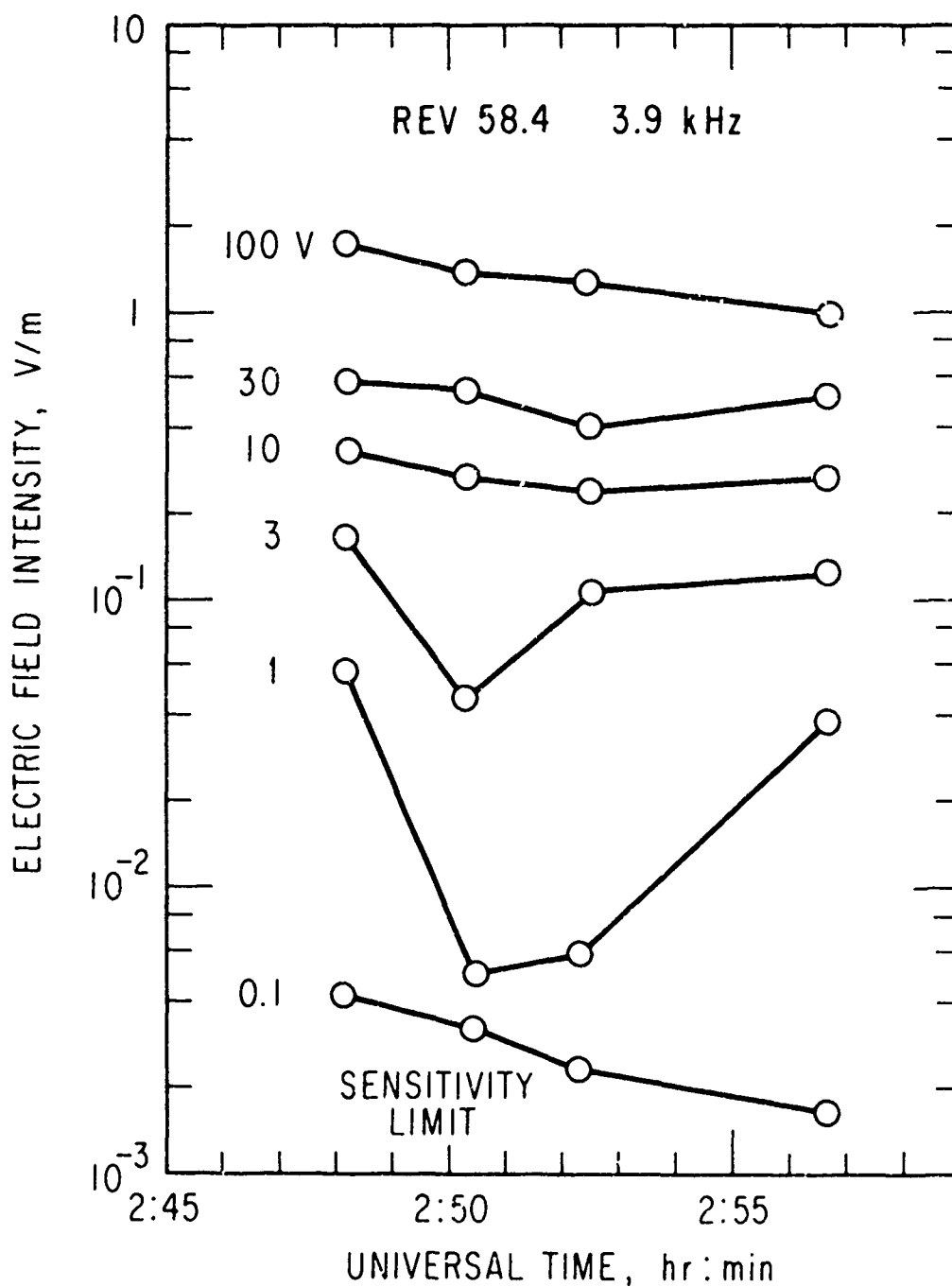
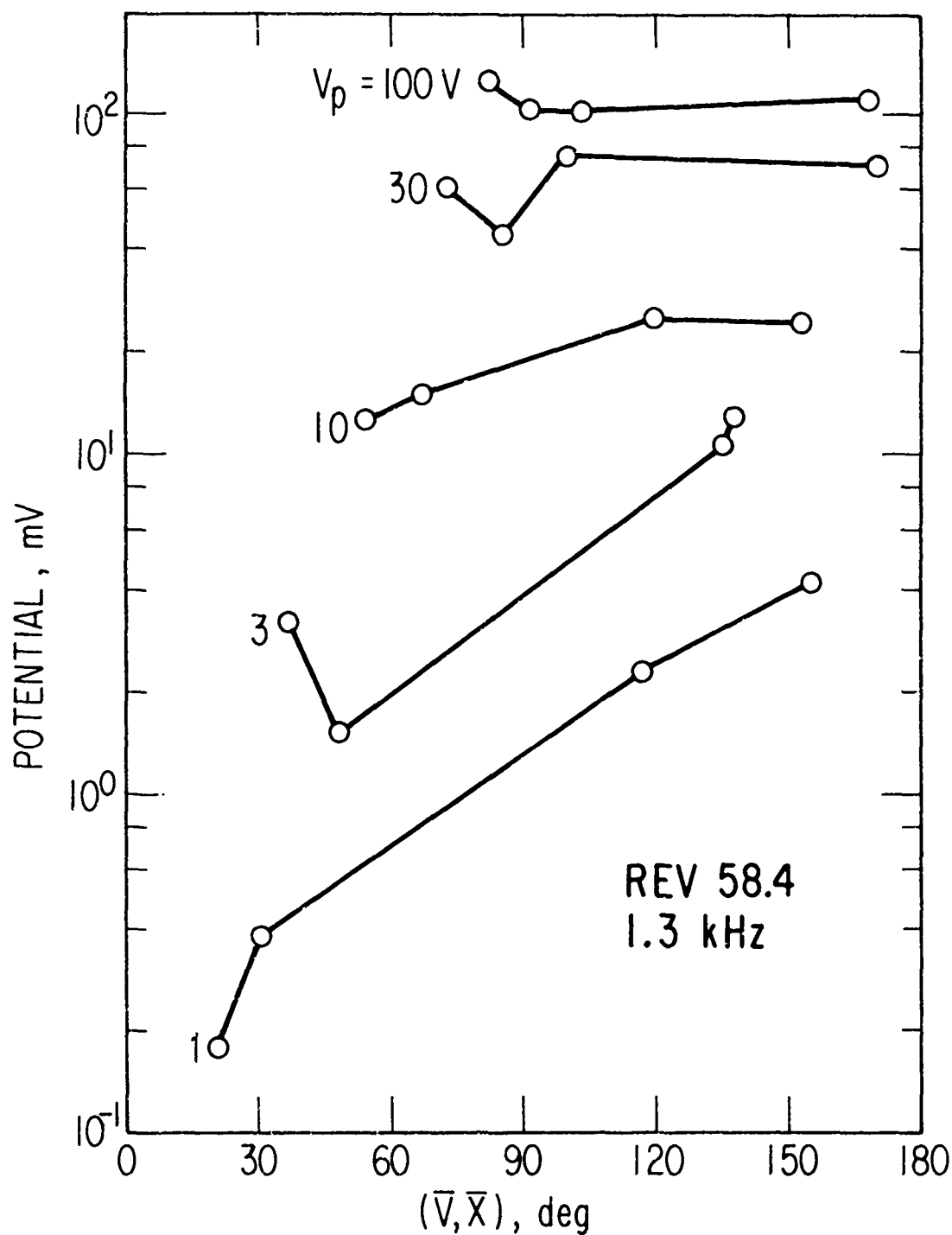Fig. 63. Electric Field Intensity vs time for excitation at 2.3 kHz.

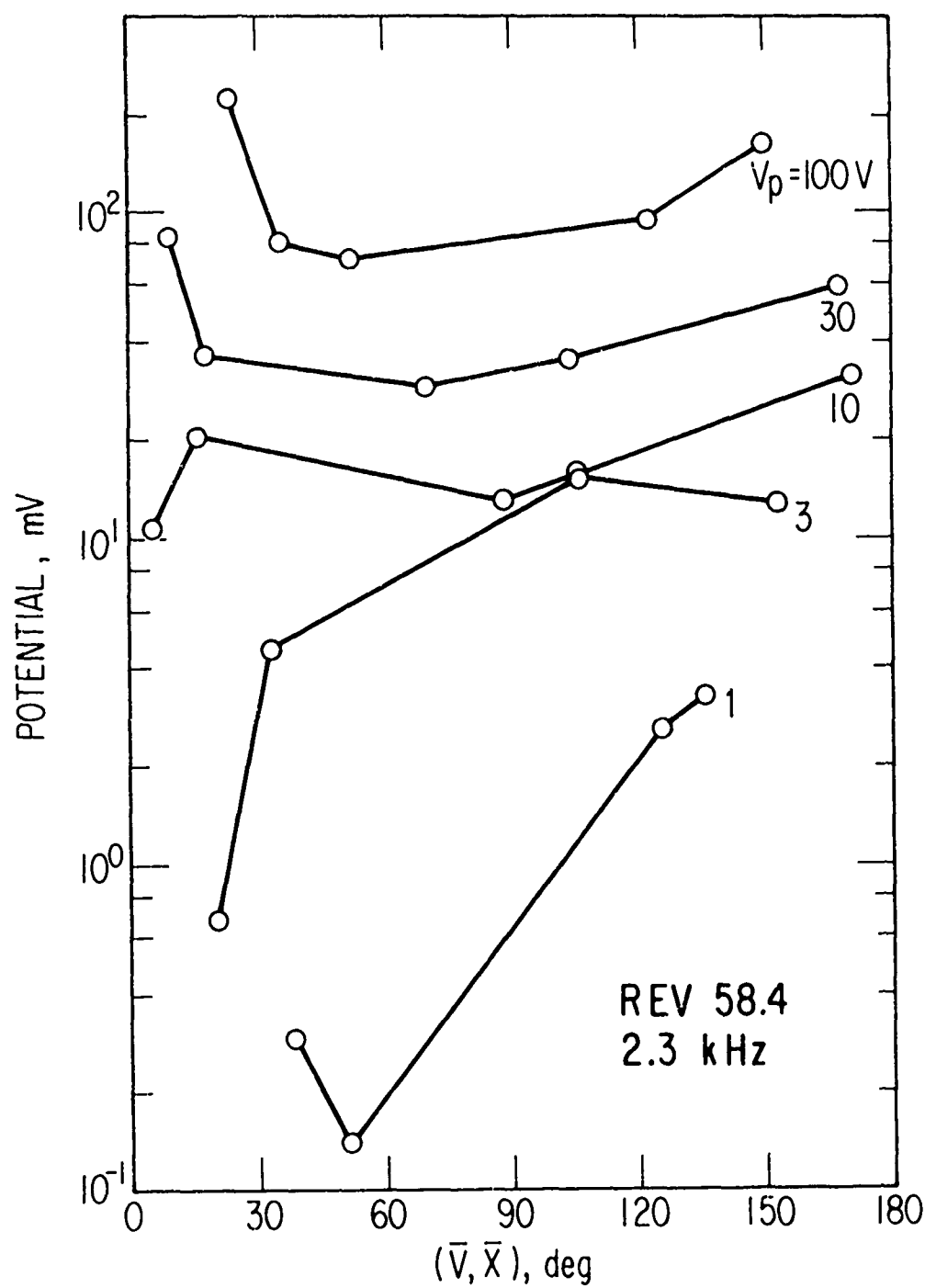Fig. 64. Potential vs ram angle for excitation at 1.3 kHz.

Fig. 65. Potential vs ram angle for excitation at 2.3 kHz.

comparable to the plasma flow velocity and the attenuation length is comparable to the distance from the exciter to the receiver, the signal from the downstream wave is significantly greater than that from the upstream wave. This effect has been observed in a laboratory ion acoustic wave experiment (Ref. 15).

D. DC ELECTRIC FIELDS

The DC potential between one of the STEM elements and the satellite body was measured during the 18-sec-quiescent period at the end of each data block. This potential together with the value of $\vec{v} \times \vec{B} \cdot l$ calculated from the aspect data and model geomagnetic field is plotted for an RTS acquisition in Fig. 66.

The range and phase of the measured DC potentials are in general agreement with the calculations. It should be pointed out that the length l was taken to be the full length (16 m) of one STEM antenna. The offset from zero and slight lack of symmetry is most likely due to the complicated surface properties of the satellite body. For example, the vehicle potential is several volts negative according to the ion trap data. There is no reason to expect the vehicle and the antenna to be at exactly the same potential.

E. CORRELATED MEASUREMENTS

The program for correlated measurements with other ground-based and satellite-borne ELF/VLF measurements was severely limited by the premature battery depletion on the OV1-21 satellite. All available data from the VLF receivers at Stanford, Dartmouth, and Kodiak and the receivers on the ISIS and Alouette satellites have been examined for emissions attributable to the NASC-117 experiment. There was no evidence of any detected radiation from the NASC-117 Impedance Experiment.

On simple theoretical grounds no measurable signal was expected to be radiated any significant distance at the very low current levels available to drive the short antenna. A nearby satellite should detect signals from a much longer antenna driven at higher current levels (Ref. 17).
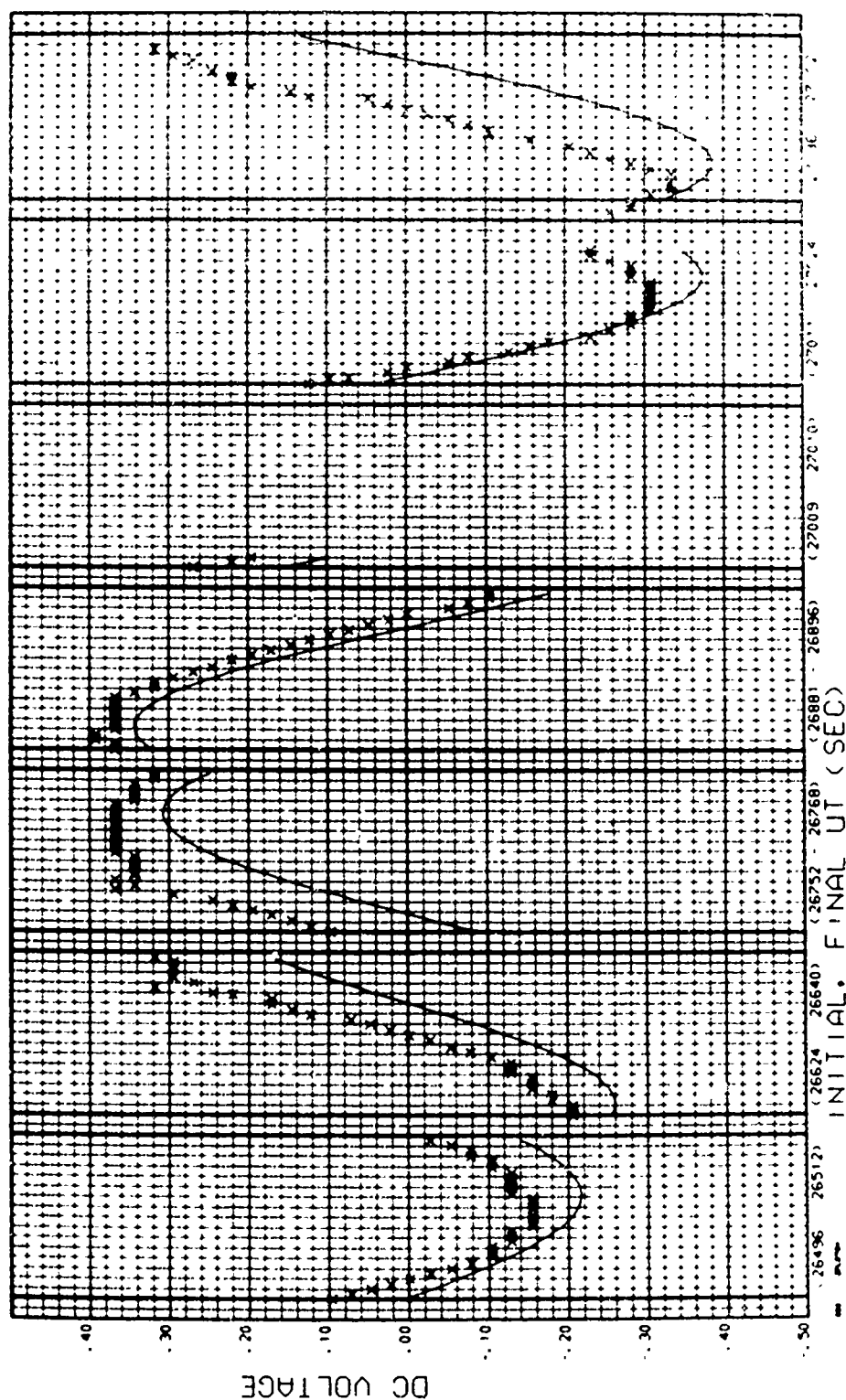
Fig. 66. Measured DC potential and computed values (○'s & □'s): $\bar{x}$ $\bar{E}$, $\bar{t}$ for an RTS acquisition between 07:21 and 07:2 F1 on 11 August 1971. (Satellite position – alt: 910–914 k; E/VL: 85.2–71.8°; B: 0.294–0.381 g, LL: 06-18-4:10 ..

VIII. SUMMARY

The data presented in this report represents only a small fraction of the total acquired during the one month lifetime of the NASC-117 experiment. The lack of funds and manpower preclude an in-depth analysis of the entire body of data collected.

The major effort was spent on obtaining the magnitude and phase of the primary dipole impedance since this was the primary objective of the experiment. The data presented in this report gives the range and trends of all of the parameters measured. It also catalogs and demonstrates the tools available for further in-depth analysis.

A.   CONCLUSIONS

The magnitude of the measured impedance and its increase with excitation voltage is in general accord with predictive models of Shkarofsky, Baker, and the model used by Develco.

The phase of the impedance becomes progressively inductive as the excitation voltage is increased. This is contrary to the available models which predict a capacitive phase shift with increasing voltage. We hypothesize that the inductive phase shift is due to the finite time it takes an ion to cross the sheath, and recommend that the predictive models be modified to include ion transit times.

Other unexpected results include: (1) a decrease in the harmonic content of the current waveform at the highest drive voltage relative to the next two lower drive voltages, (2) the asymmetric current waveforms, and (3) the possible generation of damped ion acoustic waves at the lower drive voltages.

Preceding page blank

REFERENCES

1. L. E. Orsak, et al., "VLF Propagation and Noise in the Ionosphere Observed by Sounding Rockets," Final Report Contract NASC-49(01), Stanford Research Institute, Menlo Park, Calif., January, 1965.

2. C. E. Young, "VLF Electric and Magnetic Antenna Impedance Characteristics in the Ionosphere," presented at the International Antenna and Propagation Symposium, URSI/IEEE Meeting, Palo Alto, Calif., 5-7 December 1966.

3. C. E. Young, "Impedance of LOFTI-IIA VLF Antennas in the Ionosphere," NRL Report 6712, Naval Research Laboratory, Washington, D.C., 18 June 1968.

4. S. D. Shawhan and D. A. Gurnett, "VLF Electric and Magnetic Fields Observed with the Javelin 8.45 Sounding Rocket," J. Geophys. Res., 73, 5649 (1968).

5. R. J. L. Grard and J. K. E. Tunaley, "The Impedance of the Electric Dipole Aerial on the FR-1 Satellite," Annal. des Geophys, 24, 49 (1968).

6. H. C. Koons, D. A. McPherson, and W. B. Harbridge, "Dependence of VLF Electric Field Antenna Impedance on Magnetospheric Plasma Density," J. Geophys. Res., 75, 2490 (1970).

7. D. P. Cauffman, D. A. Gurnett, and S. D. Shawhan, "Experimental Electric Antenna Characteristics in the Ionosphere at ELF/VLF," Proc. Conf. Antennas and Transionospheric Propagation as Related to ELF/VLF Downlink Satellite Communications, Naval Research Laboratory Report 7462, Washington, D.C., 27 November 1972.

8. D. A. Gurnett, et al., "Initial Observations of VLF Electric and Magnetic Fields with the Injun 5 Satellite," J. Geophys. Res., 74, 4631 (1969).

9. F. Palmer, "Rocket Probe Results Obtained with Crossed-Dipole Antennas," presented Conference on Antennas and Transionospheric Propagation as related to ELF/VLF Downlink Satellite Communications, Naval Research Laboratory, Washington, D.C., 8-10 June 1970.

10. I. P. Shkarofsky, "Nonlinear Sheath Admittance, Currents and Charges Associated with High Peak Voltage Drive on a VLF/ELF Dipole Antenna Moving in the Ionosphere," Radio Sci., 7, 503 (1972).

Preceding page blank

11.   F. L. Scarf, "Transmission Losses Associated with Plasma Perturbations," presented Conference on Antennas and Transionospheric Propagation as related to ELV/VLF Downlink Satellite Communications, Naval Research Laboratory, Washington, D. C., 8-10 June 1970.

12.   S. A. Self, "Exact Solution of the Collisionless Plasma Sheath Equation," *Phys. Fluids,* **6**, 1972 (1963).

13.   D. P. Cauffman and D. A. Gurnett, "Satellite Measurements of High Latitude Convection Electric Fields," *Space Sci. Rev.* **13**, 377 (1972).

14.   D. Baker, H. Weil, and L. S. Bearce, "Impedance and Large Signal Excitation of Satellite-Borne Antenna in the Ionosphere," *IEEE Transactions on Antennas and Propagation AP 12*, in press (September 1973).

15.   A. Y. Wong, R. W. Motley, and N. D'Angelo, "Landau Damping of Ion Acoustic Waves in Highly Ionized Plasmas," *Phys. Rev.*, **133**, A436 (1964).

16.   L. S. Bearce, "Some Considerations Related to the Feasibility of ELF/VLF Downlink Satellite Communications," Proc. Conf. Antennas and Transionospheric Propagation as Related to ELF/VLF Downlink Satellite Communications, Naval Research Laboratory Report 7462, Washington, D. C., 27 November 1972.

17.   L. H. Rorden, et al., The Feasibility of a Sub-LF Satellite-to-Submarine Communications Downlink (U), Develco Report No. 532-720731, Mountain View, California (31 July 1972)(S).

18.   J. Rubinstein and J. G. Laframboise, "Plasma Sheath Around a Floating Cylindrical Antenna at High Power," *Can. J. Phys.*, **48**, 1883 (1970).

19.   R. F. Mlodnosky and O. K. Garriott, "The V. L. F. Admittance of a Dipole in the Lower Ionosphere," Proc. Intern. Conf. Ionosphere, Institute of Physics and Physical Society, London (1963) pp. 484-491.

20.   U. Fahleson, "Theory of Electric Field Measurements Conducted in the Magnetosphere with Electric Probes," *Space Sci. Rev.*, **7**, 238 (1967).

21.   T. L. Aggson and C. A. Kapetanakos, On the Impedance of a Satellite Borne VLF Electric Field Antenna, NASA-Goddard Space Flight Center Report X-612-66-380, Greenbelt, Maryland (August 1966).